Impacts of Deforestation on Meteorology and Ecosystem Productivity in Appalachian Deciduous Forests

by

Carter E. Watson

(Under the direction of Ford Ballantyne IV)

Abstract

Deforestation has the potential to alter regional atmospheric dynamics, namely the motion of vapor, energy partitioning, and convective storm formation. Rates of photosynthesis are influenced by these factors, meaning nearby forest productivity can be influenced by the meteorological consequences of deforestation. This thesis uses process-based models to explore the implications of large, hypothetical deforestation events in Appalachia on the movement of water and primary productivity outside the deforested region. I found there was significant pixel-to-pixel and scenario-to-scenario variation in environmental conditions, forest productivity, and atmospheric feedbacks, despite environmental characteristics changing little on average. Additionally, the relative impact of changing environmental characteristics on changing primary production was dependent on the shape and extent of deforestation and background environmental conditions. These results suggest Appalachian forests are resilient to nearby deforestation, though there is heterogeneity in the environmental response, as deforestation influences environmental characteristics differently depending on its size, continuity, and orientation.

Index words: Theoretical ecology, Land-use change, Meteorology, Forest ecology, Plant physiology, Ecosystem modeling

Impacts of Deforestation on Meteorology and Ecosystem Productivity in Appalachian Deciduous Forests

by

Carter E. Watson

B.S., B.S., B.A., The University of Georgia, 2023

A Thesis Submitted to the Graduate Faculty
of The University of Georgia in Partial Fulfillment
of the
Requirements for the Degree

Master of Science

Athens, Georgia

2025

Impacts of Deforestation on Meteorology and Ecosystem Productivity in Appalachian Deciduous Forests

by

Carter E. Watson

Approved:

Major Professor: Ford Ballantyne IV

Committee: Anna Harper
Gabriel Kooperman
Alicia Peduzzi
J. Marshall Shepherd

Electronic Version Approved:

Ron Walcott
Vice Provost for Graduate Education and Dean of the Graduate School
The University of Georgia
May 2025

Dedication

For Liam, Lyssa, my parents, and the countless number of family and friends who make my life whole.

Acknowledgments

I am incredibly grateful to my advisor, Ford Ballantyne, for his phenomenal mentorship and support in my professional development. He encouraged me to dive in headfirst, to read lots of books and papers, run down every rabbit hole, and to let myself become engrossed in, and find joy in, the work we were doing. I am appreciative of all the help and guidance from the rest of my committee: Anna Harper, Gabriel Koopermann, Alicia Peduzzi, and Marshall Shepherd. With all of them outside the Odum School, their expertise was exceptionally beneficial in guiding this project. I owe Rico Holdo and his students, Maya Gonzales and Virginia Griswold, a debt of gratitude for the weekly Plant Reading Group, which was an excellent excuse to read papers and eat baked goods. I would like to thank John Knox for his help navigating the world of atmospheric models, as well as the wonderful folks on the NCAR message boards. Lastly, I am grateful for the lab server, Prospero, for doing the hard work, the Five Points Jittery Joe's for not charging me rent, and my 1949 Gibson A-40 for never going out of tune.

Table of Contents

Chapter 1

Introduction

Land cover change has the potential to alter mesoscale meteorological regimes, provided the magnitude of perturbation is sufficiently large (Mahmood et al. [2014]; Pielke Sr et al. [2011]). Anthropogenically altering the earth's surface inherently changes the land's surface roughness (Winckler et al. [2019]), energy partitioning (Yuan et al. [2021]), and albedo (Dirmeyer and Shukla [1994]), all of which exercise significant control over the movement of water vapor and the development of convective storms (Perugini et al. [2017]). Additionally, with specific regard to deforestation, the atmosphere loses a significant source of transpiration, and the surface loses an important temperature regulation mechanism. These disruptions can cascade into regional climate shifts, altering the movement of vapor, precipitation patterns (Bagley et al. [2014]), boundary layer convection (Fisch et al. [2004]), and even large-scale atmospheric circulation (Avissar and Werth [2005]).

The ability of deforestation to influence atmospheric processes has been extensively modeled, particularly in tropical latitudes (Fisch et al. [2004]; Winckler et al. [2019]; Bagley et al. [2014]; Medvigy et al. [2011]), where a large quotient of rainfall derives from evapotranspiration (Schlesinger and Jasechko [2014]). These computational studies investigate how changing land surface properties, like albedo, roughness, and energy partitioning influence convective precipitation. From these studies, it has become generally accepted that tropical deforestation leads to declines in precipitation (Medvigy et al. [2011]). Recently, this prediction has been substantiated by decades of weather station, reanalysis, and satellite data in Amazonia, the Congo, and southeast Asia (Smith et al. [2023]). This association between

deforestation and precipitation in the tropics begs the question of whether deforestation has the same consequence across other biomes and ecoregions.

While there have been many studies assessing how land cover change can induce alterations in hydrologic cycles in tropical environments, less attention has been given to temperate, midlatitude regions. This is likely because proportionately less rainfall is derived from local moisture cycling, meaning changing the land surface has a relatively smaller impact on local rainfall comparatively (Boutle et al. [2011]). However, studies focusing on these interactions in the midlatitudes (Gates and Liess [2001]; Rodgers et al. [2018]; Weaver and Avissar [2001], for instance) demonstrate that land surface does exert control over the intensity and frequency of convective storms. In fact, Weaver and Avissar [2001] notes that synoptic-scale winds play an important role in guiding the direction of the landscape-induced circulations, as opposed to inhibiting them. Additionally, even if these changes are slight compared to tropical environments, convective rainfall in the midlatitudes is not negligible and still exerts control over ecological processes. For instance, deciduous forest primary production is dependent on the physiology and stomatal aperture of dominant plant species, both of which are heavily influenced by the atmospheric and edaphic conditions dependent on hydrology of the region. For example, vapor pressure deficit (VPD) exerts significant control over photosynthesis and stomatal regulation in mesic environments (Grossiord et al. [2020]), as do soil moisture (A Al-Ani and Bierhuizen [1971]) and light availability (Shimazaki et al. [2007]). While the understanding of how plants respond to stress is still developing (see review by Anderegg [2023]), it is generally accepted that VPD, soil moisture, and light availability all exert some degree of influence over the rate of carboxylation (Li et al. [2018]; Wei et al. [2008]; Bunce [2016]), stomatal aperture, and conductance.

Additionally, carbon assimilation via photosynthesis and stomatal conductance correspond with energy partitioning at the surface, with vegetation increasing latent heat flux (Williams and Torn [2015]). Land cover changes that enhance or reduce photosynthesis therefore impact surface energy partitioning, with significant implications on the local water

cycle. For instance, enhanced stomatal conductance and photosynthesis typically increase rates of transpiration, increasing the quotient of vapor in the atmosphere, which increases convective precipitation events, replenishing soil moisture. However, decreased stomatal activity may act to reduce the vegetation-controlled flux of precipitation to the atmosphere, which could limit convective precipitation events. Because moisture changes within an area of land cover are transported beyond it by atmospheric motion, the potential effects of land cover change could ripple far outward and alter non-local gross primary production (hereafter GPP) and latent heating significantly over the course of a growing season.

Understanding how land use change influences atmospheric and ecological processes is of prime importance to understanding the scope of how anthropogenic activity influences the environment (Pielke Sr et al. [2011]). Therefore, it is important not to neglect temperate, midlatitude regions when investigating the influence of deforestation on mesoscale weather patterns. In the early-20th century, over 80% of central/southern Appalachia was clearcut for timber and mineral extraction (Yarnell [1998]). Significant forest cover has since returned as regional economic activity has decreased (Gragson and Bolstad [2006]) and an interest in using the land for carbon capture and storage has increased (Shade et al. [2025]). This, however, may change as efforts to revitalize the region's economy continue and climate change continues to intensify (Butler et al. [2015]). With the understanding that Appalachia may experience significant deforestation and land use change over the next several decades, and the understanding that deforestation substantially decreases rainfall in tropical environments, it is worth exploring how deforestation influences both meteorology and remaining deciduous forest ecophysiology in the temperate midlatitudes.

This project aims to investigate how deforestation in the temperate deciduous forests of Appalachia impacts meteorological conditions, and how changes in meteorology influence primary production in the remaining forested areas. Specifically, using a coupled atmosphere-land surface modeling appraoch, I aimed to (1) characterize the influence of significant deforestation on environmental conditions (wind speed & direction, cloud cover, VPD, daily

rainfall, and soil moisture) both *inside* and *outside* the deforested region, placing emphasis on how prevailing wind direction and distance from the deforestation center influence the spatial patterns and magnitude of these changes; (2) determine how changes in these environmental conditions influenced changes in GPP in the remaining deciduous forest; and (3) determine if changes in GPP correlated with changes in latent heat (LH) due to water loss during carbon fixation, marking a potential positive feedback in the exchange of water between the land surface and the atmosphere. These questions were addressed for multiple large-scale deforestation scenarios across a gradient of size, continuity, and spatial orientation and between comparatively "dry" years versus "wet" years, to determine whether the relative importance of different meteorological components in determining changes in GPP shift based on the climate context.

Chapter 2

Methodology

2.1 Coupled Model System, Parameterization, & and Domains

The Noah Multiparameterization Land Surface Model (Noah-MP) (version 4.5) allowes for the dynamic simulation fo carbon biogeochemistry and vegetation physiology (Niu et al. [2011], He et al. [2023]). I coupled this with the Advanced Research Weather Research and Forecasting (WRF-ARW) model (version 4.6.0), which is a mesoscale numeric weather prediction model designed for climatological research and operational forecasting (Skamarock et al. [2019]). Previous studies have demonstrated the effectiveness of utilizing this coupled model scheme in other contexts (see Yu et al. [2022]), and of using WRF for ecological purposes (He et al. [2015]). To simulate lateral boundary conditions, WRF make use of High-Resolution WRF V4 Geographical Statistic Data and ECMWF Reanalysis V5 (ERA5) single and pressure level data (Hersbach et al. [2020]). WRF is driven by a series of microphysics, cumulus, radiation, planetary boundary layer, surface, and land-surface physics schemes, as seen in Table. 2.1. These were chosen by examining successful WRF studies along the eastern United States. Noah-MP contains a similar set of parameterization schemes, though all were kept standard except the Canopy Radiation Transfer scheme (Modified Two-Stream, Niu and Yang [2004]) and the Dynamic Vegetation scheme (fully dynamic).

WRF Physics Parameters

Component	Parameterization Scheme	Studies Utilized
Cloud Microphysics	WSM6 (Hong and Lim [2006])	Rodgers et al. [2018]; Mallard and Spero [2019]; Gao et al. [2012]
Cumulous Physics	Kain-Fritsch* (Kain [2004])	Rodgers et al. [2018]; Mallard and Spero [2019]; Gao et al. [2012]
LW Radiation	RRTMG (Iacono et al. [2008])	Mallard and Spero [2019]; Gao et al. [2012]
SW Radiation	RRTMG (Iacono et al. [2008])	Mallard and Spero [2019]; Gao et al. [2012]
BL Physics	Yonsei University (Hong et al. [2006])	Rodgers et al. [2018]; Mallard and Spero [2019]
Surface Physics	Revised MM5 M-O (Jiménez et al. [2012])	Mallard and Spero [2019]
Land-Surface Model	Noah-MP	

Table 2.1: WRF Parameters used in both synoptic and focal domain simulations. *Kain-Fritsch was used only by the parent domain. No parameterization was used in the focal domain.

2.1.1 Simulation Domains

I simulated a large 15×15 km resolution parent domain to resolve large-scale synoptic systems and a smaller focal domain of 3×3 km resolution over my primary region of interest, as seen in Fig. 2.1. Adhering to the recommendations resulting from other successful attempts to model atmospheric processes across the eastern United States with WRF (see Rodgers et al. [2018], for instance), the synoptic domain extends far west and east, capturing parts of the Midwest, the Gulf Coast, and the Atlantic Seaboard, while also capturing synoptic air movement from the Atlantic Ocean and the Northeast. The 1500×1500 km is a total area large enough to capture large-scale pressure systems, fronts, and jet streams.

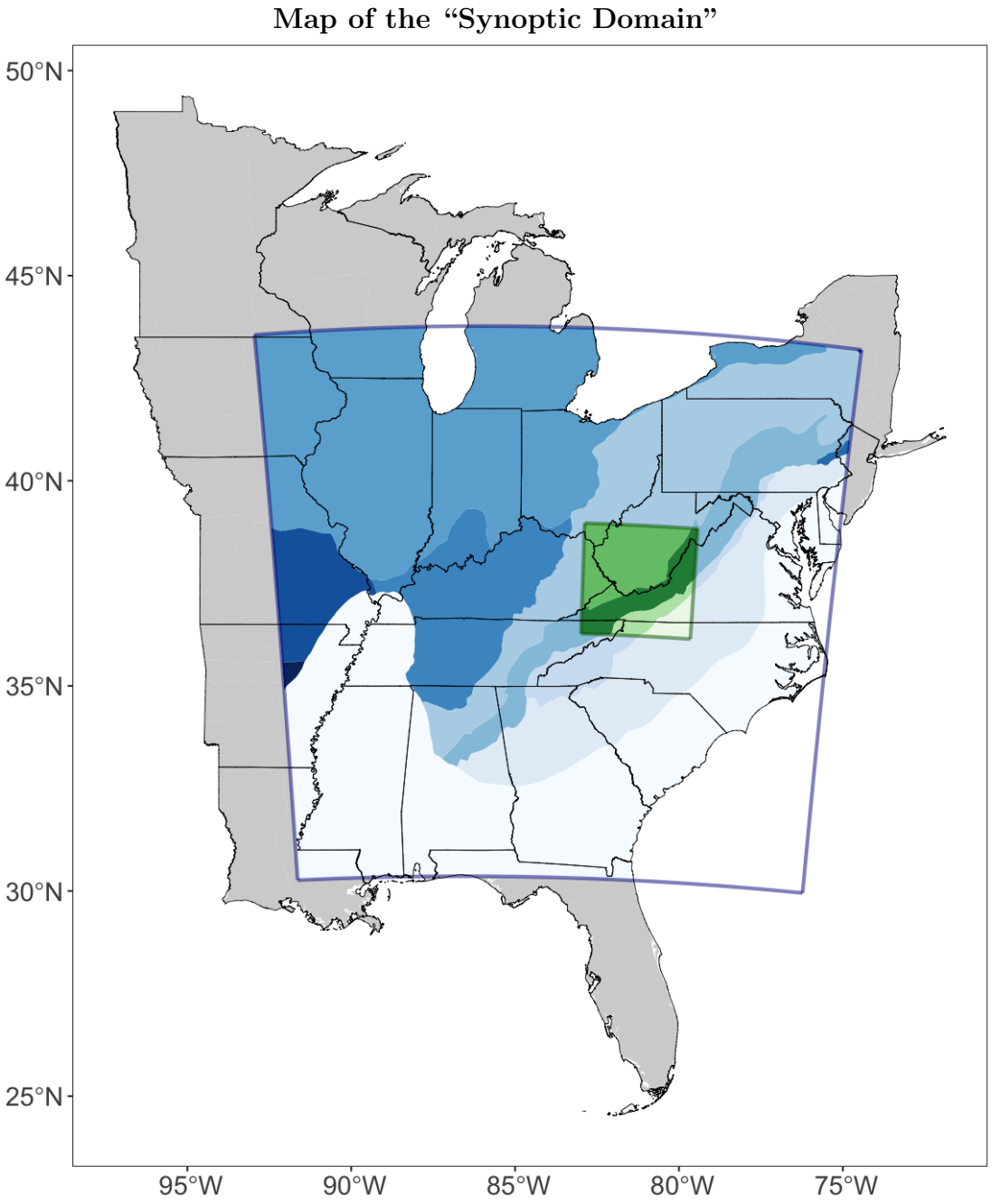

Figure 2.1: Synoptic & Focal Domains relative to the eastern United States. Shading represents different physiographic regions throughout the continental United States. From bottom right to top left, the focal domain consists of the Piedmont, Blue Ridge Mountains, Valley & Ridge, and the Appalachian Plateau.

The focal domain, which rests inside the synoptic domain, extends 303×303 km across portions of Virginia, West Virginia, Ohio, Kentucky, Tennessee, and North Carolina (Fig. 2.2). The 3×3 resolution is a computationally efficient size that is small enough to explicitly simulate shallow convection, turbulent mixing, and regional carbon dynamics with detail. This resolution yields a ratio of synoptic to focal domain resolution that is 1:5, allowing dynamical downsampling to occur without significant error.

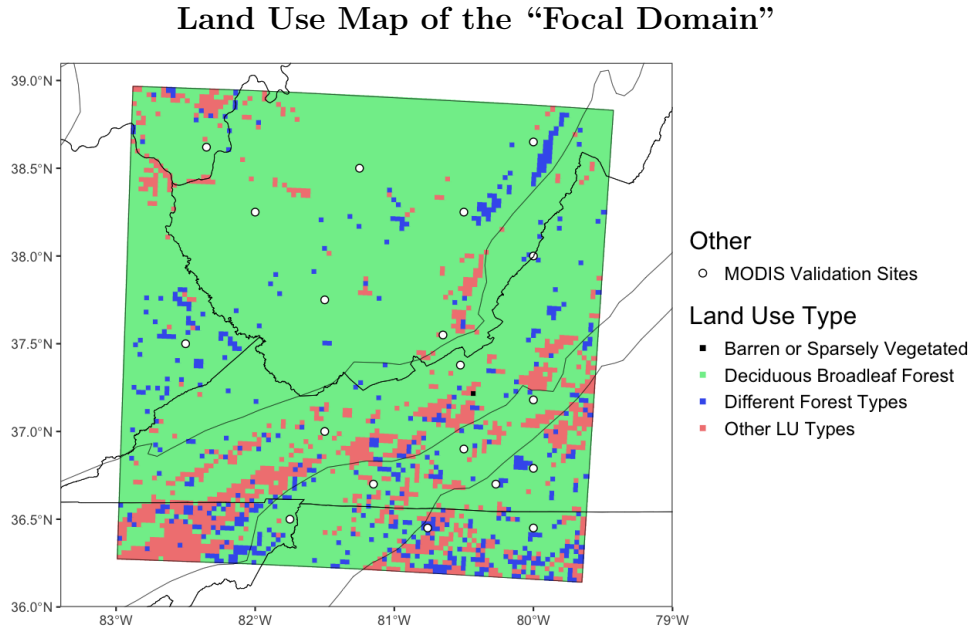

Figure 2.2: Map of the "focal domain" with land use type and lines denoting physiographic regions (Bureau [2020]). Focal domain is 303×303 km in area, with a 3 km resolution. 84.26% of the land is classified as "Deciduous Broadleaf Forest", 5.26% are of different forest functional types, 0.01% are marked as "Barren or Sparsely Vegetated", and 10.45% are classified as different land uses all together. This said, the model recognizes uneven/unequal distribution of vegetation in each pixel, having varying vegetation fractions for each location. White dots denote MODIS validation points.

2.1.2 Focal Domain Physiography

Appalachia is inhomogeneous and contains a variety of physiographic regions with varying topography and geomorphic structure, resulting in a diversity of climatic and weather conditions along elevation, terrain, and hydrological gradients. The focal domain intends to capture this diversity, as it includes many physiographic regions, including the Piedmont foothills, the Blue Ridge Mountains, the Valley and Ridge, and the dominant Appalachian Plateaus, as seen in Fig. 2.3.

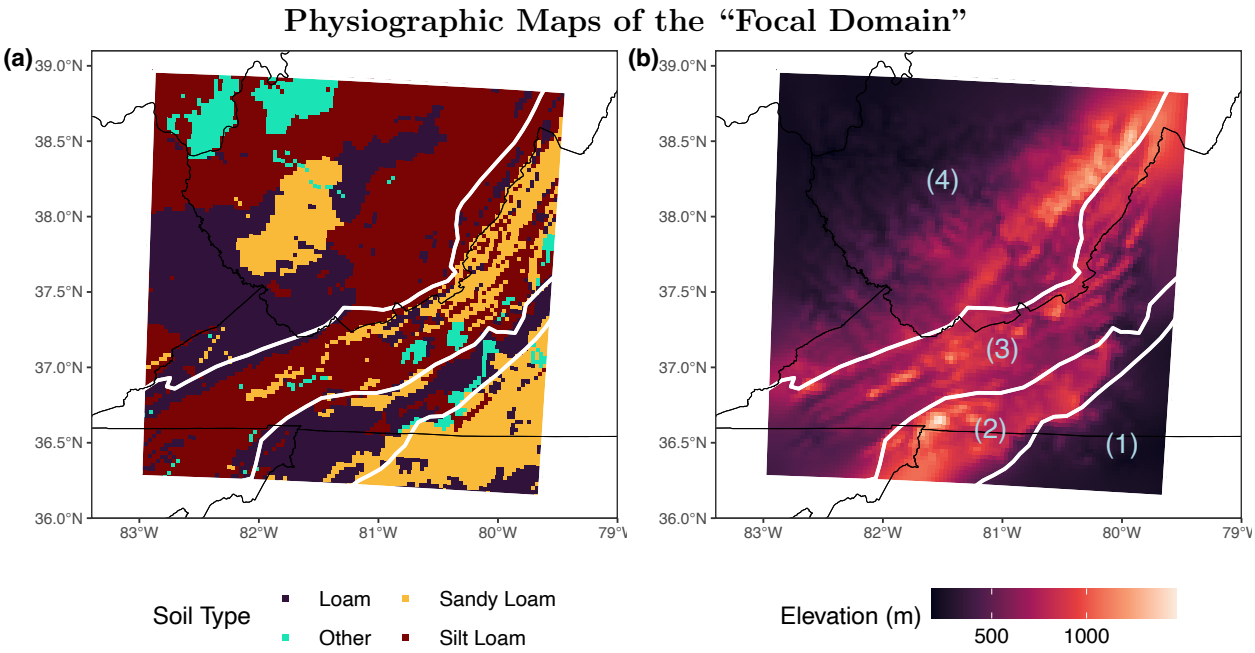

Figure 2.3: Figures aimed at characterizing phisiographic diversity across the focal domain. (a) Soil types across the focal domain: 30.50% "Loam", 45.52% "Silt Loam", 18.74% "Sandy Loam". (b) Elevation across focal domain. Highest: 1474 m. Lowest: 183 m. White lines denote physiographic region boundaries: (1) Piedmont, (2) Blue Ridge Mountains, (3) Valley and Ridge, & (4) Appalachian Plateau.

2.2 Primary Productivity Characterization, Optimization, & Model Validation

In Noah-MP, the rate of photosynthesis and GPP for C3 vegetation (the only type in Appalachian forests of the region) is a function of light, internal partial pressure of CO_2, temperature, soil moisture, foliar nitrogen, and surface air pressure, with the minimum of light- (Equation (2.1)), rubisco- (Equation (2.2)), or export-limited (Equation (2.3)) rates prescribing the realized rate (Equation (2.4), Fig. 2.4) (Niu and Yang [2004] & Dickinson et al. [1998], based upon Farquhar et al. [1980]).

$$W_J = \frac{\max(P_{CO_2,init} - P_{c,CO_2}, 0) \times J_e}{P_{CO_2,init} + 2 \times P_{c,CO_2}} \tag{2.1}$$

$$W_c = \frac{\max(P_{CO_2,init} - P_{c,CO_2}, 0) \times V_{C,max}}{P_{CO_2,init} + F_{wc}} \tag{2.2}$$

$$W_e = 0.5 \times V_{\mathrm{C,max}} \tag{2.3}$$

$$P_{SN} = \min(W_J, W_c, W_e) \times I_{GS} \tag{2.4}$$

Light-limited photosynthesis depends the rate of electron transport (J_e), which is the product of photon flux, and quantum efficiency, multiplied a temperature-dependent, saturating function of internal partial pressure of CO_2 ($(\max(P_{CO_2,init} - P_{c,CO_2}), 0)/(P_{CO_2,init} + 2 \times P_{c,CO_2})$). Rubisco-limited photosynthesis is a product of maximum rate of carboxylation ($V_{C,max}$), which is a product of foliar nitrogen, soil moisture, and a unimodal function of temperature, and a temperature-dependent, saturating function of internal partial pressure of CO_2 (similar to that for light-limited photosynthesis, $(\max(P_{CO_2,init} - P_{c,CO_2}, 0)/(P_{CO_2,init} + F_{wc})$. The saturating functions for light- and rubisco-limited photosynthesis are influenced by half saturation constants for CO_2 and O_2, and the partial pressure of O_2, to incorporate the effect of photorespiration on rate of carbon fixation, and only differ in their values of

half-saturation constants. Export-limited photosynthesis is simply half the maximum rate of carboxylation for rubisco-limited photosynthesis. The realized rate of photosynthesis is a minimization function of all three limited pathways, multiplied by a binary indicator of growing season I_{GS}. Stomatal conductance is subsequently computed from the realized rate of photosynthesis according to the empirical Ball-Berry relationship (Ball et al. [1987]).

2.2.1 Validating GPP

Prior to simulating the effects of deforestation, I performed a preliminary one-way, simulation from January 1, 2017 to November 1, 2018 using WRF's nesting input preprocessor (ndown) to determine if the coupled atmosphere and dynamic vegetation model system could accurately simulate GPP for the focal domain. I randomly chose 19 locations (Fig. 2.2) from the simulation matching the "temperate deciduous forest" land cover type and compared their 8-day GPP averages to corresponding 8-day MODIS Terra GPP data, at a similar resolution, for the entire growing season (Running and Zhao [2021]). This initial simulation overestimated of GPP across the "temperate deciduous forest" pixels across the focal domain by $> 30\%$, as seen in Fig. 2.5a. This overestimation is consistent with a recent study (Li et al. [2022]), which found Noah-MP overestimates primary production (GPP) in the continental United States by >40% when dynamic vegetation is turned ON.

To address the overestimation of GPP, I worked to identify what parameter values within Noah-MP might be leading to an overestimation within the "temperate deciduous forest" land use type. Li et al. [2022] recommended reviewing the parameterization values within Noah-MP of VCMX25, the maximum rate of carboxylation at 25°C, and AVCMX, the Q10 for VCMX25. Turnbull et al. [2002] found the VCMX25 for three keystone eastern United States tree species *Q. rubra*, *Q. prinus*, and *A. rubrum* to range between 32.4 and 57.3 μmol CO_2 m^{-2} s^{-1} and the carbon assimilation rate at 25°C to be between 6.76 and 13.5 μmol CO_2 m^{-2} s^{-1}, depending on the position in the canopy. Noah-MP's initial parameterization held VCMX25 to be at a constant 60 μmol CO_2 m^{-2} s^{-1} which results in a

rubisco-limited carbon assimilation rate of 18.8 μmol CO_2 m^{-2} s^{-1} at 25°C (Fig. 2.4a). I adjusted VCMX25 to 43 μmol CO_2 m^{-2} s^{-1} and increased AVCMX from 2.4 to 3.4 in an effort to better reflect seasonality. Altering these values in the model decreased the rubisco-limited rate of carbon uptake at 25°C to 13.5 μmol CO_2 m^{-2} s^{-1}, which falls appropriately in the range articulated by Turnbull et al. [2002] (see Fig. 2.4b).

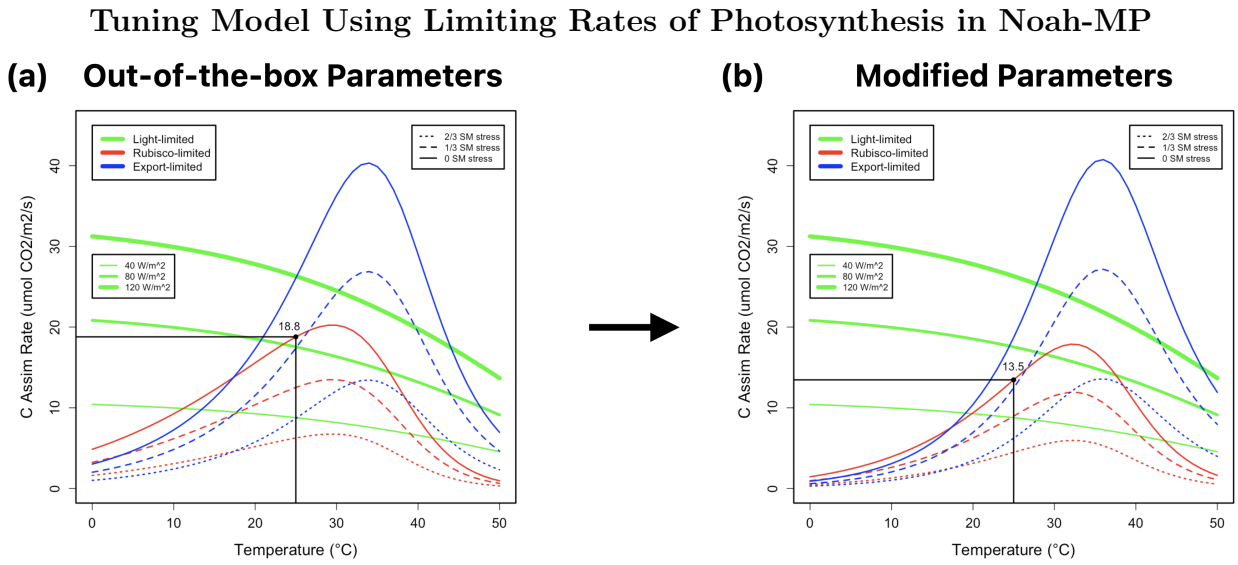

Figure 2.4: Graphical depiction of limiting photosynthetic rates across a temperature gradient. At 25°C, without limiting light or soil moisture, the out-of-the-box parameterization (a) found the rate of carbon assimilation to be 18.8 μmol CO_2 m^{-2} s^{-1}. Following adjustments to VCMX25 and AVCMX, (b) the maximum rate of carbon assimilation at 25°C without limiting light or soil moisture decreased from 18.8 $\rightarrow$ 13.5 μmol CO_2 m^{-2} s^{-1} at 25°C, which falls in the range of observed values (Turnbull et al. [2002]).

Following my adjustments to the "temperate deciduous forest" VCMX25 and AVCMX parameters, I again ran a simulation from January 1, 2017 to November 1, 2018 and compared the modeled GPP data with MODIS data at the same 19 random points (Fig. 2.5b). The adjusted carboxylation parameterization fits the MODIS data much better than the 'off the shelf' parameterization (Fig. 2.5a), and sufficiently well that this parameterization was used for the deforestation simulations.

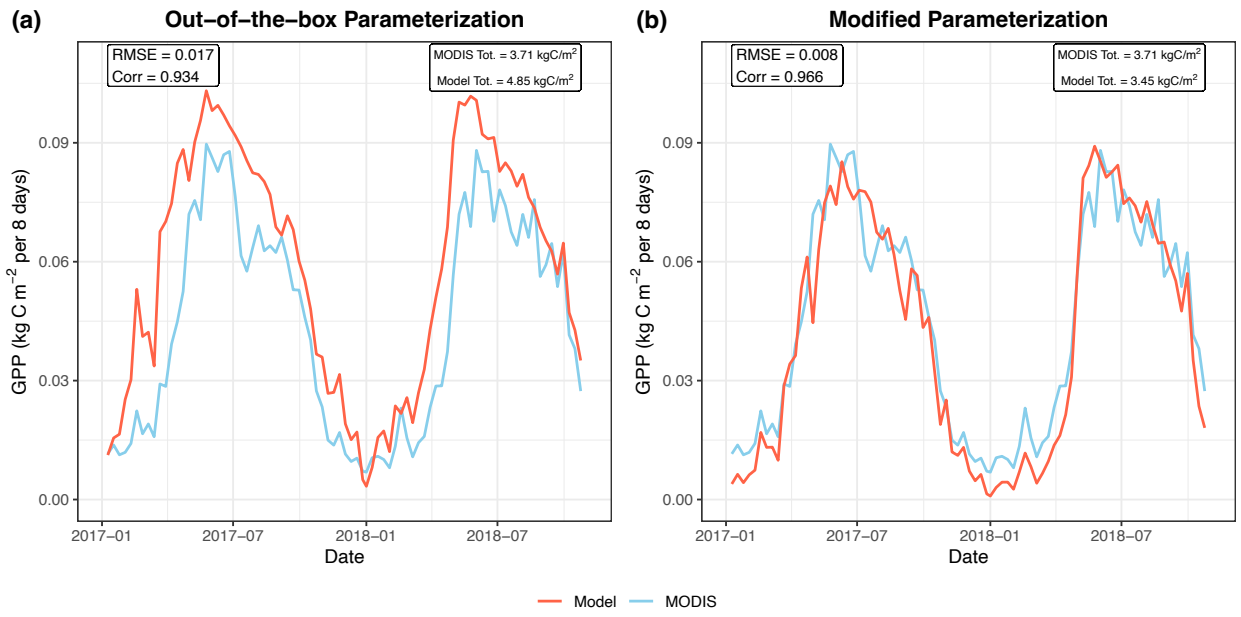

Figure 2.5: Comparison of MODIS GPP and Modeled GPP between January 1st, 2017 and November 1st, 2018 averaged across 19 random locations throughout the focal domain. For a specific map of locations used for validation, see Fig. 2.2. (a) Using Noah-MP's out-of-the-box parameterization of VCMAX25 = 60 μmol CO_2 m^{-2} s^{-1} and AVCMX = 2.4, the model simulated 4.85 kg$C$ m^{-2} total, a >30% overestimation. (b) Using the modified parameterization of VCMAX25 = 43 μmol CO_2 m^{-2} s^{-1} and AVCMX = 3.4,, the model simulated 3.45 kg$C$ m^{-2} total, a <7% underestimation. Under the modified parameterization, the correlation increased and R^2 decreased.

2.2.2 Validating Precipitation

Additionally, across this simulation, I compared the total rainfall simulated during the two growing seasons (April-October 2017 and 2018) using PRISM climate data (Group [2019]). WRF underestimated precipitation by 15.0 % in 2017 (844 mm PRISM, 718 mm WRF) and 27.2% in 2018 (1023 mm PRISM, 745 mm WRF). There were marginal overestimations in regions with high elevation (see Fig. 2.3). Additionally, there was a border around the edge of the WRF domain where precipitation did not simulate reasonably. To address this issue,

I excised a 4-pixel border from WRF and again validated against PRISM. Removing this border aligned the simulated precipitation much more closely with the reanalysis data, as seen in Fig. 2.6, and signaled a need to remove a 4-pixel border for all further data processing. This precipitation validation data is consistent with other successful WRF simulations (see analysis of precipitation bias over central Europe: Stergiou et al. [2021]).

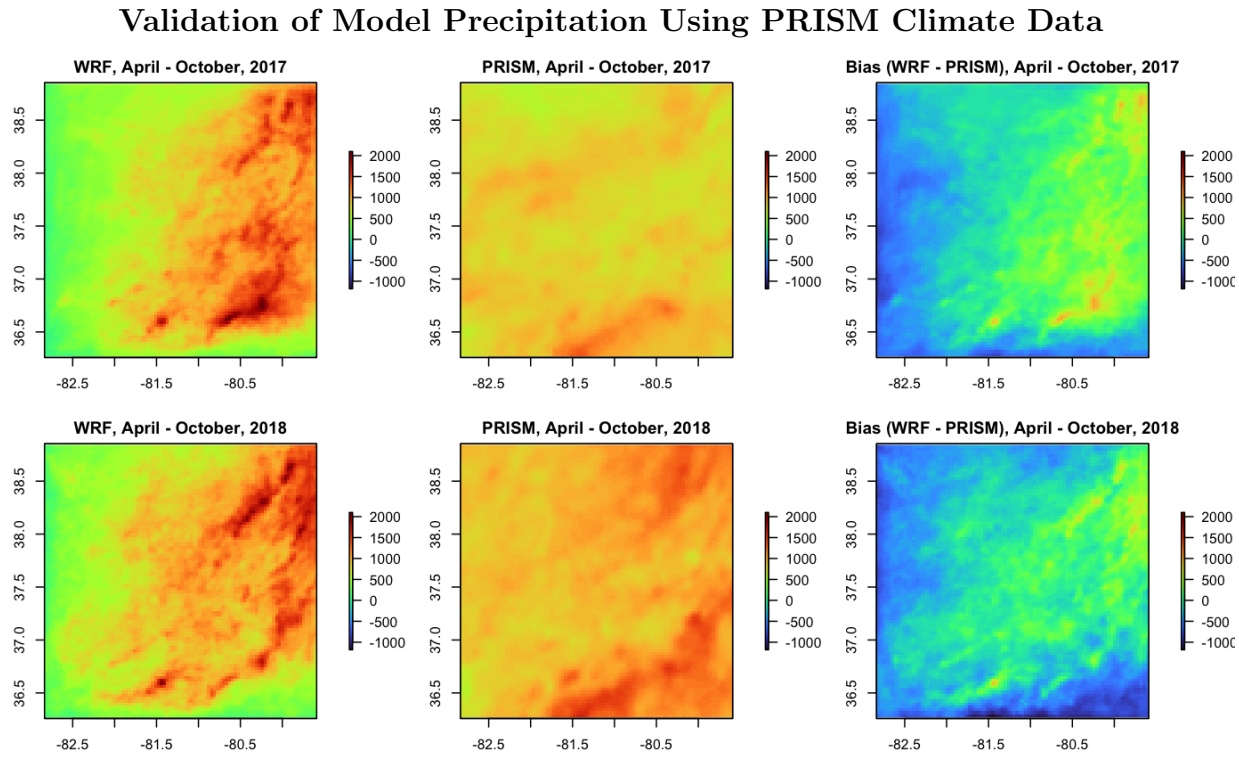

Figure 2.6: A comparison of PRISM Reanalysis precipitation and Modeled precipitation between April 1st and November 1st in 2017 and 2018 in millimeters. Removing the spurrious 4-pixel border decreased the underestimations to 4.9% in 2017 (846 mm PRISM, 804 mm WRF) and to 17.0% in 2018 (1018 mm PRISM, 840 mm WRF).

According to PRISM, an average of 846 mm of rain fell between April 1, 2017 and November 1, 2017 across the focal domain, while 1018 mm of rain fell between April 1, 2018 and November 1, 2018, meaning 2018 received 20.3% more rainfall than 2017. Therefore, running the deforestation simulations across the growing season for both 2017 and 2018 allows

for the determination of the impact of total rainfall on the magnitude of changes in environmental variables, primary production, and latent heating by comparing a comparatively "dry" year to a comparatively "wet" year.

2.3 Experimental Setup

Once I successfully validated the model system, I was in a position to simulate deforestation scenarios, which occurred during the growing season in 2017 and 2018. First, the synoptic domain was simulated twice, once from March 1, 2017 to November 1, 2017, and again from March 1, 2018 to November 1, 2018. Using the wrfout* data from the synoptic domain simulations as input for WRF's ndown.exe tool, I performed a total of 14 one-way runs of the focal domain. One-way runs minimize the probability of spurious variation in the synoptic domain that could lead to unrealistic focal domain phenomena, while increasing computational efficiency. To additionally increase model stability, vertical damping was turned on, decreasing the vertical motion of air above a height of 12,000 m, a height that will not limit convection nor hinder landscape processes.

I simulated the focal domain 7 times for 2017 and 7 times for 2018, each time with an altered land cover scheme. For both 2017 and 2018, I first simulated the domain unchanged (see Fig. 2.2) to establish control conditions. I then simulated six different land cover treatments, as seen in Fig. 2.7, using NCAR Command Line to manipulate wrfinput files, changing the LU_INDEX (land cover type/plant functional type) across all forest pixels to 16 ("barren or sparsely vegetated") and the VEGFRA (fraction of vegetation cover per-pixel) to 0 in a variety of patterns. Doing so reduces the surface roughness coefficient from 0.15 to 0 and alters albedo (increases or decreases depending on time of day) across each deforested pixel. Specific details about each land cover treatment are included in Table 2.2. All land cover alterations stretch a length of 254.558 km, and are designed to determine if the size, spatial orientation, and continuity of the deforested patch influence how environmental and ecological components of the landscape respond to the perturbation. To allow for an

appropriate spin-up period, I excised the first 11 days from the data, meaning "growing season" shall hereafter refer to March 12 to November 1.

Land Cover Scenario Details

LC Scenario	Area (km^2)	Thickness (km)	Orientation	Patches
001	17,667	42.426	BL→TR	N/A
002	8,343	21.213	BL→TR	N/A
003	4,599	42.426	BL→TR	9 km^2 with 3 km-thick boundary
004	10,377	42.426	BL→TR	81 km^2 with 3 km-thick boundary
005	17,469	42.426	TL→BR	N/A
006	8,109	21.213	TL→BR	N/A

Table 2.2: Characteristics about each deforestation scenario: how they vary in size, spatial orientation, and continuity. LC Scenarios oriented from BL-TR follow the orientation of the prevailing NE winds, while TL-BR scenarios are oriented perpendicular to the prevailing winds.

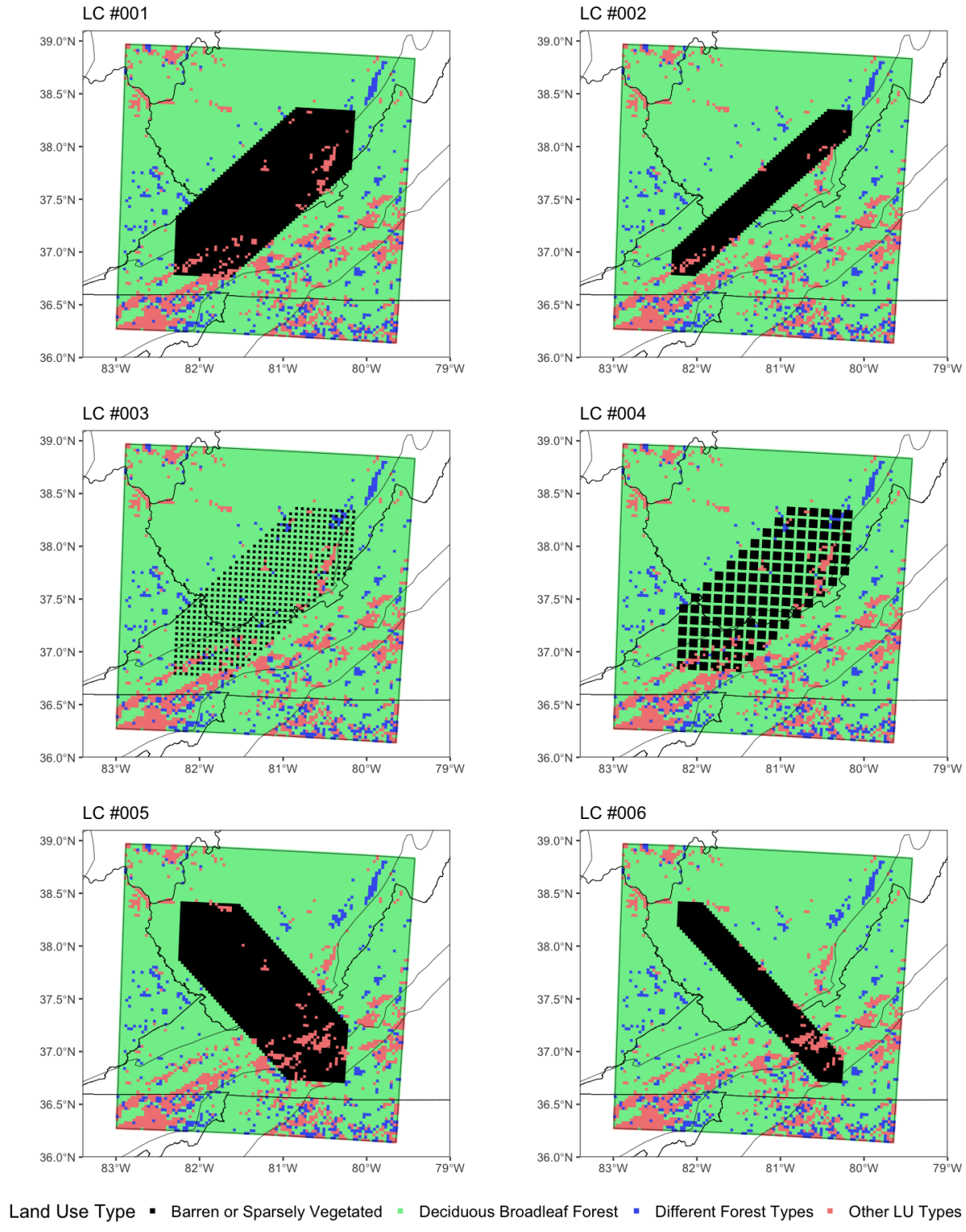

Figure 2.7: Maps of the six land cover/deforestation scenarios. Color denotes per-pixel land use type. See Table 2.2 for specific information regarding size and orientation.

2.4 Statistical Methodology

Because I only parameterized the "temperate deciduous forest" land cover type within Noah-MP, I only considered the environmental, edaphic, and carbon dynamics of these pixels. Pixels that (1) had a mean relative humidity over 100%, (2) had a mean vegetation temperature $\leq$0°C, and (3) saw a mean change in vegetation temperature $\geq$—1.7—°C were considered outliers and were excised from the data. To characterize the environmental conditions both within the deforested and remaining forest pixels, I chose to focus on **VPD** (amount of moisture the atmosphere can hold at saturation minus the amount of moisture is actually in the atmosphere), **soil moisture** from the top 10 cm (an important component of the water potential gradient), **available shortwave radiation** reaching the surface (a reasonable proxy for both cloud cover/convection (see Dirmeyer and Shukla [1994]) and photosynthetically active radiation), and **daily precipitation**. I additionally chose to investigate 10-m $u - v$ wind speed and direction inside the deforested pixels, as I believed this could play a role in altering the flow of water vapor and influence changes in VPD. I then investigated how changes in these environmental conditions elicited changes in GPP across different LC Scenarios and "wet" and "dry" years.

With the understanding that photosynthesis and GPP are intimately linked to stomatal conductance (see Section 2.2), I investigated how changes in GPP correlated with changes in Latent Heat (LH) across different LC Scenarios and "wet" and "dry" years. All the aforementioned variables were outputs of the WRF-Noah-MP coupled model system, with the exception of VPD. Because VPD is more ecologically relevant, as it captures how plants respond to water potential gradients between the soil and the atmosphere (see Grossiord et al. [2020]), I derived it from other output variables using Equation (2.5) (well-established, see Petty [2008]), where T2 is 2-meter temperature, Q2 is mixing ratio, P_{sfc} is surface-level pressure, i is longitude, j is latitude, t is timestep (hours), and T is trial (C for control).

$$\mathrm{VPD}_{i,j,t,T} = 611.2 \times \exp\left(\frac{17.67 \times (\mathrm{T2}_{i,j,t,T} - 273.15)}{(\mathrm{T2}_{i,j,t,T} - 273.15) + 243.5}\right) - \frac{\mathrm{Q2}_{i,j,t,T} \times P_{sfc_{i,j,t,T}}}{0.622 \times \mathrm{Q2}_{i,j,t,T}}, \tag{2.5}$$

Following the completion of the simulations, I first calculated the per-pixel average of each variable across each growing season for each LC Scenario, $\overline{x_{i,j,T}}$, where x is some environmental variable. After calculating $\overline{x_{i,j,T}}$, I subtracted the per-pixel average of the control ($\overline{x_{i,j,C}}$), giving the average difference in x between *before* and *after* the deforestation across the remaining deciduous forest pixels (Equation (2.6)).

$$\Delta\overline{x_{i,j,T}} = \overline{x_{i,j,T}} - \overline{x_{i,j,C}} \tag{2.6}$$

To determine how $\Delta\overline{x_{i,j,T}}$ was changing in space with respect to the center of the focal domain, I utilized the R package *geosphere* (Hijmans et al. [2017]) to assign polar coordinates to each pixel relative to the center of the focal domain, (-81.21869, 37.57799), and to the east direction (CCW: $\theta > 0$, CW: $\theta < 0$). I then characterized how $\Delta\overline{x_{i,j,T}}$ changes with regard to θ to determine the influence of radial direction. This allowed for the determination of the relative impact of the deforested region's spatial orientation, relative to the average wind direction within the deforested pixels. Additionally, I calculated the absolute value for all $\Delta\overline{x_{i,j,T}}$, abs($\Delta\overline{x_{i,j,T}}$), and plotted it as a function of distance from the center of the focal domain.

To analyze the influence of deforestation on these environmental and edaphic components, I used z-score normalization and standardized regression to demonstrate the relative impact of each $\Delta\overline{x_{i,j,T}}$ on $\Delta\overline{\mathrm{GPP}_{i,j,T}}$. Standardized regression allows for the direct comparison between the strength of the relationship between $\Delta\overline{\mathrm{GPP}_{i,j,T}}$ and different $\Delta\overline{x_{i,j,T}}$. Thus, I could compare the relative impact of a one standard deviation change in one $\Delta\overline{x_{i,j,T}}$, to a one standard deviation change in another $\Delta\overline{x_{i,j,T}}$. This allows for the determination of whether different land cover scenarios influence the relative effect of $\Delta\overline{x_{i,j,T}}$ on $\Delta\overline{\mathrm{GPP}_{i,j,T}}$ differently across "dry" and "wet" years. Because the standard deviations are reasonably

similar between trials (see Supplemental Fig. 4.1), it is reasonable to use standardized regression coefficients to compare the relative effect of one variable in one scenario to another in a different scenario.

I used a series of linear models to make inference about the relationships between environmental predictors and GPP and LH flux. I first fit Ordinary Least Squares (OLS) linear models to relate how a standardized change in $\Delta\overline{\text{VPD}_{i,j,T}}$, $\Delta\overline{\text{SoilMoist.}_{i,j,T}}$,$\Delta\overline{\text{SW RAD.}_{i,j,T}}$, and $\Delta\overline{\text{Daily Prcp.}_{i,j,T}}$ imparts a standardized change in $\Delta\overline{\text{GPP}_{i,j,T}}$ across each trial and across "dry" and "wet" years. After identifying significant spatial autocorrelation using Moran's I (hovering near 0.5, see Supplemental Fig. 4.2), I employed the "spatialreg" and "spdep" R packages to fit spatial lag models and spatial error models, which account for spatial autocorrelation (Bivand et al. [2017]). Lag models assume that autocorrelation comes from the dependent variable, in this case $\Delta\overline{\text{GPP}_{i,j,T}}$, while error models assume it originates from unobserved phenomena (spatially-structured variables omitted from the model). However, this situation is unique because spatial autocorrelation, in both the predictors ($\Delta\overline{\text{VPD}_{i,j,T}}$, $\Delta\overline{\text{SoilMoist.}_{i,j,T}}$,$\Delta\overline{\text{SW RAD.}_{i,j,T}}$, and $\Delta\overline{\text{Daily Prcp.}_{i,j,T}}$) and the response ($\Delta\overline{\text{GPP}_{i,j,T}}$) is likely driven by the formation of clouds and localized convection-driven precipitation events. Since pixels within a storm experience similar atmospheric conditions, their responses are not dependent on immediate neighbors but on the storm itself. Consequently, the development and distribution of convective storms depends on pixel-to-pixel landscape features (elevation, albedo, soil moisture, etc.). These factors create spatial effects on storm occurrence and intensity, meaning precipitation exhibits spatial structure tied to underlying landscape features. This suggests that failing to account for spatial autocorrelation could misrepresent the relationships between the predictors and $\Delta\overline{\text{GPP}_{i,j,T}}$. The best models were selected using AIC values, and Moran's I, calculated on residuals was used to determine if spatial autocorrelation was adequately addressed within each model. I then used the same approach to relate $\Delta\overline{\text{GPP}_{i,j,T}}$ to $\Delta\overline{\text{LH Flux}_{i,j,T}}$, with the aim of demonstrating a feedback to

atmospheric phenomena through water being transported back to the atmosphere through GPP.

Chapter 3

Results & Discussion

3.1 Characterizing Environmental Conditions Throughout Focal Domain

Average environmental conditions throughout the focal domain clearly show 2017 to be the "dry" year and 2018 to be the "wet" year. Soil moisture, daily precipitation, and LH flux are higher in 2018 than in 2017. This is matched by a much larger VPD in 2017 than in 2018, and increased shortwave radiation at the surface (see Table 3.1).

Average Environmental Conditions Across the Focal Domain

Year	**VPD(Pa)**	**SWRAD(Wm^{-2})**	**S.Moist.(m^3m^{-3})**	**DailyPrcp.(mm)**
2017	861.1562	260.3207	0.2897	3.6613
2018	779.6536	254.0896	0.2964	4.0463
18(-)17	**-81.5026**	**-6.2311**	**0.0067**	**0.3850**

Table 3.1: Average values of relevant environmental variables for the 2017 & 2018 control runs. Supplemental Fig. 4.5 contains values for each individual simulation.

However, year to year means of environmental conditions fail to capture how physiography and synoptic weather interact to generate interesting spatial variation in these environmental conditions. For instance, topology and elevation shape the distribution of VPD (as seen in Fig. 3.1, (a) and (b)). The piedmont region sees a moderately consistent VPD around ∼900 Pa in both years, despite the bordering Blue Ridge having a VPD around ∼650 Pa both years. The Valley & Ridge region is comparatively "patchy," with small areas having low average VPD. The Appalachian Plateau exhibits significant variability, with high VPD in both years in the western portion of the region and low VPD in the northeast. These

trends are likely attributable to the elevation gradient throughout the different regions, as the Piedmont has a lower elevation than surrounding mountainous regions, leading to higher average temperatures due to the environmental lapse rate, contributing to a comparatively high VPD. The Blue Ridge is high elevation, and is characterized by comparatively lower temperatures forcing a lower VPD. The Valley & Ridge, consisting of bands of high mountains and valleys with low elevations, likely exhibits greater "patchiness" in VPD, in part, due to temperature gradients across substantial variation in elevation.

Soil moisture is similarly mediated by interactions with the landscape, though soil type has a pronounced influence soil moisture variation. Average soil moisture is lowest in "Sandy Loam" soils, found in the Piedmont and Appalachian Plateau, and highest in "Silt Loam" soils. This is likely due to the ability of silt loam soils hold water tighter than sandy loam. It is additionally possible, however, that soil moisture is associated with elevation, given higher temperatures associated with lower elevations in the Piedmont, which could lead to greater evaporation and soil water loss. Lastly, while there is notable variation in available SW radiation at the surface, which again can be attributed to the elevation gradient modulating the flow of vapor across the land surface, it is less pronounced than it is for VPD and soil moisture. Still, there is unique spatial variation present, most notably the lower average in the Piedmont in 2017 relative to the Blue Ridge. Interestingly, this pattern is not present in 2018. It is clear that without land surface modification, VPD, soil moisture, and available shortwave radiation demonstrate significant spatial variability due to land surface features.

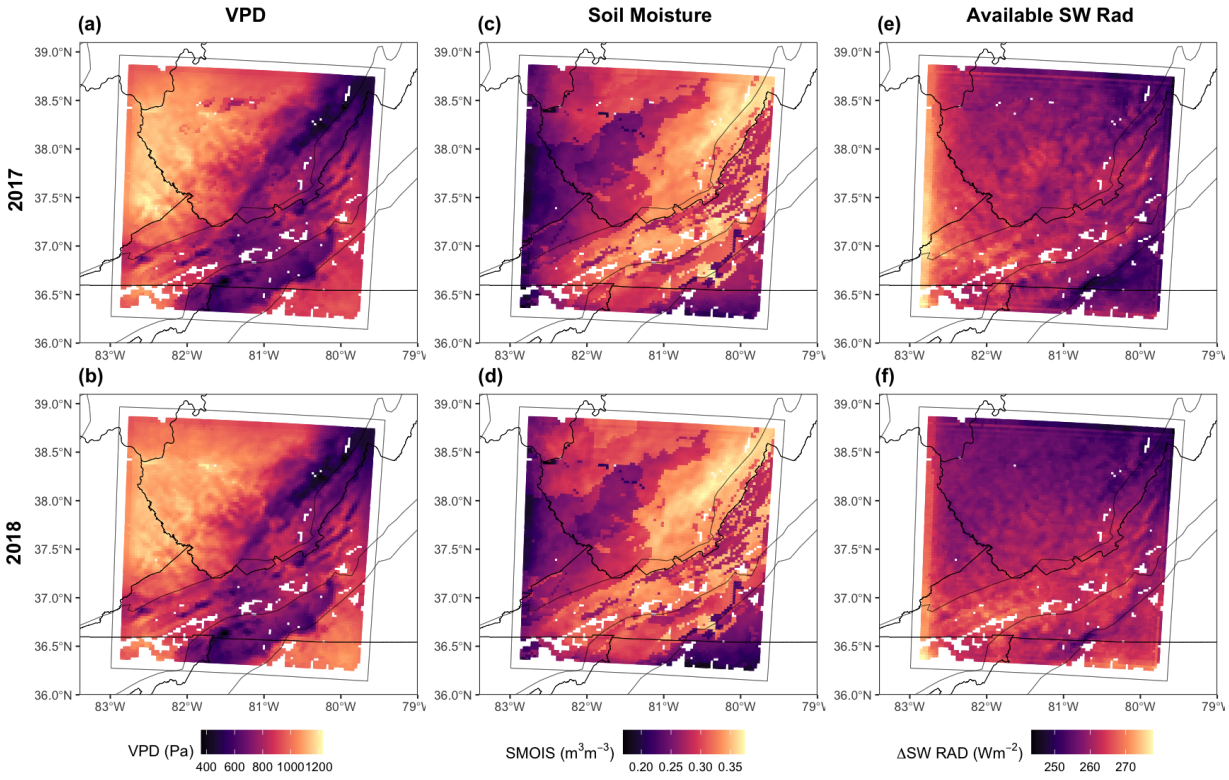

Figure 3.1: The per-pixel average VPD (a) & (b), Soil Moisture (c) & (d), and Available SW Radiation (e) & (f) for the 2017 and 2018 control trials. Variable arrangement of these environmental characteristics suggest physiography, primarily topography, elevation, and soil type play a significant role in distributing water vapor, soil moisture, and photosynthetically active radiation.

3.2 Characterizing Changes in Environmental Conditions Across Deforested Pixels and Remaining Deciduous Forest Pixels

3.2.1 Within Deforested Pixels

Deforestation induced substantial changes in environmental conditions, both atmospheric and terrestrial, within the deforested pixels. Across all deforestation scenarios, 10 m $u - v$ wind speeds increased by $\sim$0.4 ms^{-1} on average within the deforested pixels. Average wind direction was not different between between deforestation scenarios and controls in 2017, however average wind direction differed considerably between 2017 and 2018. Furthermore, deforestation scenarios have a slight impact on average wind direction in 2018 (Fig. 3.2). This increase in wind speed was expected, as the reduction in surface roughness from the land surface conversion decreases the frictional drag acting against the winds (Gandu et al. [2004]). The slight change in wind direction is also likely due to this reduction of surface roughness, as the vegetation could have deformed the prevailing winds. The average wind vector is well aligned with the major axis of land cover scenarios 001, 002, 003, and 004 (see Fig. 2.7).

2017 & 2018 Avg. $u - v$ Wind Velocity Vectors Across All Treatments

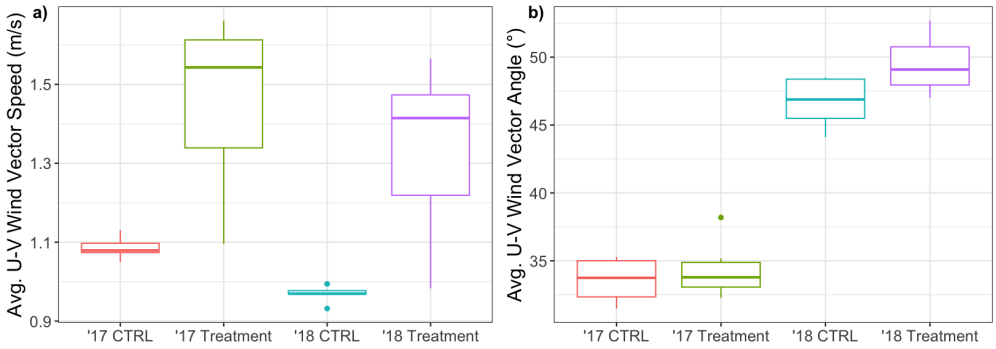

Figure 3.2: Comparison between control and treatment velocity vectors averaged across all 2017 and 2018 land cover scenarios. A significant increase in the magnitude of the wind vector between controls and treatments ($p < 0.01$) was found, but only a very small, marginally significant difference in θ ($p < 0.05$) was recovered. Mean wind speed & direction, 2017: 1.458 ms^{-1}, 34.348°. Mean wind speed & direction, 2018: 1.337 ms^{-1}, 49.458°.

VPD

Across all deforestation scenarios in 2017 and 2018, average growing season VPD appears to increase by ∼4% on average in deforested pixels (see Table 3.2). This is likely due to the altered surface energy partitioning of the "Barren or Sparsely Vegetated" pixels relative to "Temperate Deciduous Forest." Without the capacity for transpiration, deforested pixels will experience a substantial decline in transpiration from the loss of vegetation, limiting the flow of vapor back into the atmosphere. Furthermore, increased transpiration reduces temperature, which can limit convective storm formation. The change in a single pixel from control to treatment of average VPD, $\Delta\overline{\text{VPD}_{i,j,T}}$, is dependent on the pixel's radial direction, relative to the center of the focal domain and the prevailing $u-v$ wind direction (Fig. 3.3 and Fig. 3.4). For instance, the point of absolute minimum of $\Delta\overline{\text{VPD}_{i,j,T}}$ across all scenarios in both 2017 and 2018 is in the direction of the average wind vector. This means that moisture is being transported across the land surface in the direction of dominant winds. Additionally, average VPD decreases clockwise of the average wind vector and is higher counterclockwise.

Average Environmental Conditions In Deforested Pixels

Year	LC Applied?	VPD(Pa)	SWRAD(Wm^{-2})	S.Moist.(m^3m^{-3})	DailyPrcp.(mm)
2017	No	807.3279	260.7829	0.3077	4.0420
2017	Yes	840.5400	264.3757	0.2796	3.8458
2017	Delta	33.2121	3.5928	-0.0281	-0.1961
2018	No	728.7491	254.8222	0.3152	4.7311
2018	Yes	757.5173	259.0204	0.2911	4.4593
2018	Delta	28.7681	4.1983	-0.0242	-0.2719

Table 3.2: Average environmental conditions within *deforested* pixels, before (No) and after (Yes) the deforestation, and the difference between them (Delta). Supplemental Fig. 4.4 contains values for each individual simulation.

This is likely due to the prevailing winds that, in the Northern Hemisphere, veer clockwise with increasing height due to Ekman dynamics in the boundary layer (Lindvall and Svensson [2019]), resulting in moisture advection eastward.

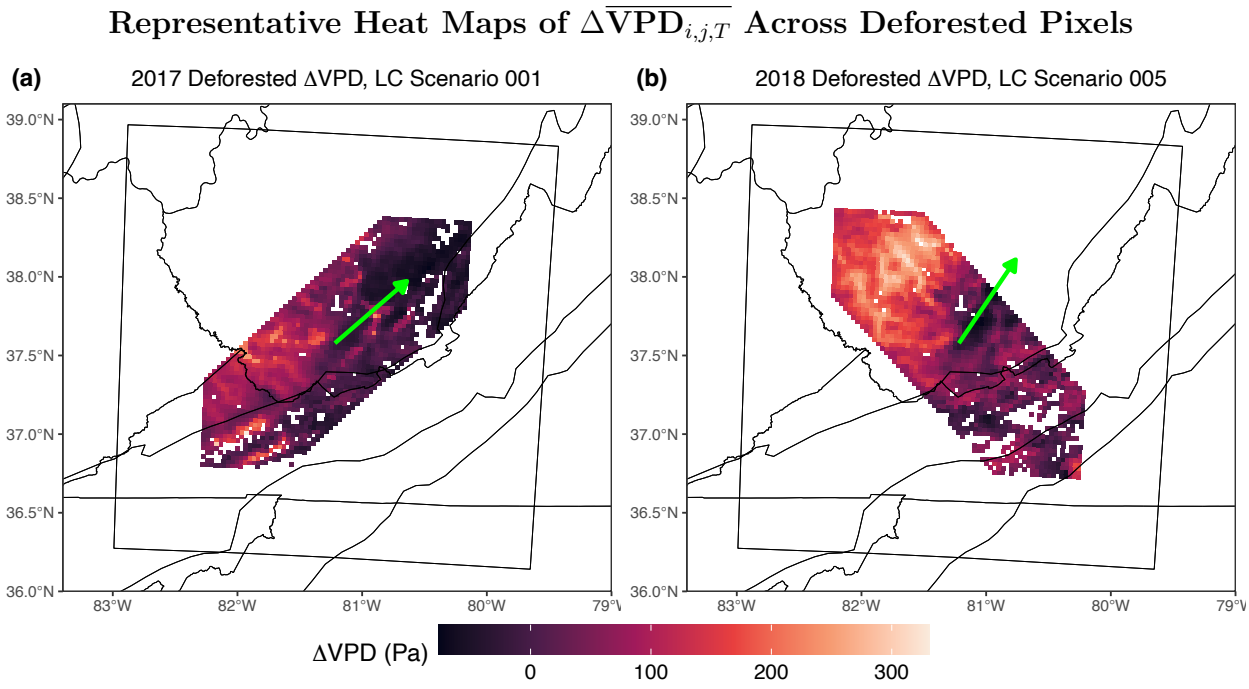

Figure 3.3: Heat maps of the difference between average VPD *before* and *after* deforestation across all deforested pixels ($\Delta\overline{\text{VPD}_{i,j,T}}$) for (a) Scenario 001 in 2017 and (b) Scenario 005 in 2018. Green arrows depicts the angle of the average prevailing 10-meter winds inside the deforested pixels, relative to the *east* (2017: 34.348°, 2018: 49.458°). For all heat maps, see Supplemental Figures 4.5 & 4.6.

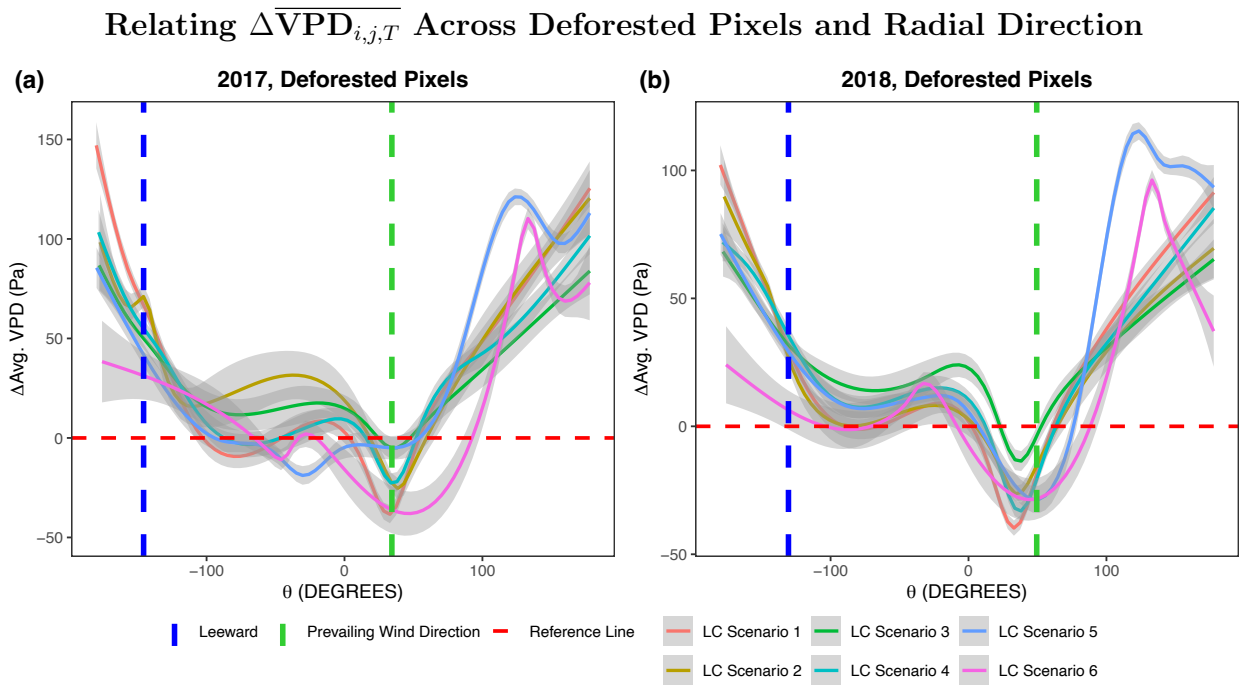

Figure 3.4: A series of GAMs/loess' relating the difference between average VPD *before* and *after* deforestation across all deforested pixels ($\Delta\overline{\text{VPD}_{i,j,T}}$) and radial direction, relative to the east, where $\theta = 0$. θ **increases** counterclockwise of the east and **decreases** clockwise from the east for both (a) 2017 and (b) 2018 trials. For more GAMs/loess' across the deforested pixels, see Supplemental Figures 4.1 & 4.2.

Soil Moisture

Across the growing season, average soil moisture declined in every deforested pixel across all scenarios in both 2017 and 2018. On average, across all scenarios, ∼9.1% in 2017 and ∼7.6% in 2018 (Table 3.2). This universal decline is a consequence of higher VPD and increased advective moisture transport, the loss of shade and roots that would otherwise limit soil water loss, and decreased precipitation (see below). These declines were not correlated with the pixel's radial direction relative to the center of the focal domain and the prevailing $u - v$ wind direction (Supplemental Figs. 4.1 & 4.2), rather these declines took place relatively uniformly across the deforested regions (Fig. 3.5). Additionally, there was minimal

scenario-to-scenario variation in average per-pixel changes in soil moisture. This suggests the mechanisms behind fluctuations in $\Delta\overline{\text{VPD}_{i,j,T}}$ and $\Delta\overline{\text{SoilMoist.}_{i,j,T}}$ are different, though deforestation is influencing both. Although notable, this is not especially unexpected, given that edaphic conditions are likely to respond to differently to deforestation than atmospheric conditions.

Representative Heat Maps of $\Delta\overline{\text{SoilMoist.}_{i,j,T}}$ Across Deforested Pixels

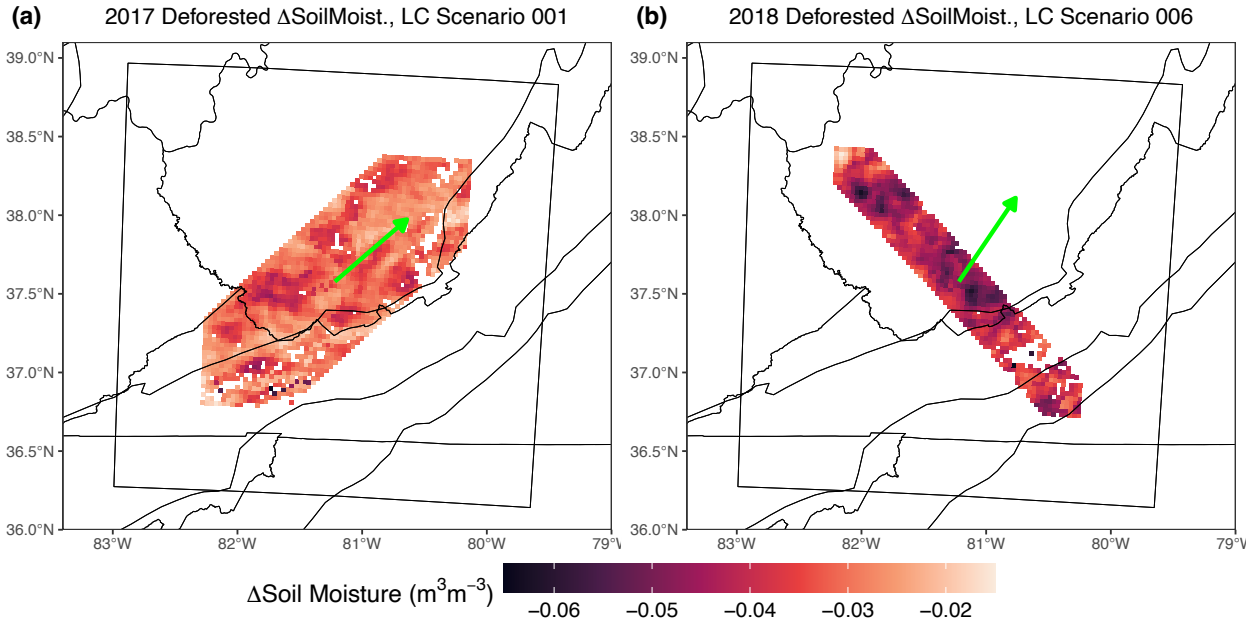

Figure 3.5: Heat maps of the difference between average soil moisture *before* and *after* deforestation across all deforested pixels ($\Delta\overline{\text{SoilMoist.}_{i,j,T}}$) for (a) Scenario 001 in 2017 and (b) Scenario 006 in 2018. Green arrows depicts the angle of the average prevailing 10-meter winds inside the deforested pixels, relative to the *east* (2017: 34.348°, 2018: 49.458°). For all heat maps, see Supplemental Figures 4.9 & 4.10.

Available Shortwave Radiation

Across all LC scenarios, average available shortwave radiation increased by ∼1.5% on average in deforested pixels (Table 3.2). Because the amount of available shortwave radiation is primarily influenced by cloud cover, the increase in available shortwave radiation suggests

both that the deforestation, by limiting transpiration, has reduced the flux of water vapor into the atmosphere, and that the altered surface energy balance may have reduced convection and cloud formation across the deforested pixels. Similar to soil moisture, however, there does not appear to be any spatial patterns associated with changes in per-pixel average available shortwave radiation, $\Delta\overline{\text{SW RAD.}}_{i,j,T}$ (Fig. 3.6). Despite being an atmospheric feedback to the land cover change, the mechanisms shaping the response of $\Delta\overline{\text{SW RAD.}}_{i,j,T}$ appear to be different than those shaping $\Delta\overline{\text{VPD}}_{i,j,T}$, another atmospheric feedback.

Representative Heat Maps of $\Delta\overline{\text{SW RAD.}}_{i,j,T}$ Across Deforested Pixels

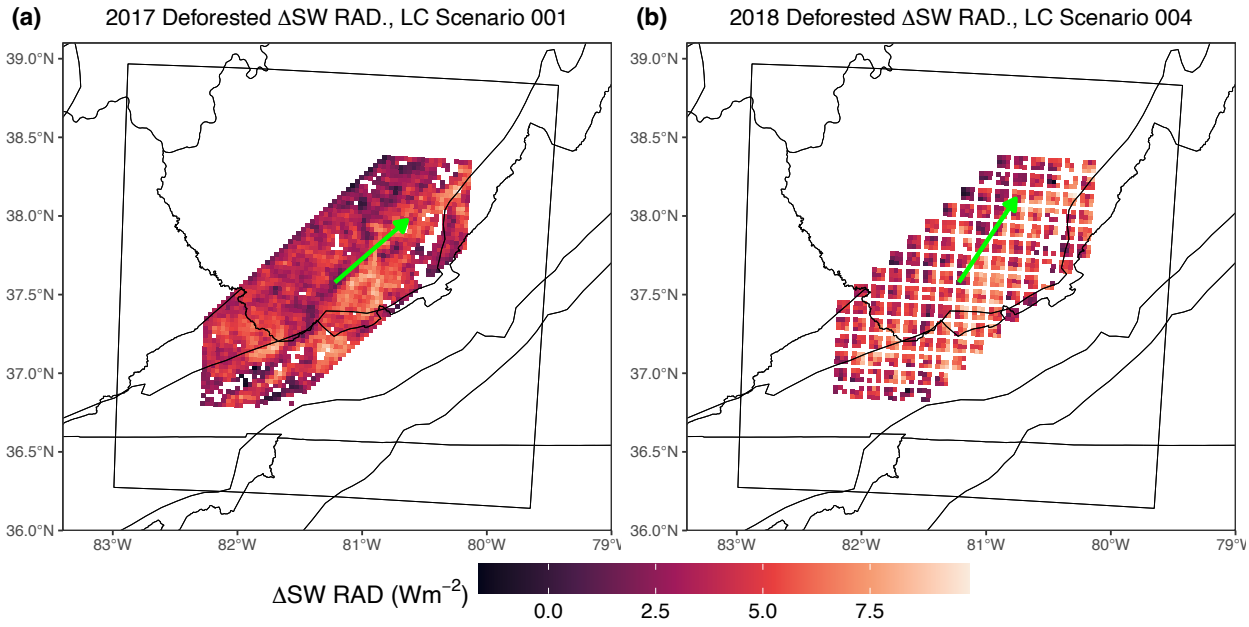

Figure 3.6: Heat maps of the difference between average available shortwave radiation *before* and *after* deforestation across all deforested pixels ($\Delta\overline{\text{SW RAD.}}_{i,j,T}$) for (a) Scenario 001 in 2017 and (b) Scenario 004 in 2018. Green arrows depicts the angle of the average prevailing 10-meter winds inside the deforested pixels, relative to the *east* (2017: 34.348°, 2018: 49.458°). For all heat maps, see Supplemental Figures 4.13 & 4.14.

Daily Precipitation

Rainfall, across all LC scenarios, decreased by ∼4.9% in 2017 and ∼5.7% in 2018 within deforested pixels (Table 3.2). This confirms a decline in convective precipitation, albeit minor, which can be attributed to both the loss of transpiration and the altered surface energy budget in the deforested pixels. Similar to $\Delta\overline{\text{SW RAD.}_{i,j,T}}$, changes in the per-pixel averages of daily precipitation, $\Delta\overline{\text{DailyPrcp.}_{i,j,T}}$, appears to be different than those shaping $\Delta\overline{\text{VPD}_{i,j,T}}$, despite atmospheric vapor being critical to both the development of clouds and rainfall.

Representative Heat Maps of $\Delta\overline{\text{Daily Prcp.}_{i,j,T}}$ Across Deforested Pixels

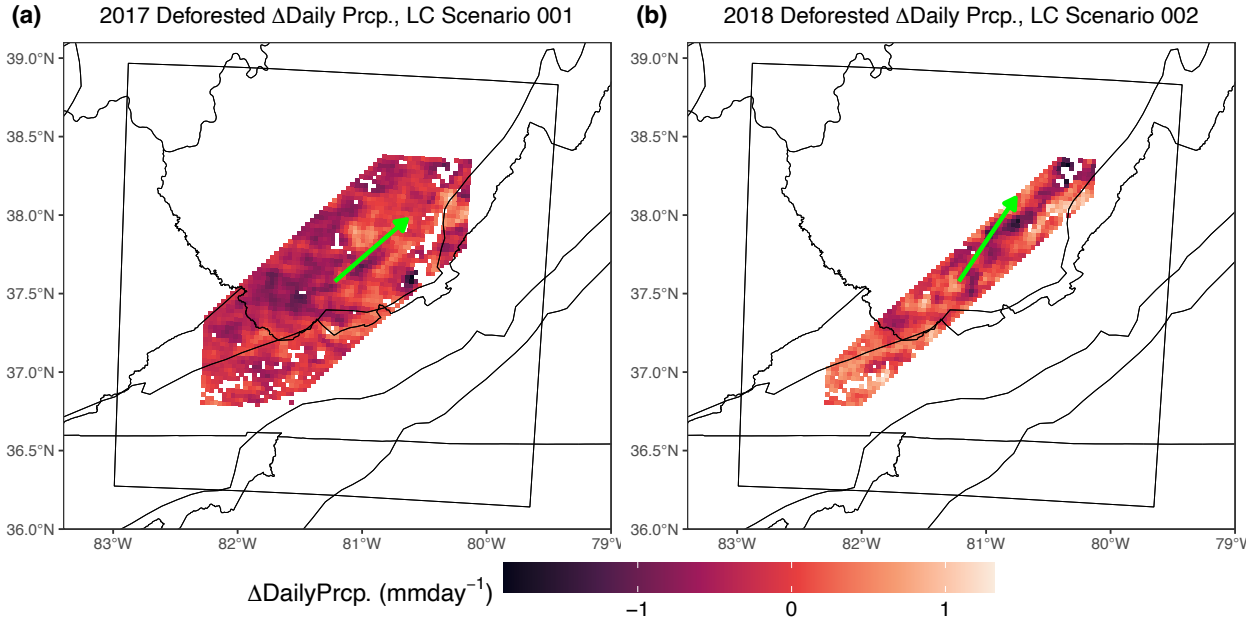

Figure 3.7: Heat maps of the difference between average daily precipitation *before* and *after* deforestation across all deforested pixels ($\Delta\overline{\text{DailyPrcp.}_{i,j,T}}$) for (a) Scenario 001 in 2017 and (b) Scenario 002 in 2018. Green arrows depicts the angle of the average prevailing 10-meter winds inside the deforested pixels, relative to the *east* (2017: 34.348°, 2018: 49.458°). For all heat maps, see Supplemental Figures 4.17 & 4.18.

Summary

Average growing season VPD, soil moisture, available shortwave radiation, and daily precipitation all change significantly in response to deforestation across the deforested pixels. $\Delta\overline{\text{VPD}_{i,j,T}}$ is asymmetric, with moisture advection moving decreasing VPD clockwise of the prevailing winds and increasing VPD counterclockwise of the prevailing winds. Average soil moisture declined in every deforested pixel across all deforestation scenarios, suggesting the loss of roots, shade, and transpiration increased the burden on soil moisture to satisfy evaporative demand. Average available shortwave radiation increased slightly across the deforested pixels, though it does not follow the clear spatial pattern changes in average VPD followed. Lastly, there were sizable changes in average daily precipitation across deforested pixels, likely due to a decreased flux of water vapor from lost transpiration and altered surface energy budget.

3.2.2 Within Remaining Deciduous Forest Pixels

Substantial changes in environmental conditions across the deforested pixels were expected, and the more interesting question is whether these effects spill over into the remaining deciduous forest pixels, driving changes in GPP and LH Flux. In short, environmental conditions changed in response to deforestation, but to a small degree, in remaining deciduous forest pixels. Average VPD, soil moisture, and daily precipitation all declined, but by $\leq$1%, while average available shortwave radiation increased by <1% (Table 3.3). The direction of these changes are generally consistent with what our analysis of the deforested pixels found. However, the magnitude of these changes suggests that the remaining deciduous forest and atmosphere, as a whole, exhibit remarkable stability in response to significant deforestation. However, there is scenario-to-scenario variation and significant pixel-to-pixel variation within each scenario that averages fail to capture, including significant radial variation and variation with distance from the center of the focal domain.

Average Environmental Values in Remaining Deciduous Forest

Year	LC Applied?	VPD(Pa)	SWRAD(Wm^{-2})	S.Moist.(m^3m^{-3})	DailyPrcp.(mm)
2017	No	871.5590	260.2052	0.2861	3.5831
2017	Yes	870.4085	260.2946	0.2853	3.5717
2017	Delta	-1.1506	0.0894	-0.0008	-0.0114
2018	No	788.6834	253.9339	0.2928	3.9129
2018	Yes	786.8223	254.0495	0.2922	3.8880
2018	Delta	-1.8611	0.1156	-0.0006	-0.0249

Table 3.3: Average values of relevant environmental variables for each year, control (No) and treatment (Yes), for the deciduous forest pixels that were not removed/deforested. Supplemental Fig. 4.5 contains values for each individual simulation.

VPD

Similar to changes in average VPD across deforested pixels, the difference in VPD between *before* and *after* the deforestation across the remaining deciduous forest pixels ($\Delta\overline{\text{VPD}_{i,j,T}}$) demonstrates significant spatial variation relative to the internal prevailing wind direction (Fig. 3.8). This, again, is likely a consequence of Ekman dynamics in the boundary layer advecting moisture eastward. This eastward decrease in VPD (negative $\Delta\overline{\text{VPD}_{i,j,T}}$) from control-to-treatment suggests atmospheric water availability increases and evaporative demand decreases to the east, potentially reducing plant stress and increasing stomatal conductance and photosynthesis. For instance, there is a consistent decrease in VPD relative to the control across the different physiographic regions in the southeast corner of the domain. Given the variation in control VPD between the different physiographic regions in the southeastern corner (see Fig. 3.1), the uniform changes in VPD must stem from the deforestation in 001. The opposite is observed counterclockwise of the prevailing wind direction (Fig. 3.9), with slight, uniform decreases in VPD. Additionally, these results suggest the radial changes in VPD depend on the size (magnitude of changes larger for 001 than for 002, and for 005 than for 006), spatial orientation (the pattern exhibited by 001 and 002 is different than 005

and 006, respectively) of deforestation, can be muted by discontinuities (the amplitude of 003 and 004 are significantly less than 001), and the amplitude of the perturbation appears to be greater in the "dry" year (the magnitude of the GAMs is lower in 2018, see 005 and 006). However, it is intriguing that all deforestation scenarios across both "wet" and "dry" years redistribute atmospheric moisture across the remaining forested pixels in a manner that results in minimal changes on average throughout the focal domain. This suggests the total vapor in the atmosphere is changing very little, but rather the more pronounced change is where the vapor is going.

As distance from the center of the focal domain increases, the magnitude of $\Delta\overline{\mathrm{VPD}_{i,j,T}}$ decreases and gradually attenuates towards zero (Fig. 3.10). Some scenarios appear to have a steeper curve of attenuation than others and appears to strongly depend on the size of the deforested region. For instance, deforestation scenario 001 has the highest abs($\Delta\overline{\mathrm{VPD}_{i,j,T}}$) 50km away from the center of the focal domain, followed by scenarios 004 and 005. The smallest scenarios, 002, 003, and 006, see much smaller changes to abs($\Delta\overline{\mathrm{VPD}_{i,j,T}}$). 150 km away, however, the different deforestation scenarios see approximately equivalent perturbations. Simply, the deforestation generates a pronounced and consistent spatial shift in VPD in the remaining forest pixels, with the magnitude of this effect determined by the spatial extent of the deforestation. Irrespective of this, however, the effects of the deforestation scenario attenuate a couple hundred kilometers away.

Representative Heat Maps of $\Delta\overline{\text{VPD}_{i,j,T}}$ Across Remaining Deciduous Forest Pixels

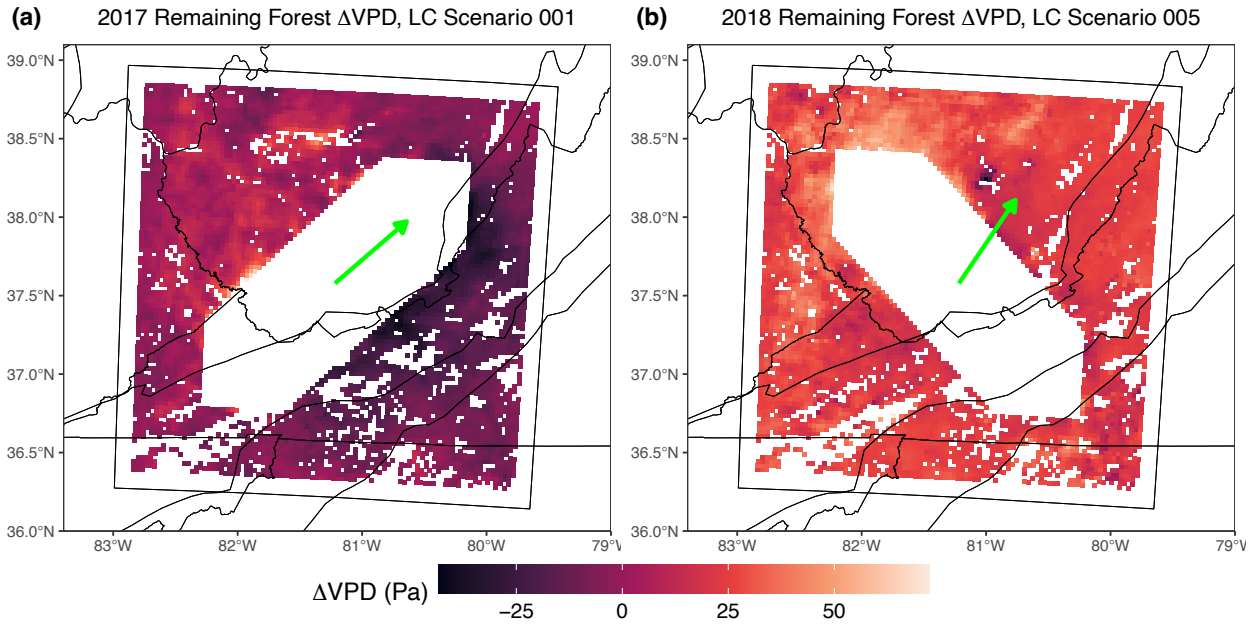

Figure 3.8: Heat maps of the difference between average VPD *before* and *after* deforestation across all remaining deciduous forest pixels ($\Delta\overline{\text{VPD}_{i,j,T}}$) for (a) Scenario 001 in 2017 and (b) Scenario 005 in 2018. Green arrows depicts the angle of the average prevailing 10-meter winds inside the deforested pixels, relative to the *east* (2017: 34.348°, 2018: 49.458°). For all heat maps, see Supplemental Figures 4.7 & 4.8.

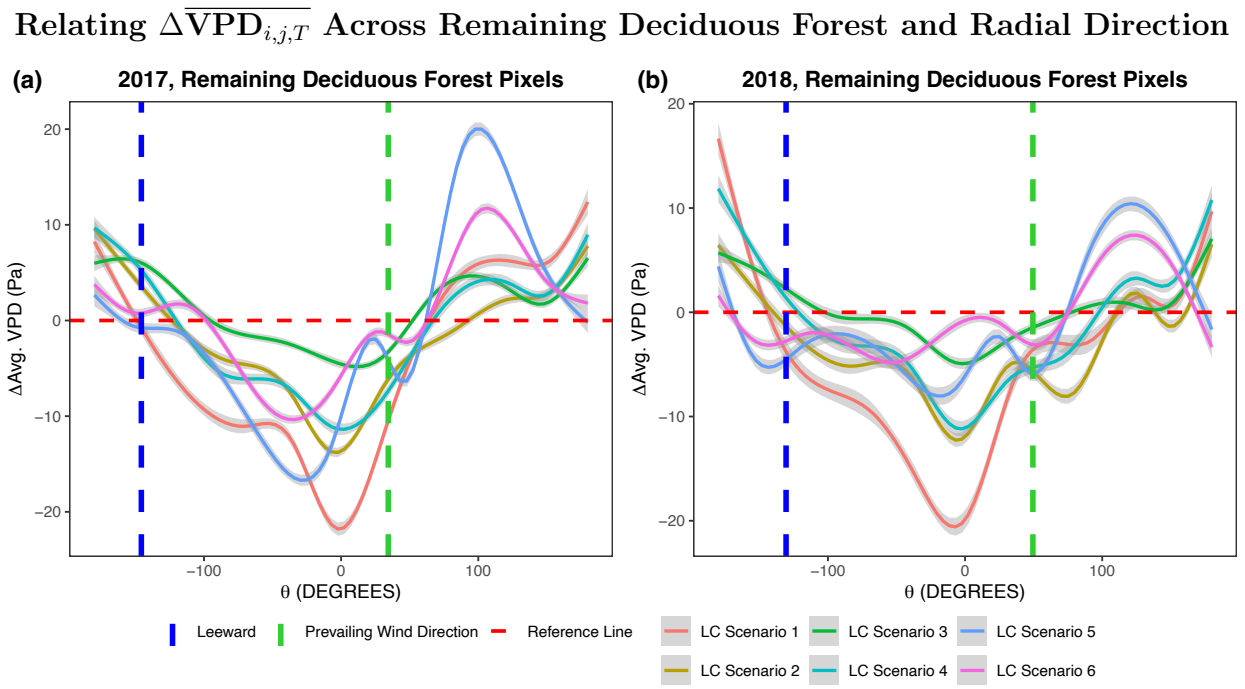

Figure 3.9: A series of GAMs/loess' relating the difference between average VPD *before* and *after* deforestation across all remaining deciduous forest pixels ($\Delta\overline{\text{VPD}_{i,j,T}}$) and radial direction, relative to the east, where $\theta = 0$. θ **increases** counterclockwise of the east and **decreases** clockwise from the east for both (a) 2017 and (b) 2018 trials. For more GAMs/loess' relating changes in environmental characteristics to radial direction in remaining deciduous forest pixels, see Supplemental Figures 4.3 & 4.4.

Relating abs($\Delta\overline{\text{VPD}_{i,j,T}}$) Across Remaining Deciduous Forest Pixels and Distance From Center of Focal Domain

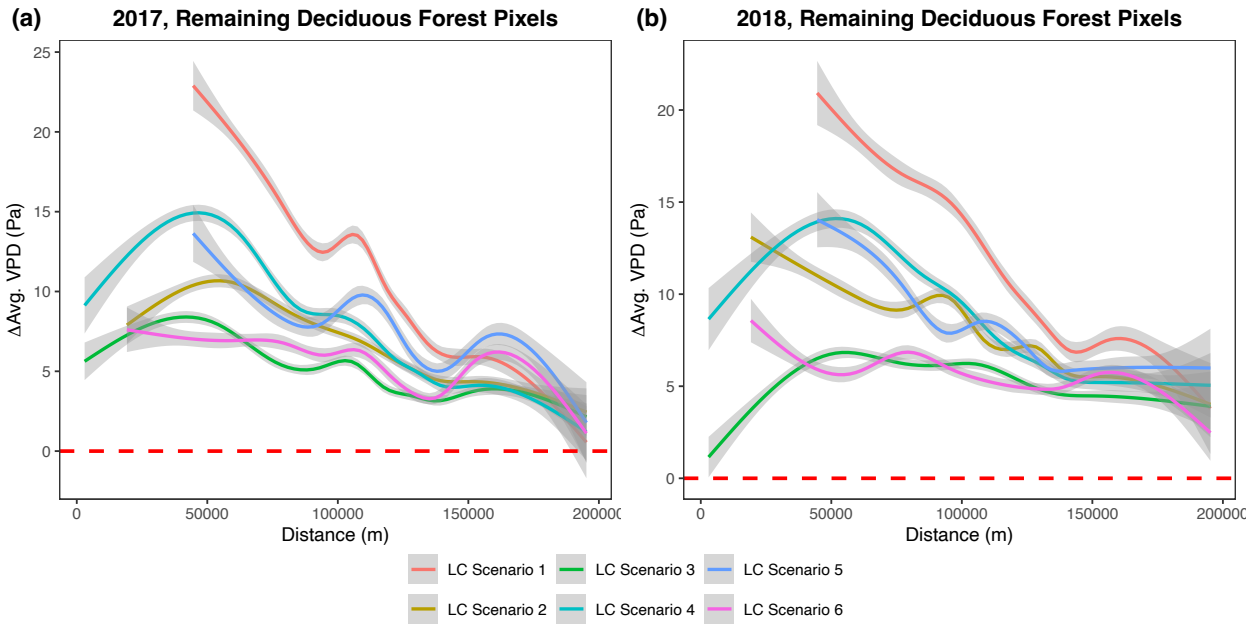

Figure 3.10: A series of GAMs/loess' relating the absolute value of the difference between average VPD *before* and *after* deforestation across all remaining deciduous forest pixels (abs($\Delta\overline{\text{VPD}_{i,j,T}}$)) and linear distance from the center of the focal domain in meters for both (a) 2017 and (b) 2018 trials.

Soil Moisture

Similar to average soil moisture across deforested pixels, changes between the *before* and *after* average of soil moisture across remaining forested regions ($\Delta\overline{\text{SoilMoist.}_{i,j,T}}$), which are small, do not appear to depend on the direction of the prevailing winds, nor on the size, spatial orientation, or continuity of the deforestation scenario (Fig. 3.11). While there are "patches" of large increases and decreases in soil moisture, it is difficult to determine consistent patterns across different scenarios or a direct source of this variation, beyond being a consequence of increased atmospheric instability and slightly altered precipitation patterns (see precipitation Fig. 3.15). As a whole, soil moisture changed very little and unpredictably. Interestingly, however, as distance increases from the center of the focal domain, the magnitude of $\Delta\overline{\text{SoilMoist.}_{i,j,T}}$, abs($\Delta\overline{\text{SoilMoist.}_{i,j,T}}$), does not decrease and attenuate towards zero (Fig. 3.12). Rather, soil moisture continues to be perturbed far away from the center of the focal domain. The lack of attenuation suggests that the effects of deforestation on soil moisture can ripple outward a considerable distance, potentially influencing hydrology hundreds of kilometers away. There does not appear to be any significant impact of the size, spatial orientation, or continuity of the deforested region on the impact on soil moisture. This is likely due to the dependency of soil moisture on a multitude of factors (e.g. precipitation, runoff, vertical infiltration, and evapotranspiration) (see Noah soil moisture scheme utilized by Noah-MP: Ek et al. [2003]).

Representative Heat Maps of $\Delta\overline{\text{SoilMoist.}_{i,j,T}}$ Across Remaining Deciduous Forest Pixels

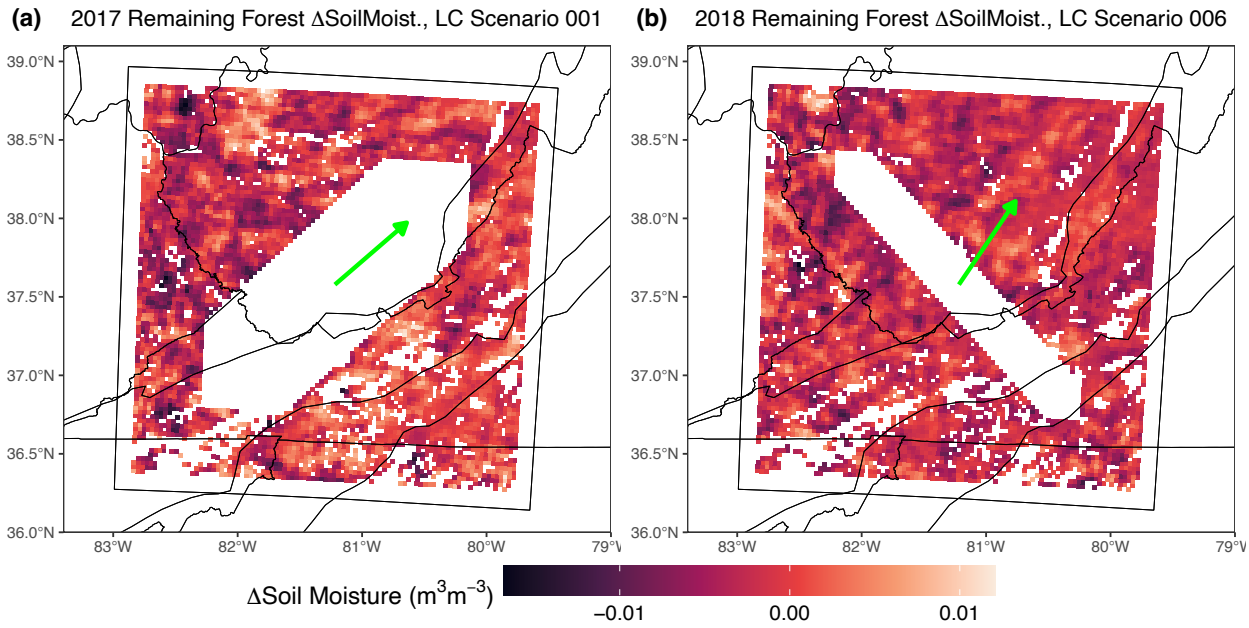

Figure 3.11: Heat maps of the difference between average soil moisture *before* and *after* deforestation across all remaining deciduous forest pixels ($\Delta\overline{\text{SoilMoist.}_{i,j,T}}$) for (a) Scenario 001 in 2017 and (b) Scenario 006 in 2018. Green arrows depicts the angle of the average prevailing 10-meter winds inside the deforested pixels, relative to the *east* (2017: 34.348°, 2018: 49.458°). For all heat maps, see Supplemental Figures 4.11 & 4.12.

Relating abs($\Delta\overline{\text{SoilMoist.}_{i,j,T}}$) Across Remaining Deciduous Forest Pixels and Distance From Center of Focal Domain

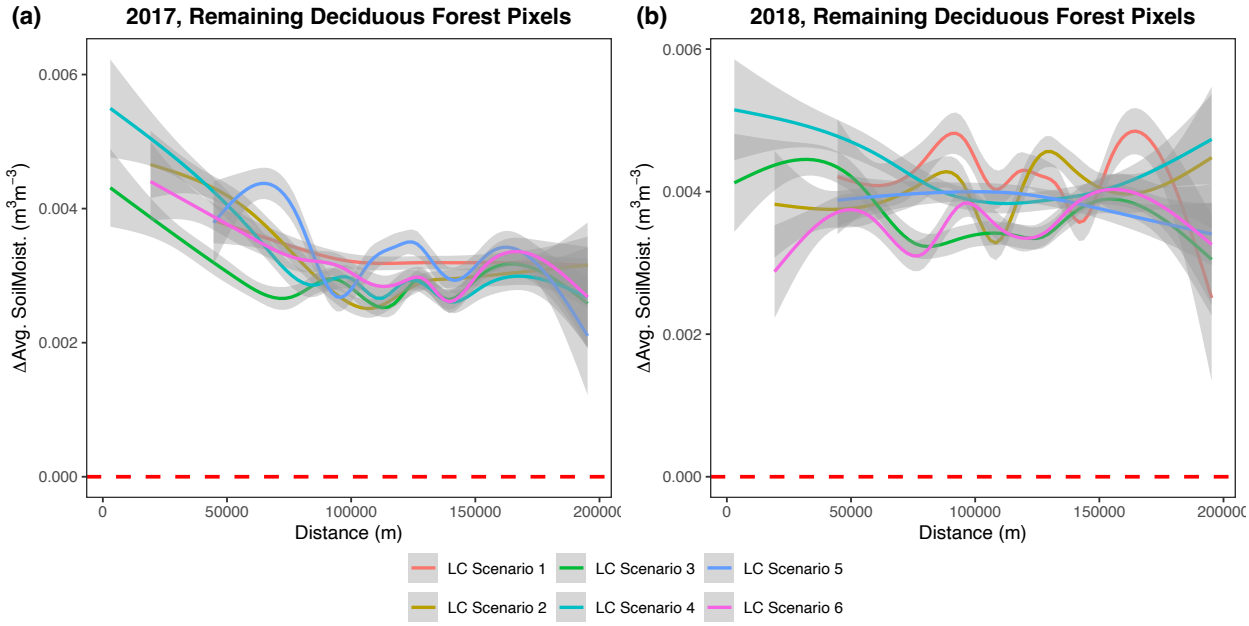

Figure 3.12: A series of GAMs/loess' relating the absolute value of the difference between average soil moisture *before* and *after* deforestation across all remaining deciduous forest pixels (abs($\Delta\overline{\text{SoilMoist.}_{i,j,T}}$)) and linear distance from the center of the focal domain in meters for both (a) 2017 and (b) 2018 trials. For all heat maps, see Supplemental Figures 4.11 & 4.12.

Available Shortwave Radiation

Similar to available shortwave radiation across the deforested pixels, the difference between the *before* and *after* average of available shortwave radiation across remaining forested regions ($\Delta\overline{\text{SW RAD.}_{i,j,T}}$) appears to change little on average, despite significant pixel-to-pixel variation (Fig. 3.13). There does not appear to be any spatial dependence relative to the direction of the prevailing winds. However, across both 2017 and 2018, the magnitude of $\Delta\overline{\text{SW RAD.}_{i,j,T}}$ is hightest at the edges of the deforested pixels and decreases with distance (Fig. 3.14), similar to $\Delta\overline{\text{VPD}_{i,j,T}}$. This suggests fluctuations in cloud cover are occurring

close the boundary between the different land use types, "Barren or Sparsely Vegetated" and "Temperate Deciduous Forest". Vertical motion is known to fluctuate at the convergence of different land cover types (Cheng and McColl [2023]), though the resolution of the model limited the ability to identify specific spatial trends in changes in vertical flux changes (see Supplemental Figs. 4.1, 4.2, 4.3, & 4.4). However, this perturbation in available shortwave radiation at the edges of the remaining deciduous forest, which is highest for the largest deforestation scenarios (001, 004, and 005) suggest vertical motion and convection has been impacted at the land cover boundary. As distance increases from the deforested region, abs($\Delta\overline{\text{SW RAD.}}_{i,j,T}$) approached zero, and any such effects effectively disappear.

Representative Heat Maps of $\Delta\overline{\text{SW RAD.}}_{i,j,T}$ Across Remaining Deciduous Forest Pixels

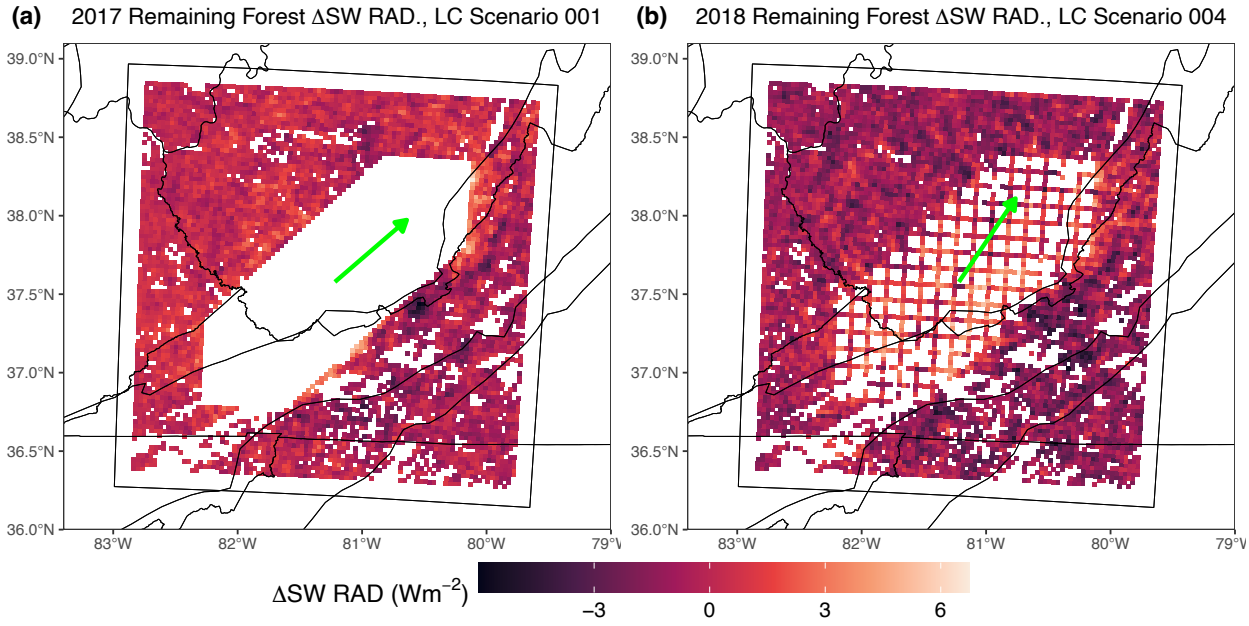

Figure 3.13: Heat maps of the difference between average available shortwave radiation *before* and *after* deforestation across all remaining deciduous forest pixels ($\Delta\overline{\text{SW RAD.}}_{i,j,T}$) for (a) Scenario 001 in 2017 and (b) Scenario 004 in 2018. Green arrows depicts the angle of the average prevailing 10-meter winds inside the deforested pixels, relative to the *east* (2017: 34.348°, 2018: 49.458°). For all heat maps, see Supplemental Figures 4.15 & 4.16.

Relating abs($\Delta\overline{\text{SW RAD.}}_{i,j,T}$) Across Remaining Deciduous Forest Pixels and Distance From Center of Focal Domain

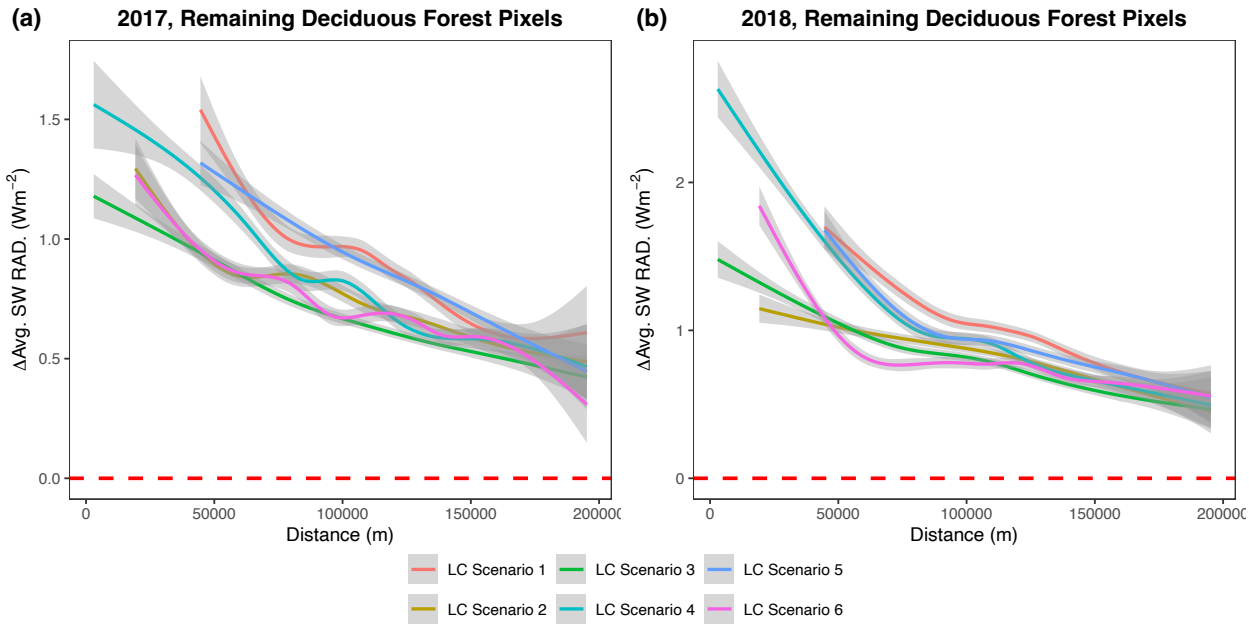

Figure 3.14: A series of GAMs/loess' relating the absolute value of the difference between average available shortwave radiation *before* and *after* deforestation across all remaining deciduous forest pixels (abs($\Delta\overline{\text{SW RAD.}}_{i,j,T}$)) and linear distance from the center of the focal domain in meters for both (a) 2017 and (b) 2018 trials.

Daily Precipitation

Daily precipitation changes little on average. However, similar to the other atmospheric and edaphic features in the remaining deforested region, there appears to be a significant amount of pixel-to-pixel variation in the difference between daily precipitation *before* and *after* the deforestation, or $\Delta\overline{\text{Daily Prcp.}_{i,j,T}}$ (Fig. 3.15). These fluctuations are likely due to changes in cloud formation as indicated by $\Delta\overline{\text{SW RAD.}_{i,j,T}}$ and changes in atmospheric moisture indicated by $\Delta\overline{\text{VPD}_{i,j,T}}$. Similar to both abs($\Delta\overline{\text{VPD}_{i,j,T}}$) and abs($\Delta\overline{\text{SW RAD.}_{i,j,T}}$), the absolute value of $\Delta\overline{\text{Daily Prcp.}_{i,j,T}}$, abs($\Delta\overline{\text{Daily Prcp.}_{i,j,T}}$), decreases with distance from the center of the focal domain, suggesting that changes in daily precipitation induced by the different deforestation schemes in the remaining deciduous forest pixels attenuate to zero with distance (Fig. 3.16). There does not appear to be significant variation between the different deforestation schemes on the magnitude of the perturbation to daily precipitation in remaining deciduous forest pixels, perhaps due to the formulation of precipitation in WRF being dependent on a myriad of factors, similar to soil moisture.

Representative Heat Maps of $\Delta\overline{\text{Daily Prcp.}}_{i,j,T}$ Across Remaining Deciduous Forest Pixels

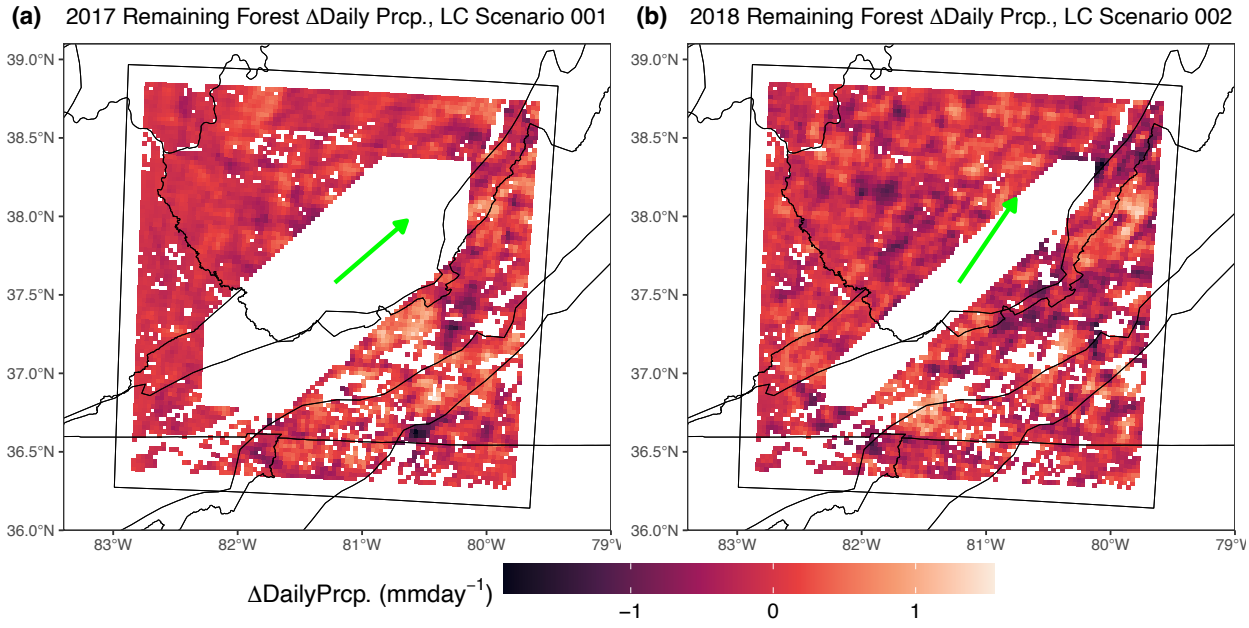

Figure 3.15: Heat maps of the difference between average daily precipitation *before* and *after* deforestation across all remaining deciduous forest pixels ($\Delta\overline{\text{DailyPrcp.}}_{i,j,T}$) for (a) Scenario 001 in 2017 and (b) Scenario 002 in 2018. Green arrows depicts the angle of the average prevailing 10-meter winds inside the deforested pixels, relative to the *east* (2017: 34.348°, 2018: 49.458°). For all heat maps, see Supplemental Figures 4.19 & 4.20.

Relating abs($\Delta\overline{\text{Daily Prcp.}}_{i,j,T}$) Across Remaining Deciduous Forest Pixels and Distance From Center of Focal Domain

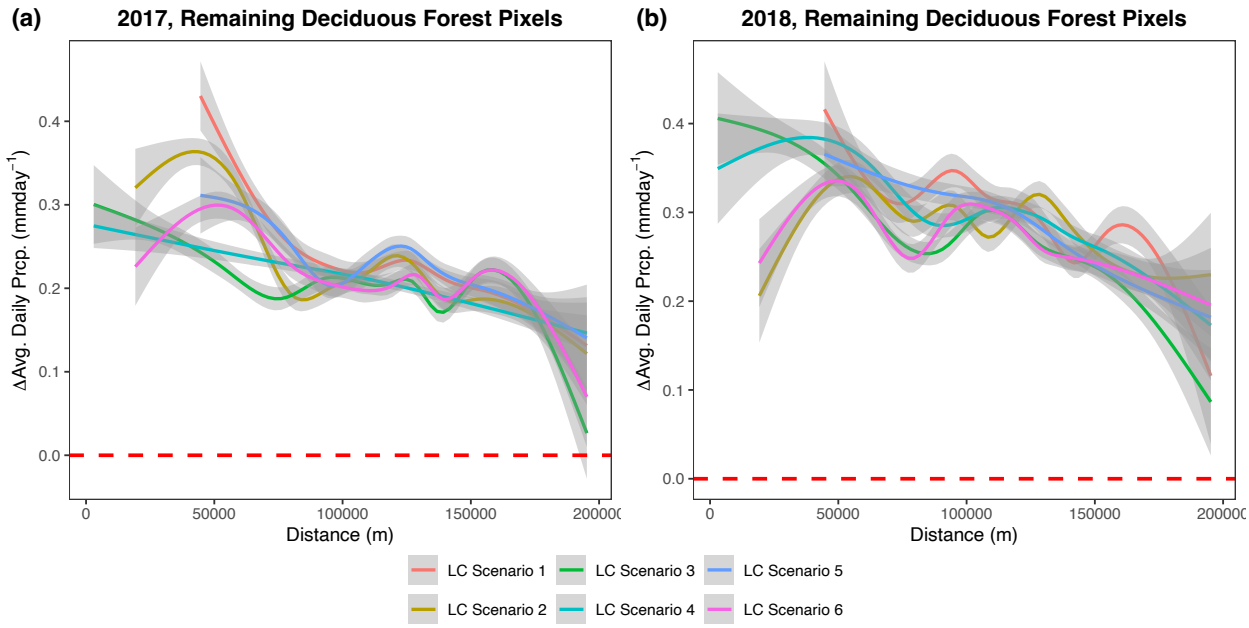

Figure 3.16: A series of GAMs/loess' relating the absolute value of the difference between average daily precipitation *before* and *after* deforestation across all remaining deciduous forest pixels (abs($\Delta\overline{\text{Daily Prcp.}}_{i,j,T}$)) and linear distance from the center of the focal domain in meters for both (a) 2017 and (b) 2018 trials.

Summary

Despite environmental conditions changing mininally on average across all remaining temperate deciduous forest pixels in the focal domain, there is significant pixel-to-pixel variation in both the average atmospheric (VPD, available shortwave radiation, and daily precipitation) and edaphic (soil moisture) conditions. Changes in average atmospheric conditions were most pronounced in the remaining deciduous forest pixels closest to the center of the focal domain, suggesting the atmospheric consequences of the different deforestation scenarios attenuate with distance. Changes in average soil moisture, however, did not attenuate with distance, and appeared to be relatively uniform across the remaining pixels and

land cover scenarios. Average VPD appeared to decrease eastward of the deforested region and increase westward, a consequence of moisture advection due to Ekman dynamics in the boundary layer, reducing atmospheric moisture in the western portion of the domain and increasing it in the east.

Size, spatial orientation, and continuity all appeared to play a role in shaping the response of average VPD across the different deforestation scenarios, with larger, continuous scenarios aligned with the direction of the prevailing winds having the greatest effect. Size played an additionally critical role in shaping the response of average available shortwave radiation across the remaining forested pixels. In contrast, size, spatial orientation, or continuity exerted little influence on average soil moisture or average daily precipitation. Additionally, the results do not suggest any significant influence of "wet" versus "dry" years on the perturbation of these environmental conditions, with the exception of VPD.

3.3 Characterization of Spatial Variation & Environmental Influence on Changes in GPP

Average GPP Across Remaining Deciduous Forest Pixels

Year	LC Applied?	GPP ($gCm^{-2}hr^{-}1$)
2017	No	0.2969
2017	Yes	0.2964
2017	Delta	-0.0005
2018	No	0.2862
2018	Yes	0.2857
2018	Delta	-0.0005

Table 3.4: Average values of GPP for each year, control (No) and treatment (Yes), for the deciduous forest pixels that were not removed/deforested. Supplemental Fig. 4.5 contains values for each individual simulation.

Similar to the average environmental conditions, the average response of GPP in the remaining deciduous forest pixels to deforestation was small (Table 3.4). A change of -

0.0005 gC m^{-2} hr^{-1} in GPP corresponds to to a shift of -0.02916 MgC ha^{-1} (≈-0.2% change) over the entire growing season. This, coupled with minimal changes in VPD, soil moisture, and available shortwave radiation, speaks to the resiliency of the landscape to significant landscape alteration close by. Recognizing the substantial pixel-to-pixel and simulation-to-simulation variability in atmospheric and edaphic conditions across the remaining deciduous forest pixels, we might expect the difference between the *before* and *after* average of GPP across remaining forested regions $\Delta\overline{\text{GPP}_{i,j,T}}$, to exhibit similar variability, as GPP depends on these environmental characteristics. However, $\Delta\overline{\text{GPP}_{i,j,T}}$ does not appear to be influenced by the prevailing wind direction (Figs. 3.17 & 3.18), suggesting a limited correlation with $\Delta\overline{\text{VPD}_{i,j,T}}$. Additionally, abs($\Delta\overline{\text{GPP}_{i,j,T}}$) changes with distance do not attenuate ∼200 kilometers from the center of the focal domain, unlike for abs($\Delta\overline{\text{VPD}_{i,j,T}}$) abs($\Delta\overline{\text{SW RAD.}_{i,j,T}}$) (Fig. 3.19). abs($\Delta\overline{\text{GPP}_{i,j,T}}$) appears to behave very similarly to abs($\Delta\overline{\text{SoilMoist.}_{i,j,T}}$) in with deviations from the control scenarios persisting hundreds of kilometers away from the site of deforestation, suggesting $\Delta\overline{\text{Soil Moist.}_{i,j,T}}$ may exercise the most pronounced control over $\Delta\overline{\text{GPP}_{i,j,T}}$ across the focal domain during the 2017 and 2018 growing seasons.

Representative Heat Maps of $\Delta\overline{\text{GPP}_{i,j,T}}$ Across Remaining Deciduous Forest Pixels

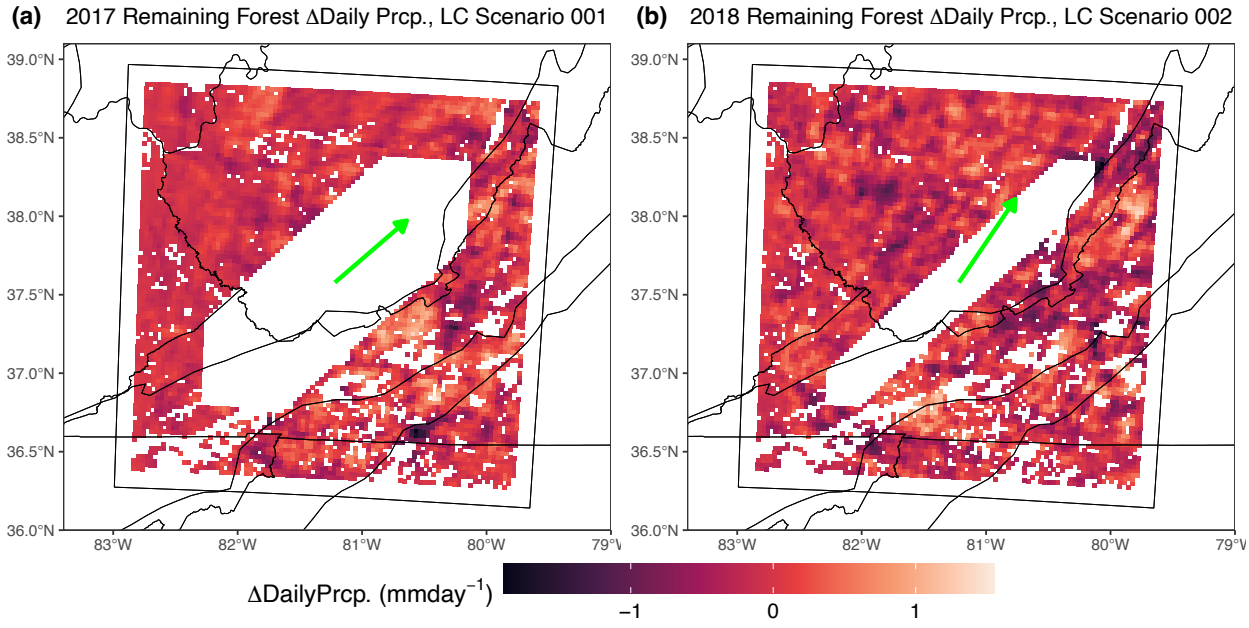

Figure 3.17: Heat maps of the difference between average daily precipitation *before* and *after* deforestation across all remaining deciduous forest pixels ($\Delta\overline{\text{GPP}_{i,j,T}}$) for (a) Scenario 001 in 2017 and (b) Scenario 006 in 2018. Green arrows depicts the angle of the average prevailing 10-meter winds inside the deforested pixels, relative to the *east* (2017: 34.348°, 2018: 49.458°). For all heat maps, see Supplemental Figures 4.21 & 4.22.

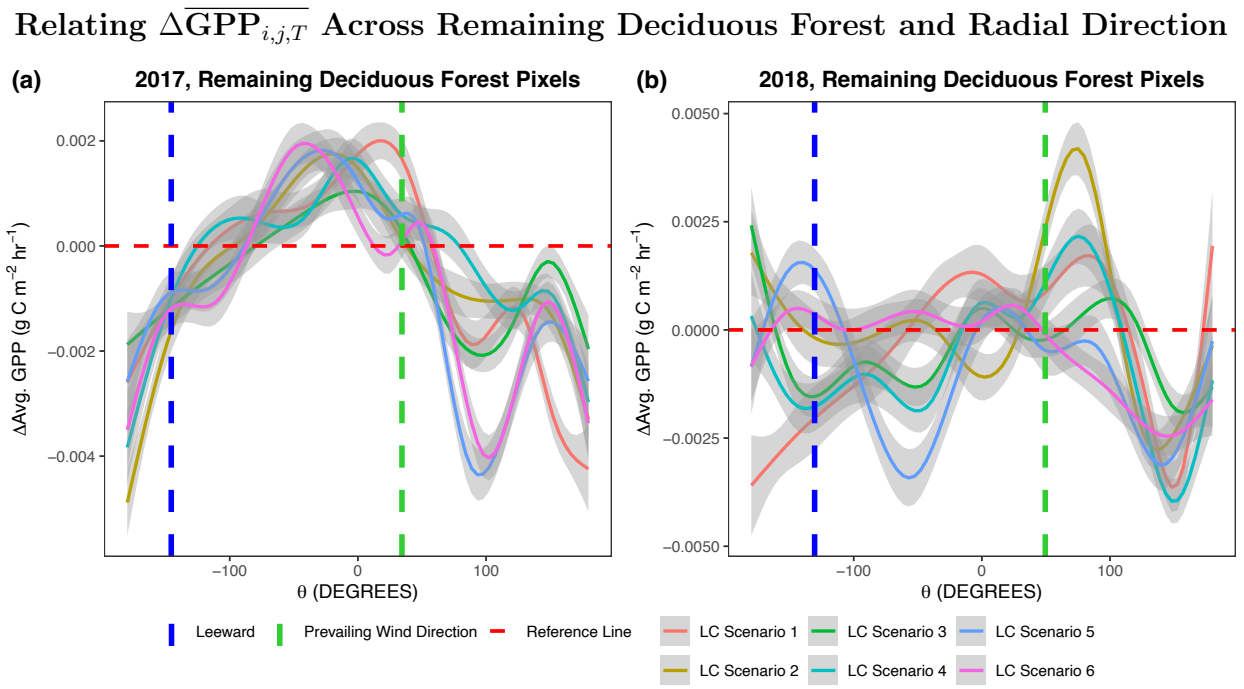

Figure 3.18: A series of GAMs/loess' relating the difference between average GPP *before* and *after* deforestation across all remaining deciduous forest pixels ($\Delta\overline{\text{GPP}_{i,j,T}}$) and radial direction, relative to the east, where $\theta = 0$. θ **increases** counterclockwise of the east and **decreases** clockwise from the east.

Relating abs($\Delta\overline{\text{GPP}_{i,j,T}}$) Across Remaining Deciduous Forest and Distance From Center

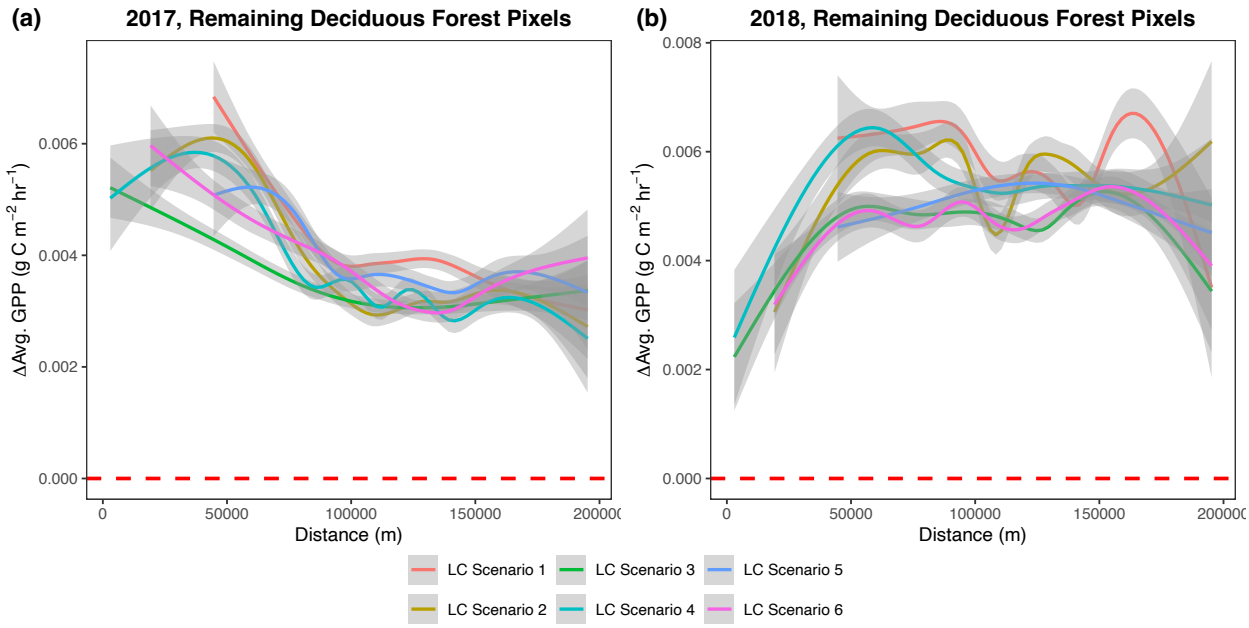

Figure 3.19: A series of GAMs/loess' relating the absolute value of the difference between average GPP *before* and *after* deforestation across all remaining deciduous forest pixels (abs($\Delta\overline{\text{GPP}_{i,j,T}}$)) and linear distance from the center of the focal domain in meters for both (a) 2017 and (b) 2018 trials.

Despite little variation in average GPP across LC scenarios (Table 3.4), $\Delta\overline{\text{GPP}_{i,j,T}}$ exhibits substantial spatial variation that's different across scenarios that is well predicted by $\Delta\overline{\text{VPD}_{i,j,T}}$, $\Delta\overline{\text{Soil Moist.}_{i,j,T}}$, $\Delta\overline{\text{SW RAD.}_{i,j,T}}$, and $\Delta\overline{\text{Daily Prcp.}_{i,j,T}}$. Relative variation in soil moisture differences were most strongly associated with relative variation in GPP differences; the normalized coefficient for $\Delta\overline{\text{SoilMoist.}_{i,j,T}}$ was the largest out of all predictors for all deforestation scenarios. The spatial variation in $\Delta\overline{\text{GPP}_{i,j,T}}$, which is explicitly addressed by the spatial error model, indicates that GPP has pronounced patches of significant high and low values, likely due to isolated storms, soil moisture anomalies, topography, runoff, or vertical infiltration.

Spatial Error Models Relating $\Delta\overline{\text{GPP}_{i,j,T}}$ to $\Delta\overline{x_{i,j,T}}$ by Simulation

Model Parameters				Z-Normalized Coefficients				Coefficients in Original Units			
LC	**Year**	**R^2**	**Spat.Depend.**	$\Delta\overline{\text{VPD}_{i,j,T}}$	$\Delta\overline{\text{S.M.}_{i,j,T}}$	$\Delta\overline{\text{SW}_{i,j,T}}$	$\Delta\overline{\text{D.Prcp.}_{i,j,T}}$	$\Delta\overline{\text{VPD}_{i,j,T}}$	$\Delta\overline{\text{S.M.}_{i,j,T}}$	$\Delta\overline{\text{SW}_{i,j,T}}$	$\Delta\overline{\text{D.Prcp.}_{i,j,T}}$
001	2017	0.791	$\lambda = 0.876$	-0.153	0.615	0.166	0.148	-0.000064	0.802199	0.000776	0.002492
001	2018	0.779	$\lambda = 0.892$	0.384	0.874	0.107	0.118	0.000225	1.243490	0.000660	0.002404
002	2017	0.791	$\lambda = 0.883$	0.203	0.770	0.126	0.115	0.000119	0.999389	0.000661	0.001873
002	2018	0.807	$\lambda = 0.866$	0.277	0.894	0.094	0.083	0.000218	1.272820	0.000653	0.001639
003	2017	0.765	$\lambda = 0.822$	0.160	0.779	0.110	0.132	0.000106	0.984857	0.000579	0.002176
003	2018	0.796	$\lambda = 0.846$	0.225	0.908	0.106	0.065	0.000199	1.261513	0.000674	0.001178
004	2017	0.788	$\lambda = 0.835$	0.073	0.757	0.151	0.109	0.000036	0.949951	0.000727	0.001872
004	2018	0.786	$\lambda = 0.857$	0.293	0.903	0.118	0.067	0.000198	1.272676	0.000722	0.001301
005	2017	0.778	$\lambda = 0.831$	0.021	0.764	0.160	0.106	0.000010	0.920131	0.000742	0.001723
005	2018	0.777	$\lambda = 0.852$	0.371	0.983	0.098	0.019	0.000253	1.385014	0.000634	0.000355
006	2017	0.744	$\lambda = 0.916$	0.591	0.887	0.094	0.104	0.000374	1.168818	0.000537	0.001803
006	2018	0.779	$\lambda = 0.847$	0.346	0.978	0.102	0.046	0.000289	1.364736	0.000662	0.000844

Table 3.5: Presents the results of spatial error models relating $\Delta\overline{\text{GPP}_{i,j,T}} \sim \Delta\overline{\text{VPD}_{i,j,T}} + \Delta\overline{\text{SoilMoist.}_{i,j,T}} + \Delta\overline{\text{SW RAD.}_{i,j,T}} + \Delta\overline{\text{Daily Prcp.}_{i,j,T}}$ for all simulations. Z-score normalized coefficients showing relative impact and the coefficients in standard units included. The presented models have the lowest AIC and Moran I statistic, and the highest Moran P-value of any model tested for that LC Scenario and Year. All OLS models demonstrated significantly high Moran I statistics. See appendix for full model results (Supplemental Fig. 4.2) and table of standard deviations (Supplemental Fig. 4.1).

Intriguingly, the models suggest the relative influence of the drivers of $\Delta\overline{\text{GPP}_{i,j,T}}$ is more consistent and less variable in the wetter year (2018) than during the drier year (2017) (refer to Fig. 3.20). Spatial extent of deforestation also plays a role, with the observed changes in the relative importance of $\Delta\overline{\text{VPD}_{i,j,T}}$, $\Delta\overline{\text{SoilMoist.}_{i,j,T}}$ and $\Delta\overline{\text{SW RAD.}_{i,j,T}}$ changing the most between years in scenarios 001 and 005. In 2018, $\Delta\overline{\text{VPD}_{i,j,T}}$ coefficients vary between 0.225 and 0.384, $\Delta\overline{\text{SoilMoist.}_{i,j,T}}$ coefficients vary between 0.874 and 0.983, and $\Delta\overline{\text{SW RAD.}_{i,j,T}}$ coefficients vary between 0.094 and 0.118 (Fig. 3.5). In 2017, the influence of these drivers was far more variable, with $\Delta\overline{\text{VPD}_{i,j,T}}$ coefficients varying between -0.153 and 0.591, $\Delta\overline{\text{SoilMoist.}_{i,j,T}}$ coefficients varying between 0.615 and 0.887, and $\Delta\overline{\text{SW RAD.}_{i,j,T}}$ coefficients varying between 0.094 and 0.166. In 2018, the higher quotient of soil moisture and lower

vapor pressure deficit reduced plant stress and potentially increased conductance and photosynthesis (see Fig. 2.4, as reduced soil moisture stress results in higher rates of GPP when RuBisCO is limiting), minimizing variation in the relationship between how changes in $\Delta\overline{\text{SoilMoist.}_{i,j,T}}$ and $\Delta\overline{\text{VPD}_{i,j,T}}$ give rise to changes in $\Delta\overline{\text{GPP}_{i,j,T}}$. The largely consistent association (with the exception of 006) between how standardized differences in soil moisture and VPD impact standardized changes in GPP between LC scenarios and associated controls reflects the formulation of water relations and limitation in Noah-MP, and the shift in climate influence space between 2017 and 2018 indicates that deforestation-driven changes in local meteorology shift the relative influence of the primary drivers of GPP, namely light, and water potentials. For example, in 2017 which is drier than 2018, the relative influence of changes in both soil moisture and VPD on GPP is muted, and the relative influence of light is higher (again, see Fig. 2.4, as warmer temperatures increase the likelihood of light limitation, and drier conditions correspond with warmer temperatures). One explanation is that with less moisture in the environment in general, variation in moisture in the air and in soils has less of an impact on GPP. And, with greater SW RAD in 2017, almost certainly due to reduced convective cloud formation, appears to be relatively more responsive to changes in photosynthetically active radiation, which makes sense if GPP is light-limited.

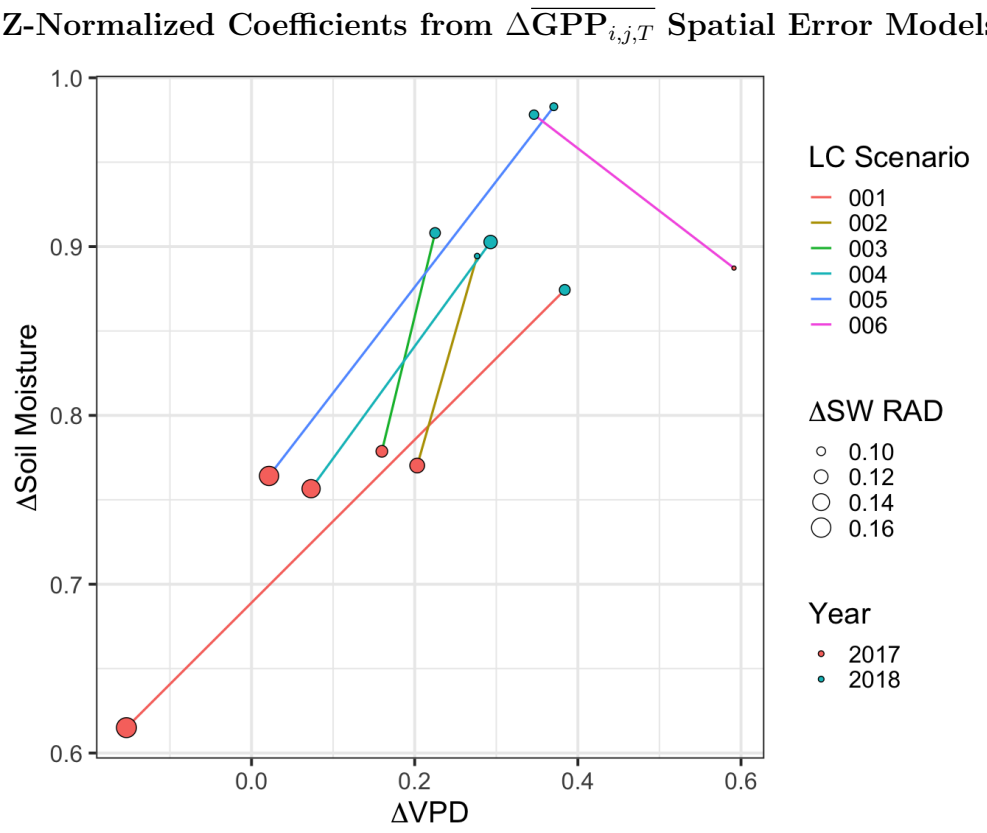

Figure 3.20: Demonstrating the change in coefficients relating $\Delta\overline{\text{GPP}_{i,j,T}}$ to $\Delta\overline{\text{VPD}_{i,j,T}}$, $\Delta\overline{\text{SoilMoist.}_{i,j,T}}$, and $\Delta\overline{\text{SW RAD.}_{i,j,T}}$ in the spatial error models for both "dry" and "wet" years.

It is clear GPP fluctuates throughout the domain in response to changes in environmental conditions induced by the different deforestation scenarios. While $\Delta\overline{\text{GPP}_{i,j,T}}$ did not follow any clear radial trends or trends with distance from the center of the focal domain in relation to the different deforestation scenarios, there are differences in how $\Delta\overline{\text{VPD}_{i,j,T}}$, $\Delta\overline{\text{SoilMoist.}_{i,j,T}}$, $\Delta\overline{\text{SW RAD.}_{i,j,T}}$, and $\Delta\overline{\text{Daily Prcp.}_{i,j,T}}$ influence $\Delta\overline{\text{GPP}_{i,j,T}}$ across "wet" and "dry" years, and across the different deforestation scenarios. The specific response of changes in GPP to changes in environmental characteristics depends on this larger "climate space", with changes in GPP being more closely correlated with changes in VPD and soil moisture in wetter years, and more closely correlated with changes in available shortwave

radiation in drier years. Scaled up to the entire focal domain, however, the total average GPP throughout the entire focal domain and growing season changes very little.

3.4 Characterization of Spatial Variation & Influence of GPP on Changes in LH

Similar to the environmental variables that drive GPP, and to GPP itself, average LH flux differs minimally between years, it's ∼3% higher in the wetter conditions of 2018 than in 2017 (Table 3.6). Also consistent with the changes in GPP, the deforestation scenarios caused average LH to decrease by <1% on average across all remaining deciduous forest pixels. This suggests that, while the deforestation scenarios are still influencing LH in the remaining deciduous forest pixels, changes are extremely minor and likely do little to impact overall atmospheric stability.

Average LH Across Remaining Deciduous Forest Pixels

Year	LC Applied?	LH (Wm^{-2})
2017	No	82.5218
2017	Yes	82.3164
2017	Delta	-0.2054
2018	No	85.2596
2018	Yes	85.0560
2018	Delta	-0.2036

Table 3.6: Average values of LH for each year, control (No) and treatment (Yes), for the deciduous forest pixels that were not removed/deforested. Supplemental Fig. 4.5 contains values for each individual simulation.

Spatially, $\Delta\overline{\text{LH Flux}_{i,j,T}}$ follows a variable pattern, one similar to $\Delta\overline{\text{GPP}_{i,j,T}}$ (Figs. 3.17 & 3.21, and Figs. 3.18 & 3.22). For instance, the 2018 directional plot of $\Delta\overline{\text{LH Flux}_{i,j,T}}$ have similar radial peaks and troughs for simulations 002 and 005 at ≈60° and ≈-60°, respectively. Additionally, similar to both $\Delta\overline{\text{GPP}_{i,j,T}}$ and $\Delta\overline{\text{SoilMoist.}_{i,j,T}}$, as distance from the center of

the focal domain increases, $\Delta\overline{\text{LH Flux}_{i,j,T}}$ does not attenuate towards zero for any of the scenarios, meaning the influence of the deforestation schemes continues far from the cite of deforestation (Fig. 3.23).

Representative Heat Maps of $\Delta\overline{\text{LH}_{i,j,T}}$ Across Remaining Deciduous Forest Pixels

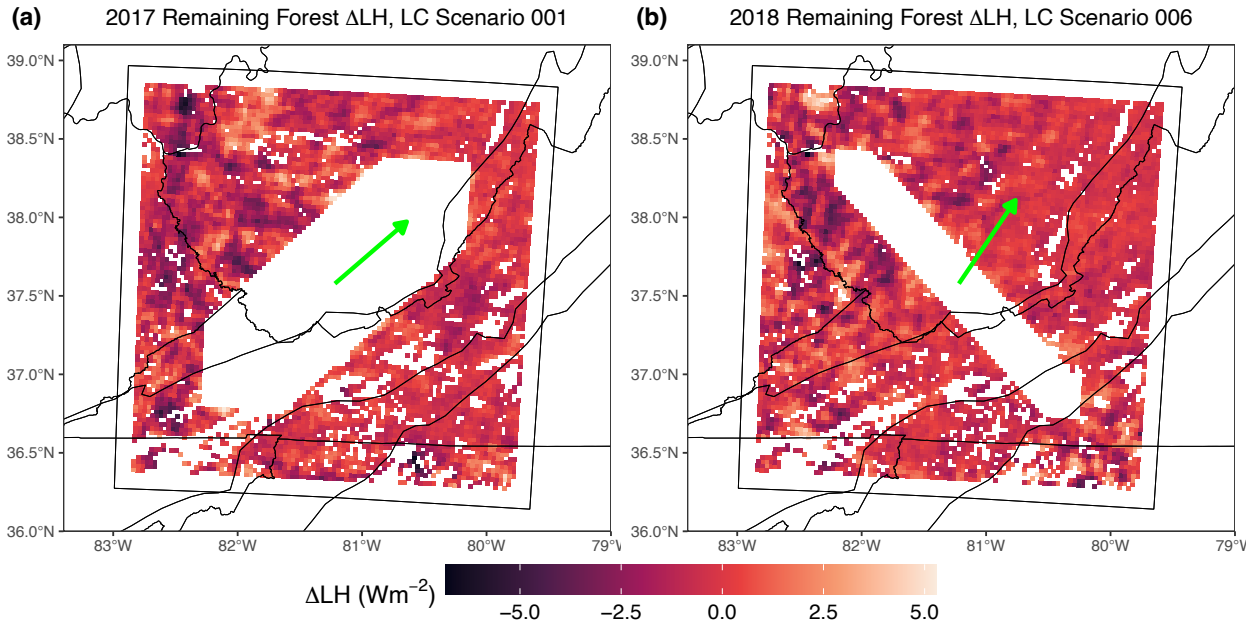

Figure 3.21: Heat maps of the difference between average daily precipitation *before* and *after* deforestation across all remaining deciduous forest pixels ($\Delta\overline{\text{LH}_{i,j,T}}$) for (a) Scenario 001 in 2017 and (b) Scenario 006 in 2018. Green arrows depicts the angle of the average prevailing 10-meter winds inside the deforested pixels, relative to the *east* (2017: 34.348°, 2018: 49.458°). For all heat maps, see Supplemental Figures 4.23 & 4.24.

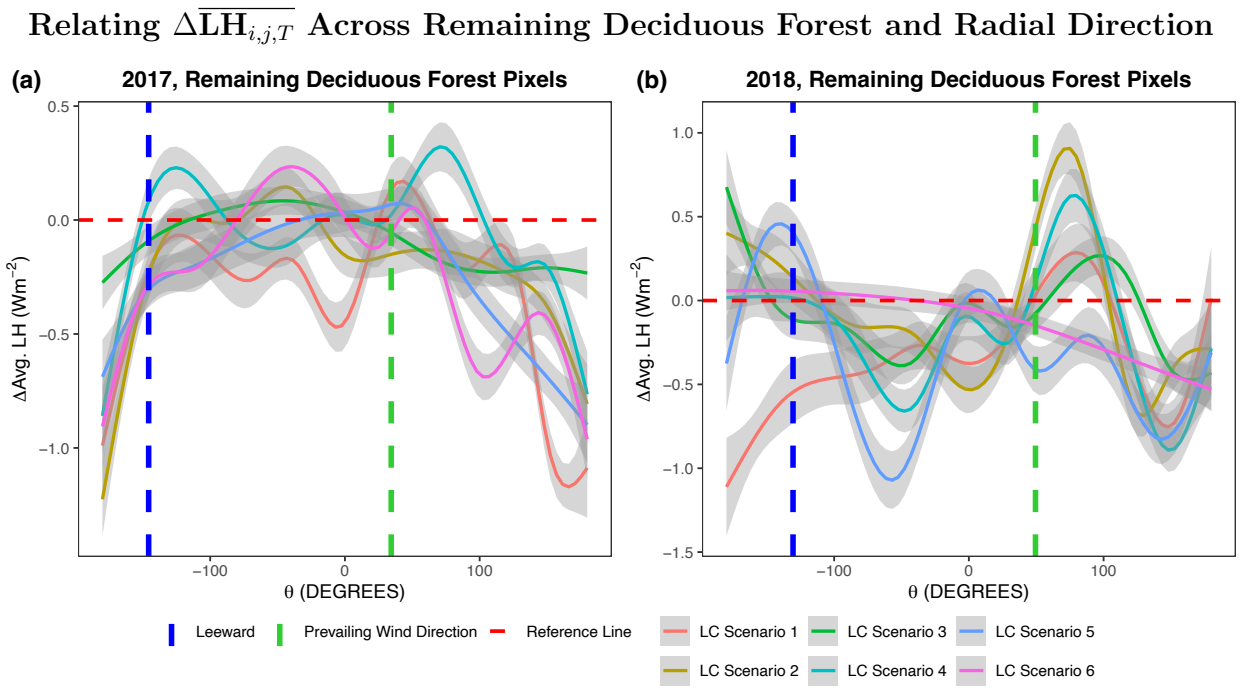

Figure 3.22: A series of GAMs/loess' relating the difference between average LH *before* and *after* deforestation across all remaining deciduous forest pixels ($\Delta\overline{\mathrm{LH}_{i,j,T}}$) and radial direction, relative to the east, where $\theta = 0$. θ **increases** counterclockwise of the east and **decreases** clockwise from the east.

Relating abs($\Delta\overline{\text{LH}_{i,j,T}}$) Across Remaining Deciduous Forest and Distance From Center

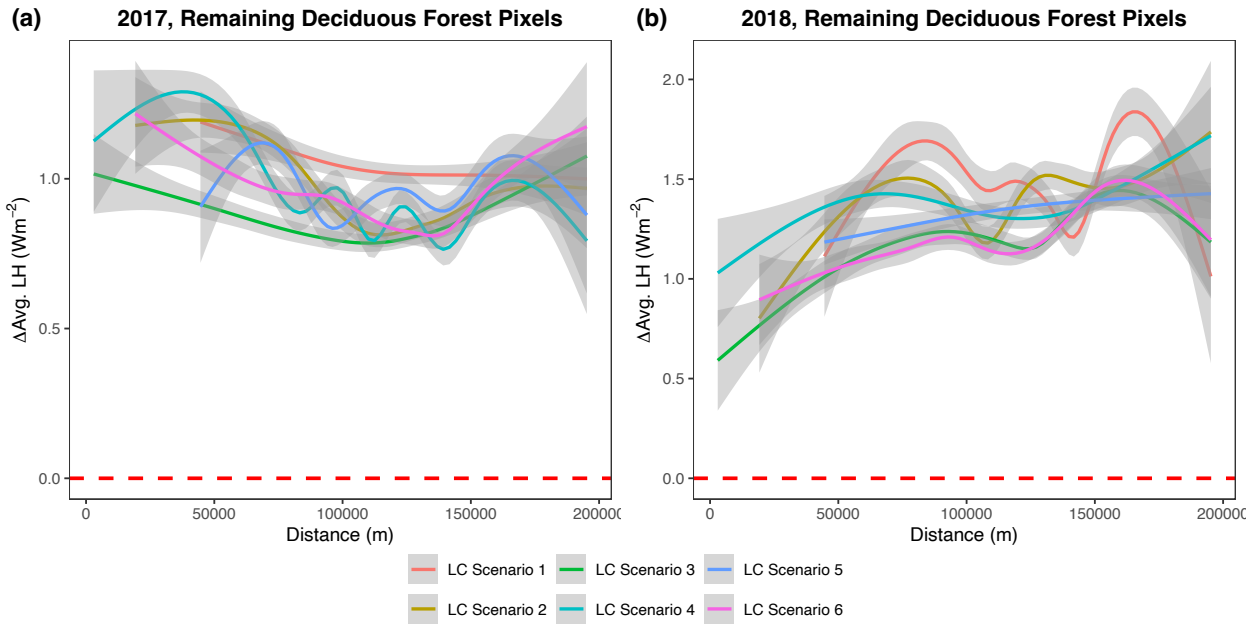

Figure 3.23: A series of GAMs/loess' relating the absolute value of the difference between average LH *before* and *after* deforestation across all remaining deciduous forest pixels (abs($\Delta\overline{\text{LH}_{i,j,T}}$)) and linear distance from the center of the focal domain in meters for both (a) 2017 and (b) 2018 trials.

Across all scenarios, there was a tight correlation between $\Delta\overline{\text{LH Flux}_{i,j,T}}$ and $\Delta\overline{\text{GPP}_{i,j,T}}$, with normalized coefficients ranging between 0.792 and 0.952, and R^2 ranging between 0.766 and 0.883 (Table 3.7). The normalized coefficients relating $\Delta\overline{\text{GPP}_{i,j,T}}$ to $\Delta\overline{\text{LH Flux}_{i,j,T}}$ are higher, though more variable in "dry" 2017 deforestation scenarios, while the relationship is marginally weaker, though more consistent in "wet" 2018 (Fig. 3.24). The largest magnitude change between years was seen for the largest extents of deforestation, scenarios 001 and 005, similar to what was observed for the relationship between $\Delta\overline{\text{GPP}_{i,j,T}}$ and environmental conditions (Figs. 3.5, 3.20). The coupling of $\Delta\overline{\text{LH Flux}_{i,j,T}}$ and $\Delta\overline{\text{GPP}_{i,j,T}}$ depends on the larger climate space, with $\Delta\overline{\text{GPP}_{i,j,T}}$ decreasing in importance with increased precipitation and soil moisture and decreased VPD between 2017 and 2018. Changes in latent heat are more sensitive to changes in GPP under drier conditions compared to wetter conditions, potentially because of greater evaporative demand in the canopy and less soil moisture contributing to evapotranspiration as a whole.

Spatial Error Models of $\Delta\overline{\mathbf{LH}_{i,j,T}}$ by Simulation

LC Scenario	Year	R^2	Spat. Dependence	Z-Norm. GPP	Original Units GPP
001	2017	0.800	$\lambda = 0.886$	0.952	241.537
001	2018	0.857	$\lambda = 0.828$	0.821	208.109
002	2017	0.835	$\lambda = 0.821$	0.884	216.702
002	2018	0.883	$\lambda = 0.804$	0.831	209.106
003	2017	0.829	$\lambda = 0.767$	0.880	217.900
003	2018	0.881	$\lambda = 0.751$	0.859	219.499
004	2017	0.766	$\lambda = 0.845$	0.879	222.240
004	2018	0.840	$\lambda = 0.818$	0.829	208.080
005	2017	0.793	$\lambda = 0.840$	0.856	211.692
005	2018	0.862	$\lambda = 0.817$	0.792	203.986
006	2017	0.844	$\lambda = 0.793$	0.832	198.077
006	2018	0.870	$\lambda = 0.781$	0.827	209.492

Table 3.7: Presents the results of spatial error models relating $\Delta\overline{\mathrm{LH}_{i,j,T}} \sim \Delta\overline{\mathrm{GPP}_{i,j,T}}$ for all simulations. Z-score normalized coefficients showing relative impact and the coefficients in standard units included. The presented models have the lowest AIC and Moran I statistic, and the highest Moran P-value of any model tested (see Supplemental Fig. 4.3, and for standard deviations, see Supplemental Fig. 4.1).

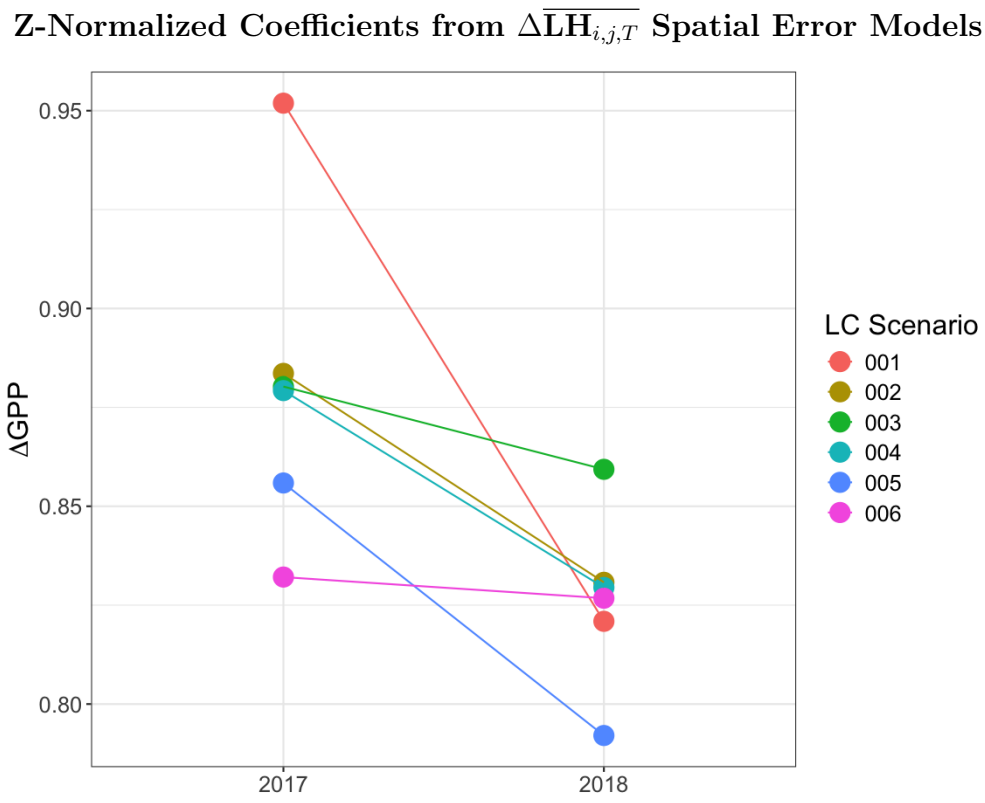

Figure 3.24: Demonstrating the change in coefficients relating $\Delta\overline{\text{LH}_{i,j,T}}$ to $\Delta\overline{\text{GPP}_{i,j,T}}$ in spatial error models between "dry" and "wet" years. The relationship is stronger, though the variation is greater in the drier year than in the wetter year. This suggests that the relative impact of $\Delta\overline{\text{GPP}_{i,j,T}}$ on $\Delta\overline{\text{LH}_{i,j,T}}$ is different across climate space.

Chapter 4

Conclusions, Limitations, and Future Directions

In the first growing season following significant deforestation, average changes to environmental conditions (VPD, soil moisture, available shortwave radiation, and daily precipitation), GPP, and LH are minor, as reported in Tables 3.1, 3.4, & 3.6. However, there is significant pixel-to-pixel and scenario-to-scenario variation in environmental characteristics owing to the wind direction, physiography, and the altered flow of vapor within the lower atmosphere. These environmental conditions, in flux, influence GPP, with changes in soil moisture primarily driving changes in GPP. In drier conditions, however, this relationship becomes less coupled due to the climate space having higher average VPD, light availability, and temperatures, and decreased average soil moisture, making changes in VPD and available SW radiation more relevant (see Figs. 2.4 3.20). Despite the minimal effect of deforestation on GPP averaged across the focal domain and growing season, deforestation does impact the spatial variability in both environmental conditions that influence GPP and GPP, as well as plant-mediated feedbacks to the atmosphere via latent heat flux. The strength of the relationship between changes in GPP and changes in LH also varied depending on climate space, with drier conditions increasing the relative impact of GPP on LH. These results suggests that changes in environmental conditions, as a response to nearby deforestation, depend on the larger environmental context.

Given that changes to environmental conditions in the remaining deciduous forest pixels were minimal on average, these results speak to the resilience of the carbon and hydrologic cycles to significant land cover change in Appalachia. However, these simulations were conducted over only one growing season. Given the feedbacks presented, it is possible that

effects could compound over multiple years and significantly alter nearby deciduous forest carbon and hydrologic cycling. This warrants further investigation into the potential biotic responses to the atmospheric impacts of deforestation and land use change more broadly. Additionally, while these results are ecologically reasonable and the model describes reality with reasonably accurate precision (see Fig. 2.5), there is a significant margin of error that could be reduced as land surface models continue to improve in their ecological realism. More effort is necessary to improve the representation of ecophysiology and the predictability of land surface models, starting with the development of models that contain greater ecological nuance and complexity, despite potential computational constraints (Fisher and Koven [2020]). However, the underlying mechanistic understanding of plant responses to anthropogenic stress across landscapes is not yet well understood (Blumstein [2024]; Anderegg [2023]). Incorporating what is known about the nuanced, context-dependent stress responses of vegetation to unfavorable water potentials in land surface models is critical to improve the forecasting of the influence of anthropogenic disturbance on carbon and water cycling.

Bibliography

Tariq A Al-Ani and JF Bierhuizen. Stomatal resistance, transpiration, and relative water content as influenced by soil moisture stress. *Acta botanica neerlandica*, 20(3): 318–326, 1971. ISSN 0044-5983.

Leander DL Anderegg. Why can't we predict traits from the environment? *New Phytologist*, 237(6):1998–2004, 2023. ISSN 0028-646X.

Roni Avissar and David Werth. Global hydroclimatological teleconnections resulting from tropical deforestation. *Journal of Hydrometeorology*, 6(2):134–145, 2005. ISSN 1525-7541.

Justin E Bagley, Ankur R Desai, Keith J Harding, Peter K Snyder, and Jonathan A Foley. Drought and deforestation: has land cover change influenced recent precipitation extremes in the amazon? *Journal of Climate*, 27(1):345–361, 2014. ISSN 0894-8755.

J Timothy Ball, Ian E Woodrow, and Joseph A Berry. A model predicting stomatal conductance and its contribution to the control of photosynthesis under different environmental conditions. In *Progress in photosynthesis research: volume 4 proceedings of the VIIth international congress on photosynthesis providence, Rhode Island, USA, august 10–15, 1986*, pages 221–224. Springer, 1987.

Roger Bivand, Micah Altman, Luc Anselin, Renato Assunção, Olaf Berke, Andrew Bernat, and Guillaume Blanchet. Package 'spdep'. *Spatial dependence: Weighting schemes, statistics, R package version*, pages 1.1–5, 2017.

Meghan Blumstein. The drivers of intraspecific trait variation and their implications for future tree productivity and survival. *American Journal of Botany*, 111(4):e16312, 2024. ISSN 0002-9122.

IA Boutle, SE Belcher, and RS Plant. Moisture transport in midlatitude cyclones. *Quarterly Journal of the Royal Meteorological Society*, 137(655):360–373, 2011. ISSN 0035-9009.

JA Bunce. Light dependence of carboxylation capacity for c 3 photosynthesis models. *Photosynthetica*, 54:484–490, 2016. ISSN 0300-3604.

U.S. Census Bureau. Cartographic boundary files. `https://www.census.gov/geographies/mapping-files/time-series/geo/carto-boundary-file.html`, 2020. Accessed: 21 Mar 2025.

Patricia R Butler, Louis Iverson, Frank R Thompson, Leslie Brandt, Stephen Handler, Maria Janowiak, P Danielle Shannon, Chris Swanston, Kent Karriker, and Jarel Bartig. Central appalachians forest ecosystem vulnerability assessment and synthesis: a report from the central appalachians climate change response framework project. *Gen. Tech. Rep. NRS-146. Newtown Square, PA: US Department of Agriculture, Forest Service, Northern Research Station. 310 p.*, 146:1–310, 2015.

Yu Cheng and Kaighin A McColl. Thermally direct mesoscale circulations caused by land surface roughness anomalies. *Geophysical Research Letters*, 50(16):e2023GL105150, 2023.

Robert E Dickinson, Muhammad Shaikh, Ross Bryant, and Lisa Graumlich. Interactive canopies for a climate model. *Journal of Climate*, 11(11):2823–2836, 1998. ISSN 1520-0442.

Paul A Dirmeyer and John Shukla. Albedo as a modulator of climate response to tropical deforestation. *Journal of Geophysical Research: Atmospheres*, 99(D10):20863–20877, 1994. ISSN 0148-0227.

MB Ek, KE Mitchell, Ying Lin, Eric Rogers, Pablo Grunmann, Victor Koren, George Gayno, and JD Tarpley. Implementation of noah land surface model advances in the national centers for environmental prediction operational mesoscale eta model. *Journal of Geophysical Research: Atmospheres*, 108(D22), 2003. ISSN 0148-0227.

Graham D Farquhar, S von von Caemmerer, and Joseph A Berry. A biochemical model of photosynthetic co2 assimilation in leaves of c3 species. *planta*, 149(1):78–90, 1980. ISSN 0032-0935.

G Fisch, John Tota, LAT Machado, Maria Assunção Faus da Silva Dias, RF Da F. Lyra, CA Nobre, AJ Dolman, and JHC Gash. The convective boundary layer over pasture and forest in amazonia. *Theoretical and Applied Climatology*, 78:47–59, 2004. ISSN 0177-798X.

Rosie A Fisher and Charles D Koven. Perspectives on the future of land surface models and the challenges of representing complex terrestrial systems. *Journal of Advances in Modeling Earth Systems*, 12(4):e2018MS001453, 2020. ISSN 1942-2466.

Adilson Wagner Gandu, Julia Clarinda Paiva Cohen, and JRS De Souza. Simulation of deforestation in eastern amazonia using a high-resolution model. *Theoretical and Applied Climatology*, 78:123–135, 2004. ISSN 0177-798X.

Yang Gao, Joshua S Fu, JB Drake, Yamg Liu, and Jean-Francois Lamarque. Projected changes of extreme weather events in the eastern united states based on a high resolution climate modeling system. *Environmental Research Letters*, 7(4):044025, 2012. ISSN 1748-9326.

Lydia Dümenil Gates and Stefan Liess. Impacts of deforestation and afforestation in the mediterranean region as simulated by the mpi atmospheric gcm. *Global and Planetary Change*, 30(3-4):309–328, 2001. ISSN 0921-8181.

Ted L Gragson and Paul V Bolstad. Land use legacies and the future of southern appalachia. *Society and Natural Resources*, 19(2):175–190, 2006. ISSN 0894-1920.

Charlotte Grossiord, Thomas N Buckley, Lucas A Cernusak, Kimberly A Novick, Benjamin Poulter, Rolf TW Siegwolf, John S Sperry, and Nate G McDowell. Plant responses to rising vapor pressure deficit. *New phytologist*, 226(6):1550–1566, 2020. ISSN 0028-646X.

PRISM Climate Group. Prism climate data. `https://prism.oregonstate.edu`, 2019. Data last modified: 17 Oct 2019, Accessed: 16 Dec 2020.

C He, P Valayamkunnath, M Barlage, F Chen, D Gochis, R Cabell, T Schneider, R Rasmussen, GY Niu, and ZL Yang. The community noah-mp land surface modeling system technical description version 5.0. Report, NCAR Technical Note NCAR/TN-575+ STR, doi: 10.5065/ew8g-yr95, 2023.

Yufei He, Paolo D'Odorico, and Stephan FJ De Wekker. The role of vegetation–microclimate feedback in promoting shrub encroachment in the northern chihuahuan desert. *Global Change Biology*, 21(6):2141–2154, 2015. ISSN 1354-1013.

Hans Hersbach, Bill Bell, Paul Berrisford, Shoji Hirahara, András Horányi, Joaquín Muñoz-Sabater, Julien Nicolas, Carole Peubey, Raluca Radu, and Dinand Schepers. The era5 global reanalysis. *Quarterly journal of the royal meteorological society*, 146 (730):1999–2049, 2020. ISSN 0035-9009.

Robert J Hijmans, Ed Williams, Chris Vennes, and Maintainer Robert J Hijmans. Package 'geosphere'. *Spherical trigonometry*, 1(7):1–45, 2017.

Song-You Hong and Jeong-Ock Jade Lim. The wrf single-moment 6-class microphysics scheme (wsm6). *Asia-Pacific Journal of Atmospheric Sciences*, 42(2):129–151, 2006. ISSN 1976-7633.

Song-You Hong, Yign Noh, and Jimy Dudhia. A new vertical diffusion package with an explicit treatment of entrainment processes. *Monthly weather review*, 134(9):2318–2341, 2006. ISSN 1520-0493.

Michael J Iacono, Jennifer S Delamere, Eli J Mlawer, Mark W Shephard, Shepard A Clough, and William D Collins. Radiative forcing by long-lived greenhouse gases: Calculations with the aer radiative transfer models. *Journal of Geophysical Research: Atmospheres*, 113(D13), 2008. ISSN 0148-0227.

Pedro A Jiménez, Jimy Dudhia, J Fidel González-Rouco, Jorge Navarro, Juan P Montávez, and Elena García-Bustamante. A revised scheme for the wrf surface layer formulation. *Monthly weather review*, 140(3):898–918, 2012. ISSN 0027-0644.

John S Kain. The kain–fritsch convective parameterization: an update. *Journal of applied meteorology*, 43(1):170–181, 2004. ISSN 1520-0450.

Jianduo Li, Chiyuan Miao, Guo Zhang, Yuan-Hao Fang, Wei Shangguan, and Guo-Yue Niu. Global evaluation of the noah-mp land surface model and suggestions for selecting parameterization schemes. *Journal of Geophysical Research: Atmospheres*, 127(5):e2021JD035753, 2022. ISSN 2169-897X.

Yue Li, Lei Zhou, Shaoqiang Wang, Yonggang Chi, and Jinghua Chen. Leaf temperature and vapour pressure deficit (vpd) driving stomatal conductance and biochemical processes of leaf photosynthetic rate in a subtropical evergreen coniferous plantation. *Sustainability*, 10(11):4063, 2018. ISSN 2071-1050.

Jenny Lindvall and Gunilla Svensson. Wind turning in the atmospheric boundary layer over land. *Quarterly Journal of the Royal Meteorological Society*, 145(724):3074–3088, 2019. ISSN 0035-9009.

Rezaul Mahmood, Roger A Pielke Sr, Kenneth G Hubbard, Dev Niyogi, Paul A Dirmeyer, Clive McAlpine, Andrew M Carleton, Robert Hale, Samuel Gameda, and Adriana Beltrán-Przekurat. Land cover changes and their biogeophysical effects on climate. *International journal of climatology*, 34(4):929–953, 2014. ISSN 0899-8418.

Megan S Mallard and Tanya L Spero. Effects of mosaic land use on dynamically downscaled wrf simulations of the contiguous united states. *Journal of Geophysical Research: Atmospheres*, 124(16):9117–9140, 2019. ISSN 2169-897X.

David Medvigy, Robert L Walko, and Roni Avissar. Effects of deforestation on spatiotemporal distributions of precipitation in south america. *Journal of Climate*, 24(8): 2147–2163, 2011. ISSN 0894-8755.

Guo-Yue Niu and Zong-Liang Yang. Effects of vegetation canopy processes on snow surface energy and mass balances. *Journal of Geophysical Research: Atmospheres*, 109 (D23), 2004. ISSN 0148-0227.

Guo-Yue Niu, Zong-Liang Yang, Kenneth E Mitchell, Fei Chen, Michael B Ek, Michael Barlage, Anil Kumar, Kevin Manning, Dev Niyogi, and Enrique Rosero. The community noah land surface model with multiparameterization options (noah-mp): 1. model description and evaluation with local-scale measurements. *Journal of Geophysical Research: Atmospheres*, 116(D12), 2011. ISSN 0148-0227.

Lucia Perugini, Luca Caporaso, Sergio Marconi, Alessandro Cescatti, Benjamin Quesada, Nathalie de Noblet-Ducoudré, Johanna I House, and Almut Arneth. Biophysical effects on temperature and precipitation due to land cover change. *Environmental Research Letters*, 12(5):053002, 2017. ISSN 1748-9326.

Grant W Petty. *A first course in atmospheric thermodynamics*. Sundog Publishing, 2008. ISBN 1944441018.

Roger A Pielke Sr, Andy Pitman, Dev Niyogi, Rezaul Mahmood, Clive McAlpine, Faisal Hossain, Kees Klein Goldewijk, Udaysankar Nair, Richard Betts, and Souleymane Fall. Land use/land cover changes and climate: modeling analysis and observational evidence. *Wiley Interdisciplinary Reviews: Climate Change*, 2(6):828–850, 2011. ISSN 1757-7780.

William Rodgers, Rezaul Mahmood, Ronald Leeper, and Jun Yan. Land cover change, surface mining, and their impacts on a heavy rain event in the appalachia. *Annals of the American Association of Geographers*, 108(5):1187–1209, 2018. ISSN 2469-4452.

S. Running and M. Zhao. Mod17a2hgf modis/terra gross primary productivity gap-filled 8-day l4 global 500 m sin grid v061. `https://doi.org/10.5067/MODIS/MOD17A2HGF.061`, 2021. Accessed: 2024-09-30.

William H Schlesinger and Scott Jasechko. Transpiration in the global water cycle. *Agricultural and Forest Meteorology*, 189:115–117, 2014. ISSN 0168-1923.

Lindsay Shade, Gabe Schwartzman, Karen Rignall, Kevin Slovinsky, and Jacob Johnson. Afterlives of coal: land and transition dynamics in central appalachia. *Environmental Research: Energy*, 2025. ISSN 2753-3751.

Ken-ichiro Shimazaki, Michio Doi, Sarah M Assmann, and Toshinori Kinoshita. Light regulation of stomatal movement. *Annu. Rev. Plant Biol.*, 58(1):219–247, 2007. ISSN 1543-5008.

William C Skamarock, Joseph B Klemp, Jimy Dudhia, David O Gill, Zhiquan Liu, Judith Berner, Wei Wang, Jordan G Powers, Michael G Duda, and Dale M Barker. A description of the advanced research wrf version 4. *NCAR tech. note ncar/tn-556+ str*, 145, 2019.

Callum Smith, JCA Baker, and DV Spracklen. Tropical deforestation causes large reductions in observed precipitation. *Nature*, 615(7951):270–275, 2023. ISSN 0028-0836.

Ioannis Stergiou, Efthimios Tagaris, and Rafaella-Eleni P Sotiropoulou. Investigating the wrf temperature and precipitation performance sensitivity to spatial resolution over central europe. *Atmosphere*, 12(2):278, 2021. ISSN 2073-4433.

Matthew H Turnbull, David Whitehead, David T Tissue, William S Schuster, Kim J Brown, Victor C Engel, and Kevin L Griffin. Photosynthetic characteristics in canopies of quercus rubra, quercus prinus and acer rubrum differ in response to soil water availability. *Oecologia*, 130:515–524, 2002. ISSN 0029-8549.

Christopher P Weaver and Roni Avissar. Atmospheric disturbances caused by human modification of the landscape. *Bulletin of the American Meteorological Society*, 82(2): 269–282, 2001. ISSN 0003-0007.

Zeng Wei, Jiang Yanling, Li Feng, and Zhou Guangsheng. Responses of photosynthetic parameters of quercus mongolica to soil moisture stresses. *Acta Ecologica Sinica*, 28(6): 2504–2510, 2008. ISSN 1872-2032.

Hadley Wickham, Mara Averick, Jennifer Bryan, Winston Chang, Lucy D'Agostino McGowan, Romain François, Garrett Grolemund, Alex Hayes, Lionel Henry, and Jim Hester. Welcome to the tidyverse. *Journal of open source software*, 4(43):1686, 2019. ISSN 2475-9066.

Ian N Williams and Margaret S Torn. Vegetation controls on surface heat flux partitioning, and land-atmosphere coupling. *Geophysical Research Letters*, 42(21):9416–9424, 2015. ISSN 0094-8276.

Johannes Winckler, Christian H Reick, Ryan M Bright, and Julia Pongratz. Importance of surface roughness for the local biogeophysical effects of deforestation. *Journal of Geophysical Research: Atmospheres*, 124(15):8605–8618, 2019. ISSN 2169-897X.

Susan L Yarnell. *The southern Appalachians: a history of the landscape*, volume 18. Diane Publishing, 1998. ISBN 1428953736.

Lingxue Yu, Ye Liu, Tingxiang Liu, Entao Yu, Kun Bu, Qingyu Jia, Lidu Shen, Xingming Zheng, and Shuwen Zhang. Coupling localized noah-mp-crop model with the wrf model improved dynamic crop growth simulation across northeast china. *Computers and Electronics in Agriculture*, 201:107323, 2022. ISSN 0168-1699.

Kunxiaojia Yuan, Qing Zhu, Shiyu Zheng, Lei Zhao, Min Chen, William J Riley, Xitian Cai, Hongxu Ma, Fa Li, and Huayi Wu. Deforestation reshapes land-surface energy-flux partitioning. *Environmental Research Letters*, 16(2):024014, 2021. ISSN 1748-9326.

Appendix

Standard Deviations of All $\Delta\overline{x_{i,j,T}}$

LC Scenario	Year	GPP ($gCm^{-2}hr^{-1}$)	VPD (Pa)	Soil Moisture (m^3m^{-3})	SW RAD (Wm^{-2})	Daily Prcp. (mm)	LH Flux (Wm^{-2})
001	2017	0.00528	12.649	0.00404	1.126	0.313	1.339
001	2018	0.00796	13.579	0.00560	1.285	0.391	2.017
002	2017	0.00511	8.738	0.00394	0.977	0.314	1.254
002	2018	0.00753	9.543	0.00529	1.089	0.380	1.896
003	2017	0.00462	6.945	0.00365	0.879	0.281	1.143
003	2018	0.00649	7.345	0.00467	1.021	0.358	1.658
004	2017	0.00489	10.024	0.00389	1.015	0.284	1.236
004	2018	0.00732	10.810	0.00519	1.199	0.379	1.835
005	2017	0.00517	11.142	0.00429	1.113	0.318	1.278
005	2018	0.00721	10.556	0.00512	1.115	0.377	1.858
006	2017	0.00528	8.351	0.00401	0.924	0.303	1.257
006	2018	0.00652	7.813	0.00467	1.004	0.357	1.652

Table 4.1: Standard deviations of all $\Delta\overline{x_{i,j,T}}$ for all LC scenarios. Due to the similarity between the SDs across the different LC scenarios, it is reasonable to assume normalized coefficients are appropriate.

All $\Delta\overline{\text{GPP}_{i,j,T}}$ Models

Treatment & Model			Fit & Autocorrelation					Z-Normalized Coefficients			
LC Scenario	**Year**	**Model**	**R^2**	**MoranStat**	**MoranPVal**	**AIC**	**SpatialDependence**	$\Delta\overline{\text{VPD}_{i,j,T}}$	$\Delta\overline{\text{S.M.}_{i,j,T}}$	$\Delta\overline{\text{SW}_{i,j,T}}$	$\Delta\overline{\text{D.Prcp}_{i,j,T}}$
001	2017	OLS	0.791	0.645	0	6773	NA	-0.234	0.702	0.229	0.0841
001	2017	SLM	0.791	0.284	0	3842	$\rho = 0.584$	-0.0622	0.438	0139	0.0342
001	2017	SEM	0.791	0.0293	0.00024	1862	$\lambda = 0.876$	-0.153	0.615	0.166	0.148
001	2018	OLS	0.779	0.563	0	7161	NA	-0.00998	0.848	0.148	0.0460
001	2018	SLM	0.779	0.223	0	4971	$\rho = 0.540$	0.0492	0.530	0.0894	0.0252
001	2018	SEM	0.779	-0.00270	0.617	3055	$\lambda = 0.892$	0.384	0.874	0.107	0.118
002	2017	OLS	0.791	0.523	0	8080	NA	-0.189	0.745	0.193	0.0504
002	2017	SLM	0.791	0.216	0	5539	$\rho = 0.530$	-0.0459	0.494	0.126	0.0161
002	2017	SEM	0.791	-0.0141	0.965	3729	$\lambda = 0.883$	0.203	0.770	0.126	0.115
002	2018	OLS	0.807	0.511	0	7618	NA	-0.0369	0.845	0.152	0.0369
002	2018	SLM	0.807	0.217	0	5399	$\rho = 0.492$	0.0163	0.556	0.0943	0.0196
002	2018	SEM	0.807	0.00248	0.366	3460	$\lambda = 0.866$	0.277	0.894	0.0945	0.0827
003	2017	OLS	0.765	0.510	0	9329	NA	-0.0859	0.763	0.170	0.0765
003	2017	SLM	0.765	0.199	0	7034	$\rho = 0.497$	0.0103	0.541	0.123	0.0388
003	2017	SEM	0.765	-0.0173	0.989	5355	$\lambda = 0.822$	0.160	0.779	0.110	0.132
003	2018	OLS	0.796	0.523	0	8493	NA	-0.0210	0.866	0.172	0.00985
003	2018	SLM	0.796	0.237	0	6175	$\rho = 0.484$	0.0406	0.601	0.117	0.00600
003	2018	SEM	0.796	0.00341	0.317	4073	$\lambda = 0.846$	0.225	0.908	0.106	0.0650
004	2017	OLS	0.788	0.534	0	7827	NA	-0.152	0.736	0.233	0.0959
004	2017	SLM	0.788	0.229	0	5514	$\rho = 0.500$	-0.0338	0.513	0.165	0.0531
004	2017	SEM	0.788	0.00329	0.329	3856	$\lambda = 0.835$	0.0730	0.757	0.151	0.109
004	2018	OLS	0.786	0.524	0	7985	NA	-0.01570	0.873	0.190	0.0184
004	2018	SLM	0.786	0.221	0	5768	$\rho = 0.498$	0.0393	0.578	0.128	0.0171
004	2018	SEM	0.786	-0.00670	0.799	3899	$\lambda = 0.857$	0.293	0.903	0.118	0.0675
005	2017	OLS	0.778	0.563	0	7073	NA	-0.200	0.729	0.226	0.0702
005	2017	SLM	0.778	0.230	0	5148	$\rho = 0.514$	-0.0714	0.478	0.143	0.0328
005	2017	SEM	0.778	-0.0166	0.975	3544	$\lambda = 0.831$	0.0215	0.764	0.160	0.106
005	2018	OLS	0.777	0.528	0	7240	NA	0.0920	0.983	0.157	-0.0634
005	2018	SLM	0.777	0.219	0	5320	$\rho = 0.503$	0.124	0.663	0.0994	-0.0446
005	2018	SEM	0.777	-0.00028	0.505	3673	$\lambda = 0.852$	0.371	0.983	0.0979	0.0186
006	2017	OLS	0.744	0.452	0	9349	NA	-0.0686	0.814	0.173	0.0143
006	2017	SLM	0.744	0.159	0	7117	$\rho = 0.540$	0.0566	0.545	0.118	0.00349
006	2017	SEM	0.744	-0.0235	0.999	5116	$\lambda = 0.916$	0.591	0.887	0.0940	0.104
006	2018	OLS	0.779	0.479	0	8528	NA	0.0401	0.904	0.140	-0.00200
006	2018	SLM	0.779	0.229	0	6783	$\rho = 0.462$	0.0818	0.645	0.0992	-0.00868
006	2018	SEM	0.779	0.0148	0.0261	4808	$\lambda = 0.847$	0.346	0.978	0.102	0.0463

Table 4.2: All $\Delta\overline{\text{GPP}_{i,j,T}} \sim \Delta\overline{\text{VPD}_{i,j,T}} + \Delta\overline{\text{SoilMoist.}_{i,j,T}} + \Delta\overline{\text{SW RAD.}_{i,j,T}} + \Delta\overline{\text{Daily Prcp.}_{i,j,T}}$ models. Spatial error models (SEM) outperformed spatial lag models (SLM) and ordinary least squares (OLS) models.

All $\Delta\overline{\text{LH Flux}_{i,j,T}}$ Models

LC Scenario	Year	Model	R^2	MoranStat	MoranPVal	AIC	SpatialDependence	Z-Norm. $\Delta\overline{\text{GPP}_{i,j,T}}$ Coeff.
001	2017	OLS	0.800	0.711	0	6521	NA	0.895
001	2017	SLM	0.800	0.366	0	4418	$\rho = 0.504$	0.560
001	2017	SEM	0.800	0.0100	0.113	706	$\lambda = 0.886$	0.952
001	2018	OLS	0.857	0.566	0	4804	NA	0.926
001	2018	SLM	0.857	0.323	0	2658	$\rho = 0.465$	0.602
001	2018	SEM	0.857	0.00454	0.287	1151	$\lambda = 0.828$	0.821
002	2017	OLS	0.835	0.578	0	6565	NA	0.914
002	2017	SLM	0.835	0.338	0	4656	$\rho = 0.434$	0.620
002	2017	SEM	0.835	0.0168	0.0143	2166	$\lambda = 0.821$	0.884
002	2018	OLS	0.883	0.494	0	4419	NA	0.940
002	2018	SLM	0.883	0.296	0	2227	$\rho = 0.414$	0.647
002	2018	SEM	0.883	0.00949	0.105	948	$\lambda = 0.804$	0.931
003	2017	OLS	0.829	0.538	0	7170	NA	0.911
003	2017	SLM	0.829	0.306	0	5490	$\rho = 0.386$	0.669
003	2017	SEM	0.829	-0.0108	0.922	3385	$\lambda = 0.767$	0.880
003	2018	OLS	0.881	0.487	0	4797	NA	0.939
003	2018	SLM	0.881	0.281	0	2878	$\rho = 0.369$	0.690
003	2018	SEM	0.881	-0.0182	0.992	1530	$\lambda = 0.751$	0.859
004	2017	OLS	0.766	0.650	0	8415	NA	0.875
004	2017	SLM	0.766	0.329	0	6080	$\rho = 0.508$	0.566
004	2017	SEM	0.766	-0.00443	0.706	3152	$\lambda = 0.845$	0.879
004	2018	OLS	0.840	0.594	0	6199	NA	0.916
004	2018	SLM	0.840	0.323	0	3741	$\rho = 0.465$	0.607
004	2018	SEM	0.840	-0.00848	0.856	1797	$\lambda = 0.818$	0.829
005	2017	OLS	0.793	0.651	0	6703	NA	0.890
005	2017	SLM	0.793	0.319	0	4463	$\rho = 0.508$	0.560
005	2017	SEM	0.793	-0.00942	0.864	2184	$\lambda = 0.840$	0.856
005	2018	OLS	0.862	0.507	0	4644	NA	0.928
005	2018	SLM	0.862	0.285	0	2468	$\rho = 0.445$	0.625
005	2018	SEM	0.862	-0.00020	0.500	1849	$\lambda = 0.817$	0.792
006	2017	OLS	0.844	0.507	0	6188	NA	0.919
006	2017	SLM	0.844	0.301	0	4236	$\rho = 0.414$	0.642
006	2017	SEM	0.844	0.0111	0.0718	2685	$\lambda = 0.793$	0.832
006	2018	OLS	0.870	0.463	0	5109	NA	0.933
006	2018	SLM	0.870	0.284	0	3047	$\rho = 0.401$	0.672
006	2018	SEM	0.870	0.00478	0.260	2021	$\lambda = 0.781$	0.827

Table 4.3: All $\Delta\overline{\text{LH Flux}_{i,j,T}} \sim \Delta\overline{\text{GPP}_{i,j,T}}$ models. Spatial error models (SEM) outperformed spatial lag models (SLM) and ordinary least squares (OLS) models.

Average Environmental Values in Deforested Pixels

LC Applied?	LC Scenario	Year	GPP ($gCm^{-2}hr^{-1}$)	VPD (Pa)	S.Moist. (m^3m^{-3})	SW RAD (Wm^{-2})	Daily Prcp. (mm)
No	001	2017	0.3093	790.8603	261.1872	0.3125	3.9828
Yes	001	2017	0	820.5131	265.2873	0.2826	3.7373
No	001	2018	0.3035	711.1294	255.0177	0.3202	4.7592
Yes	001	2018	0	731.3864	259.8845	0.2954	4.4609
No	002	2017	0.3062	751.7219	260.6451	0.3171	4.0905
Yes	002	2017	0	776.3500	264.8981	0.2886	3.8667
No	002	2018	0.3064	668.1973	254.6533	0.3279	5.1603
Yes	002	2018	0	683.8566	259.7770	0.3020	4.7288
No	003	2017	0.3095	791.5515	261.1434	0.3124	3.926
Yes	003	2017	0	820.4128	263.6972	0.2860	3.8910
No	003	2018	0.3033	711.1532	254.9318	0.3202	4.7509
Yes	003	2018	0	735.4421	258.1700	0.2978	4.5775
No	004	2017	0.3103	788.7940	261.0758	0.3127	4.0293
Yes	004	2017	0	816.3299	263.8209	0.2855	3.8905
No	004	2018	0.3035	710.4188	254.8664	0.3201	4.7738
Yes	004	2018	0	730.7572	258.3751	0.2976	4.6091
No	005	2017	0.3100	863.7647	260.4853	0.2957	4.0215
Yes	005	2017	0	910.4856	264.5762	0.2667	3.7678
No	005	2018	0.2990	788.3080	254.7741	0.3016	4.4614
Yes	005	2018	0	838.3588	259.1169	0.2761	4.1169
No	006	2017	0.3111	857.2750	260.1607	0.2958	4.1450
Yes	006	2017	0	899.1484	263.9748	0.2682	3.9218
No	006	2018	0.2993	783.2882	254.6896	0.3012	4.4812
Yes	006	2018	0	825.3026	258.7991	0.2775	4.2623

Table 4.4: Average environmental values in deforested pixels for all simulations for both control (NO) and treatment (YES) pixels.

Average Environmental Values in Remaining Deciduous Forest Pixels

LC Applied?	LC Scenario	Year	GPP ($gCm^{-2}hr^{-1}$)	VPD (Pa)	S.Moist. (m^3m^{-3})	SW RAD (Wm^{-2})	Daily Prcp. (mm)	LH Flux (Wm^{-2})
NO	001	2017	0.2956	886.4643	0.2815	260.0087	3.5456	82.0726
YES	001	2017	0.2950	8828609	0.2805	260.1186	3.5301	81.7043
NO	001	2018	0.2838	804.0163	0.2879	253.7597	3.7928	84.6715
YES	001	2018	0.2832	799.1482	0.2873	253.7526	3.7544	84.2931
NO	002	2017	0.2977	877.2363	0.2858	260.2553	3.5967	82.8740
YES	002	2017	0.2972	875.2922	0.2851	260.2663	3.5782	82.6553
NO	002	2018	0.2865	795.3239	0.2920	254.0098	3.8896	85.4776
YES	002	2018	0.2864	791.9678	0.2917	253.9876	3.8714	85.3694
NO	003	2017	0.2983	867.2288	0.2879	260.2308	3.6363	82.9681
YES	003	2017	0.2978	868.2134	0.2872	260.2881	3.6177	82.8798
NO	003	2018	0.2879	784.6936	0.2947	254.0271	3.9944	85.7278
YES	003	2018	0.2874	784.7604	0.2940	254.1626	3.9684	85.6261
NO	004	2017	0.2970	875.4701	0.2853	260.1575	3.5915	82.5936
YES	004	2017	0.2967	874.2965	0.2846	260.3283	3.5714	82.5128
NO	004	2018	0.2863	792.3224	0.2921	253.9475	3.9131	85.3227
YES	004	2018	0.2853	791.2310	0.2910	254.1682	3.8518	85.0730
NO	005	2017	0.2958	860.7525	0.2875	260.2528	3.5362	81.9515
YES	005	2017	0.2952	859.5164	0.2867	260.3975	3.5425	81.7184
NO	005	2018	0.2855	776.5907	0.2946	253.8523	3.9011	84.8094
YES	005	2018	0.2848	775.2252	0.2940	254.1328	3.8994	84.5500
NO	006	2017	0.2972	862.2022	0.2888	260.3261	3.5924	82.6709
YES	006	2017	0.2964	862.2712	0.2880	260.3687	3.5202	82.4277
NO	006	2018	0.2875	779.1536	0.2957	254.0071	3.9864	85.5487
YES	006	2018	0.2871	778.6013	0.2955	254.0935	3.9825	85.4243

Table 4.5: Average environmental conditions across all simulations for both control (NO) and treatment (YES) pixels.

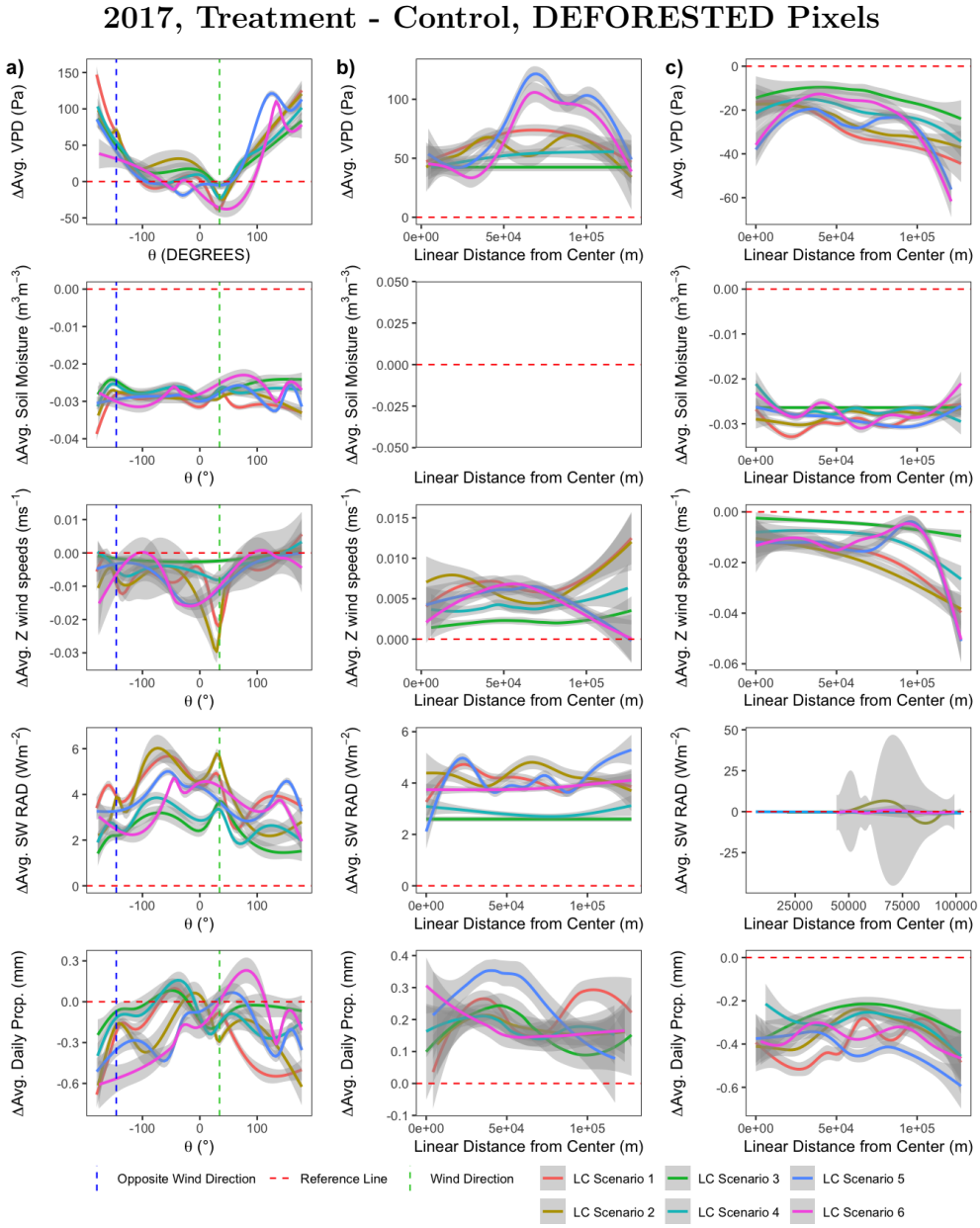

Figure 4.1: 2017 simulations, ONLY deforested pixels. A series of GAMs/loess' characterizing how the difference between control and treatment ($\Delta\overline{x_{i,j,T}}$) of a given environmental variable varies with space relative to the center of the focal domain. Created using 'geom_smooth' in Tidyverse (Wickham et al. [2019]). (col. a) The average value of $\Delta\overline{x_{i,j,T}}$ for a given radial direction, relative to the $+x$-axis. (b) The average of POSITIVE $\Delta\overline{x_{i,j,T}}$ values with radial distance r. (c) The average of NEGATIVE $\Delta\overline{x_{i,j,T}}$ values with radial distance r.

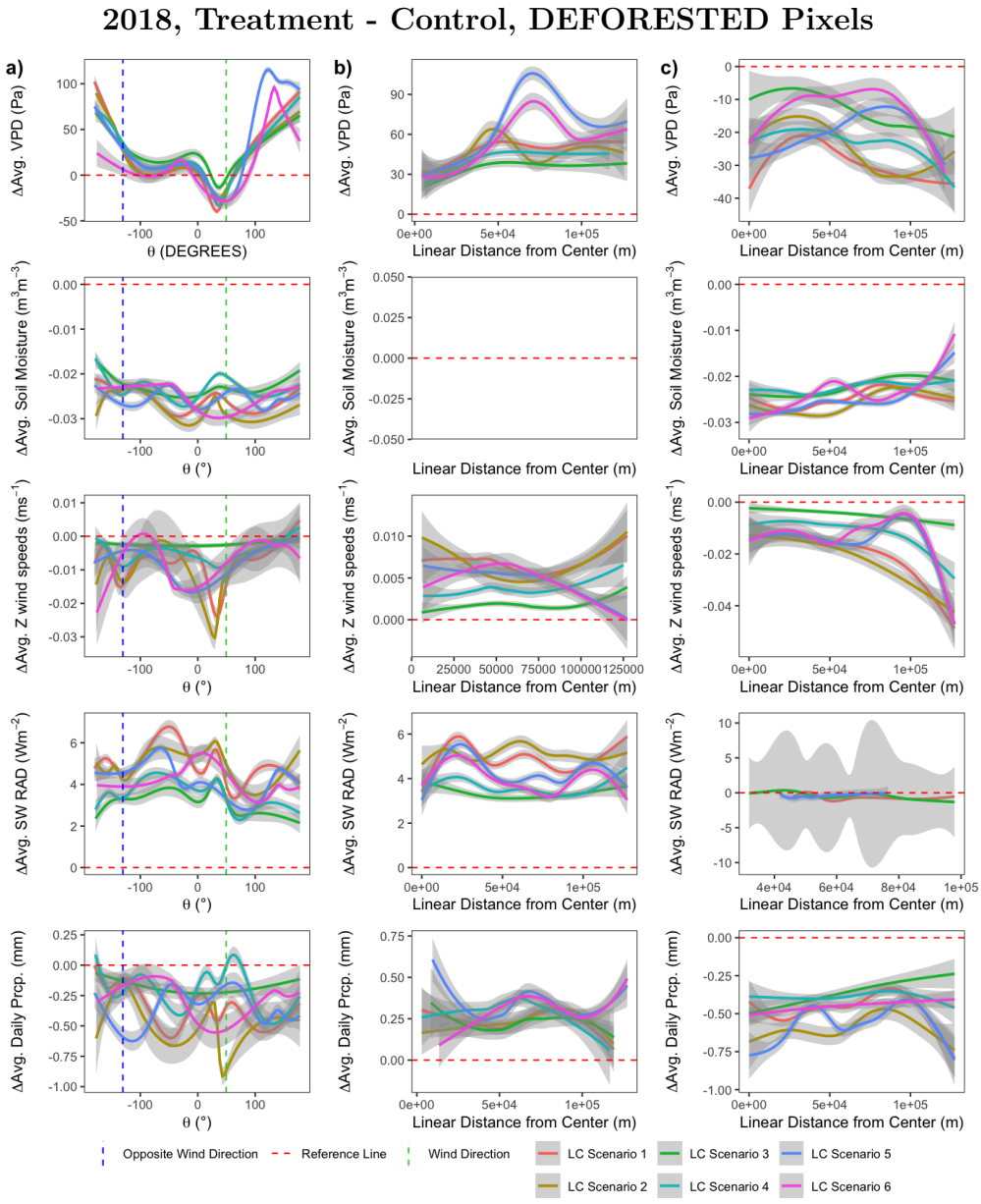

Figure 4.2: 2018 simulations, ONLY deforested pixels. A series of GAMs/loess' characterizing how the difference between control and treatment ($\Delta\overline{x_{i,j,T}}$) of a given environmental variable varies with space relative to the center of the focal domain. Created using 'geom_smooth' in Tidyverse (Wickham et al. [2019]). (col. a) The average value of $\Delta\overline{x_{i,j,T}}$ for a given radial direction, relative to the $+x$-axis. (b) The average of POSITIVE $\Delta\overline{x_{i,j,T}}$ values with radial distance r. (c) The average of NEGATIVE $\Delta\overline{x_{i,j,T}}$ values with radial distance r.

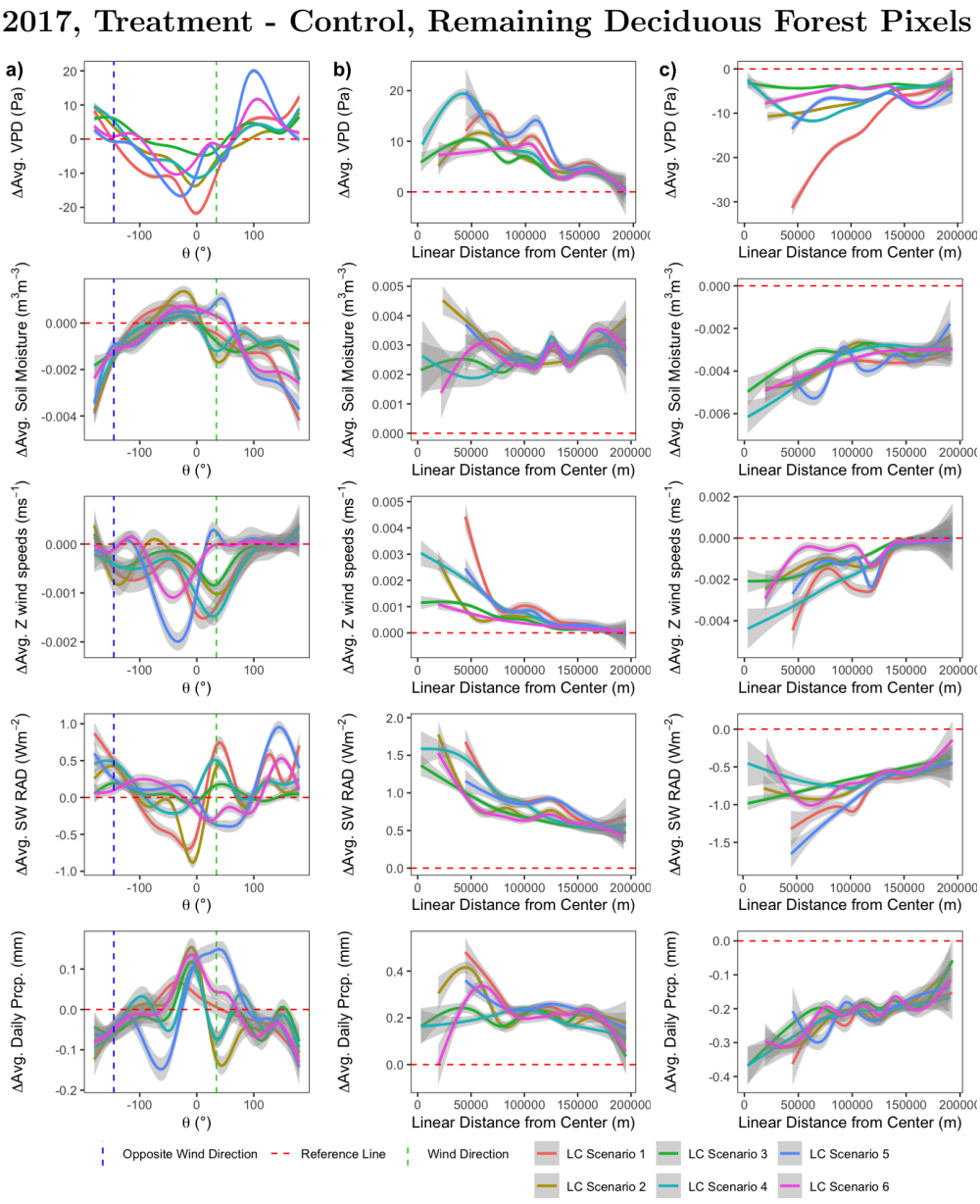

Figure 4.3: 2017 simulations, ONLY remaining deciduous forest pixels. A series of GAMs/loess' characterizing how the difference between control and treatment ($\Delta\overline{x_{i,j,T}}$) of a given environmental variable varies with space relative to the center of the focal domain. Created using 'geom_smooth' in Tidyverse (Wickham et al. [2019]). (col. a) The average value of $\Delta\overline{x_{i,j,T}}$ for a given radial direction, relative to the $+x$-axis. (b) The average of POSITIVE $\Delta\overline{x_{i,j,T}}$ values with radial distance r. (c) The average of NEGATIVE $\Delta\overline{x_{i,j,T}}$ values with radial distance r.

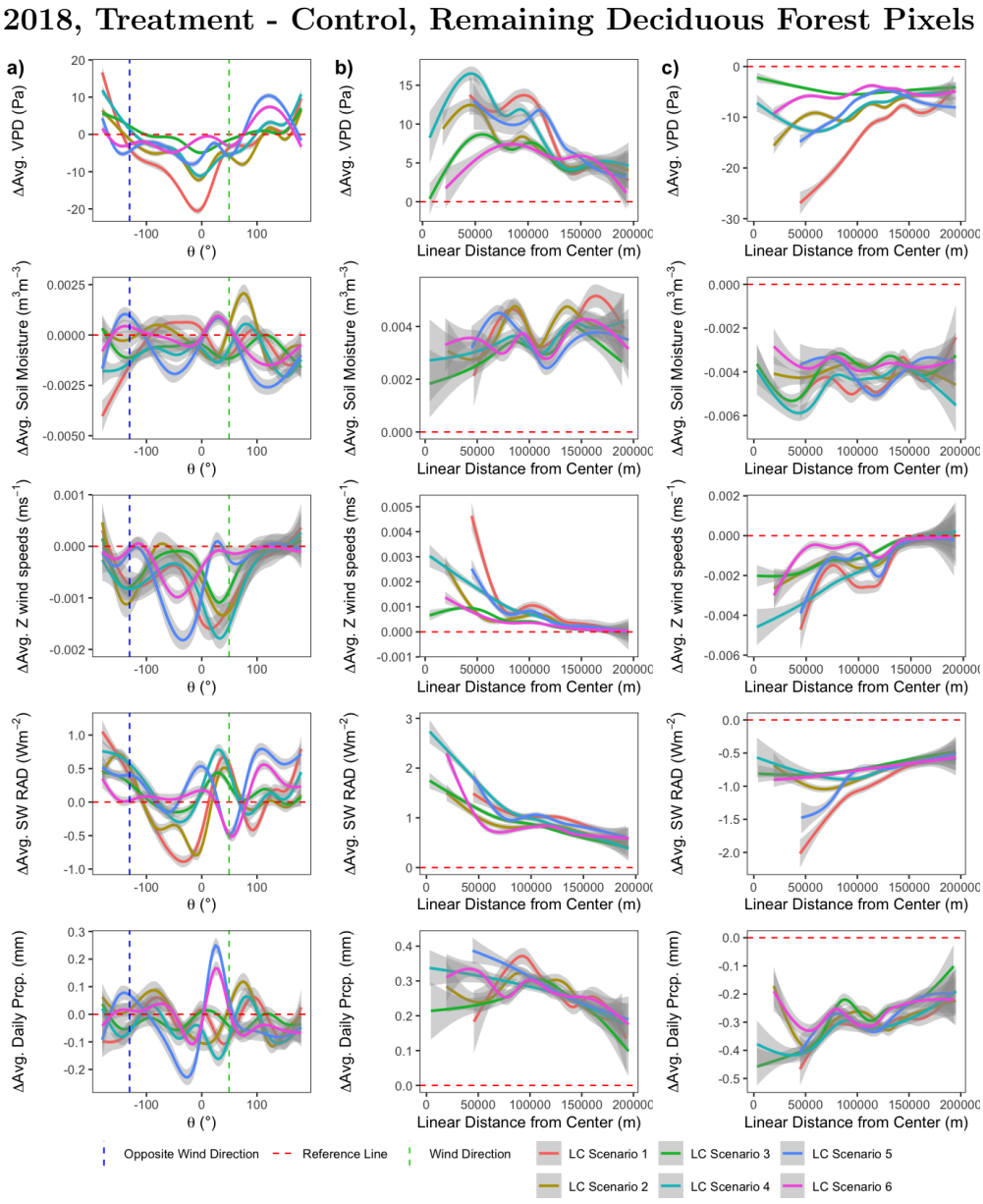

Figure 4.4: 2018 simulations, ONLY remaining deciduous forest pixels. A series of GAMs/loess' characterizing how the difference between control and treatment ($\Delta\overline{x_{i,j,T}}$) of a given environmental variable varies with space relative to the center of the focal domain. Created using 'geom_smooth' in Tidyverse (Wickham et al. [2019]). (col. a) The average value of $\Delta\overline{x_{i,j,T}}$ for a given radial direction, relative to the $+x$-axis. (b) The average of POSITIVE $\Delta\overline{x_{i,j,T}}$ values with radial distance r. (c) The average of NEGATIVE $\Delta\overline{x_{i,j,T}}$ values with radial distance r.

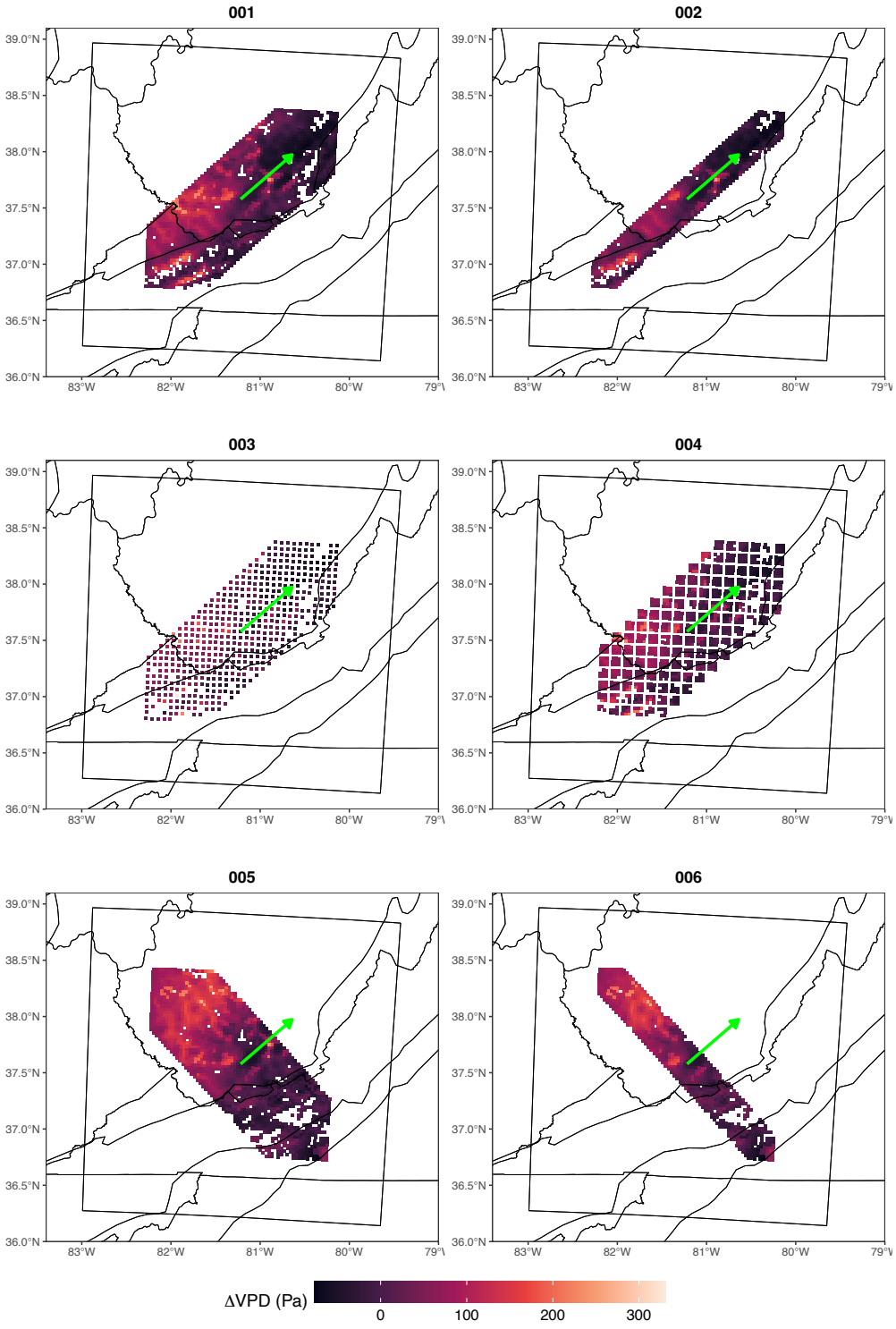

Figure 4.5: Heat maps of $\Delta\overline{\text{VPD}_{i,j,T}}$ across the deforested pixels of all LC Scenarios in 2017.

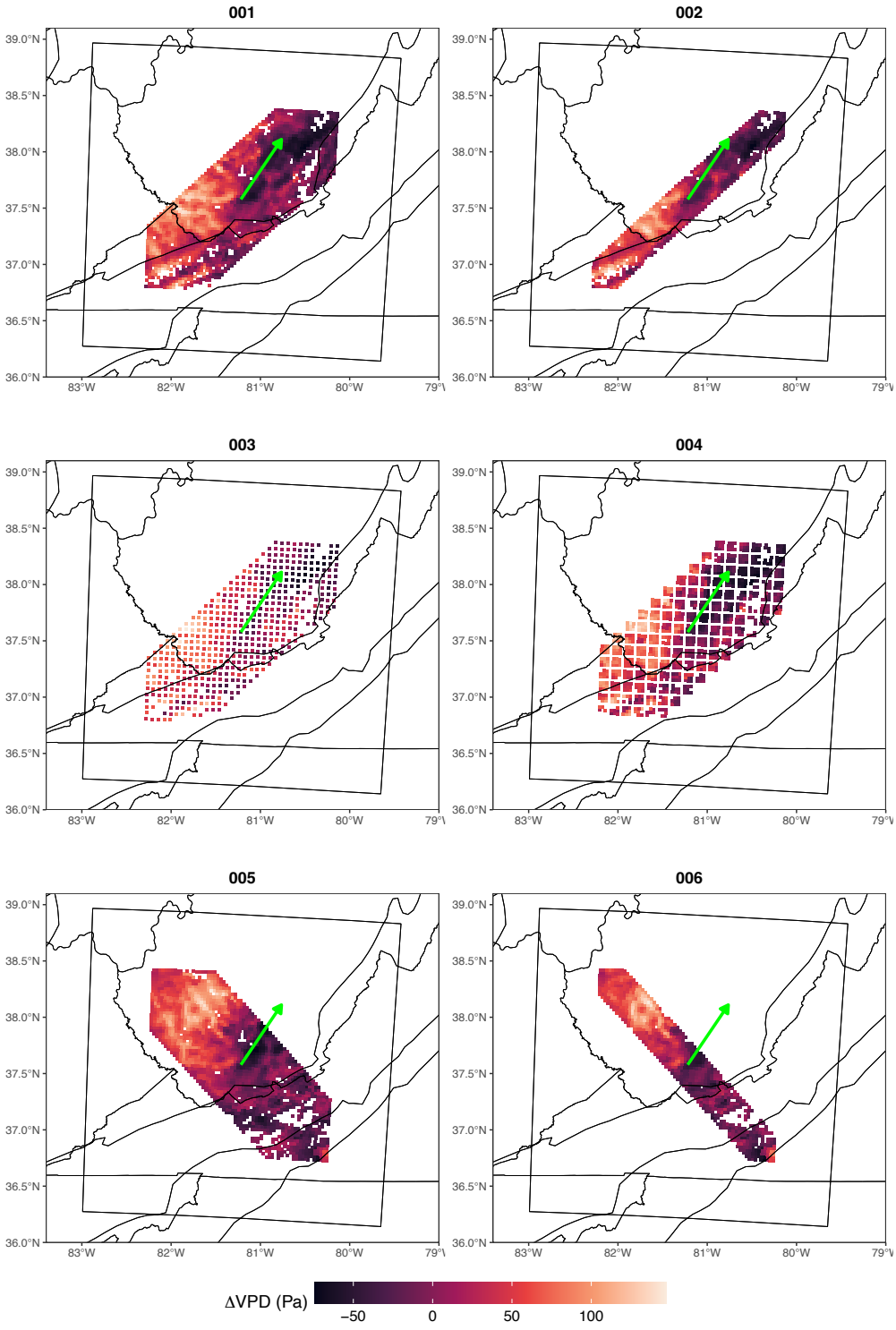

Figure 4.6: Heat maps of $\Delta\overline{\mathrm{VPD}_{i,j,T}}$ across the deforested pixels of all LC Scenarios in 2018.

2017, $\Delta\overline{\text{VPD}_{i,j,T}}$, Remaining Deciduous Forest Pixels

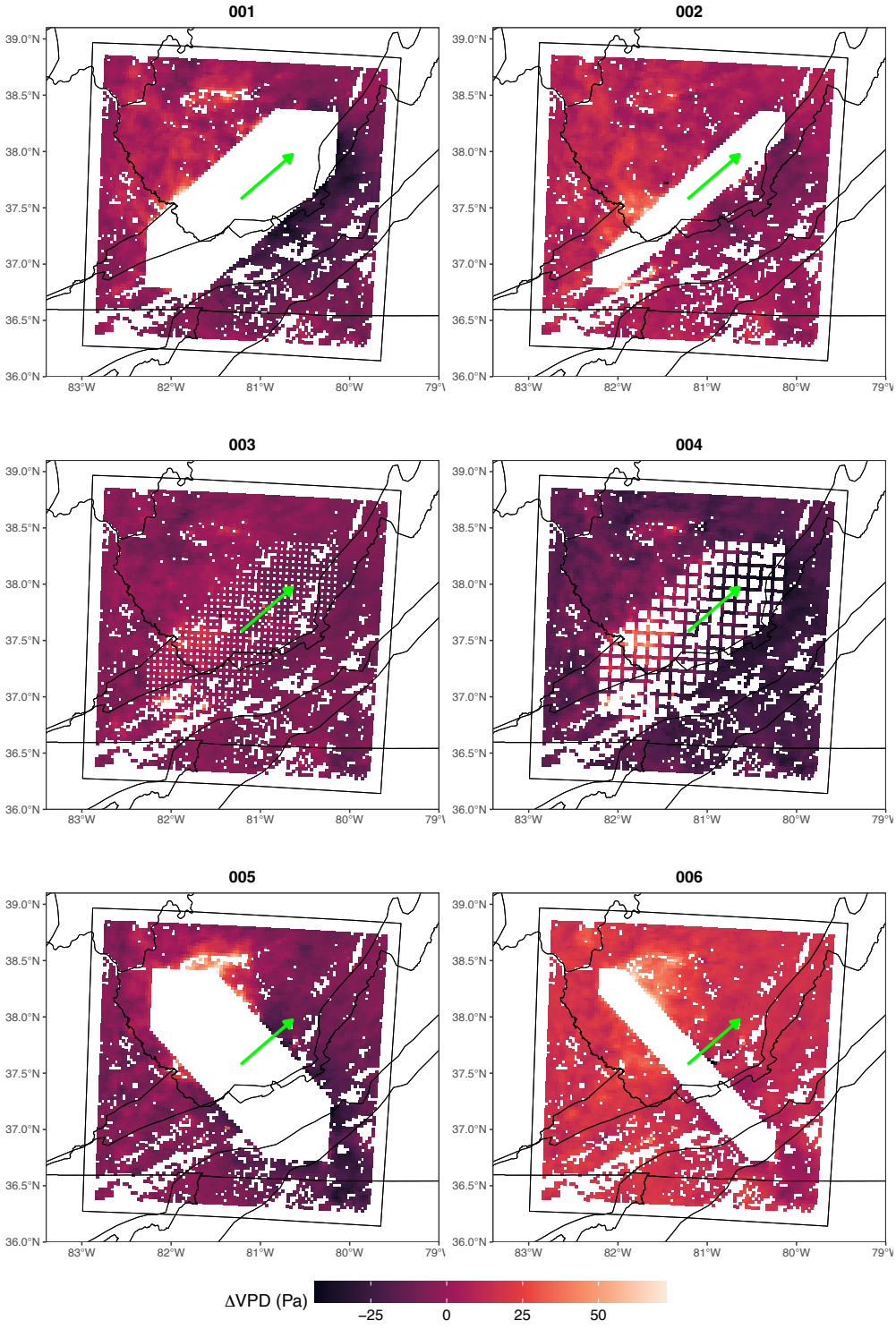

Figure 4.7: Heat maps of $\Delta\overline{\text{VPD}_{i,j,T}}$ across the remaining deciduous forest pixels of all LC Scenarios in 2017.

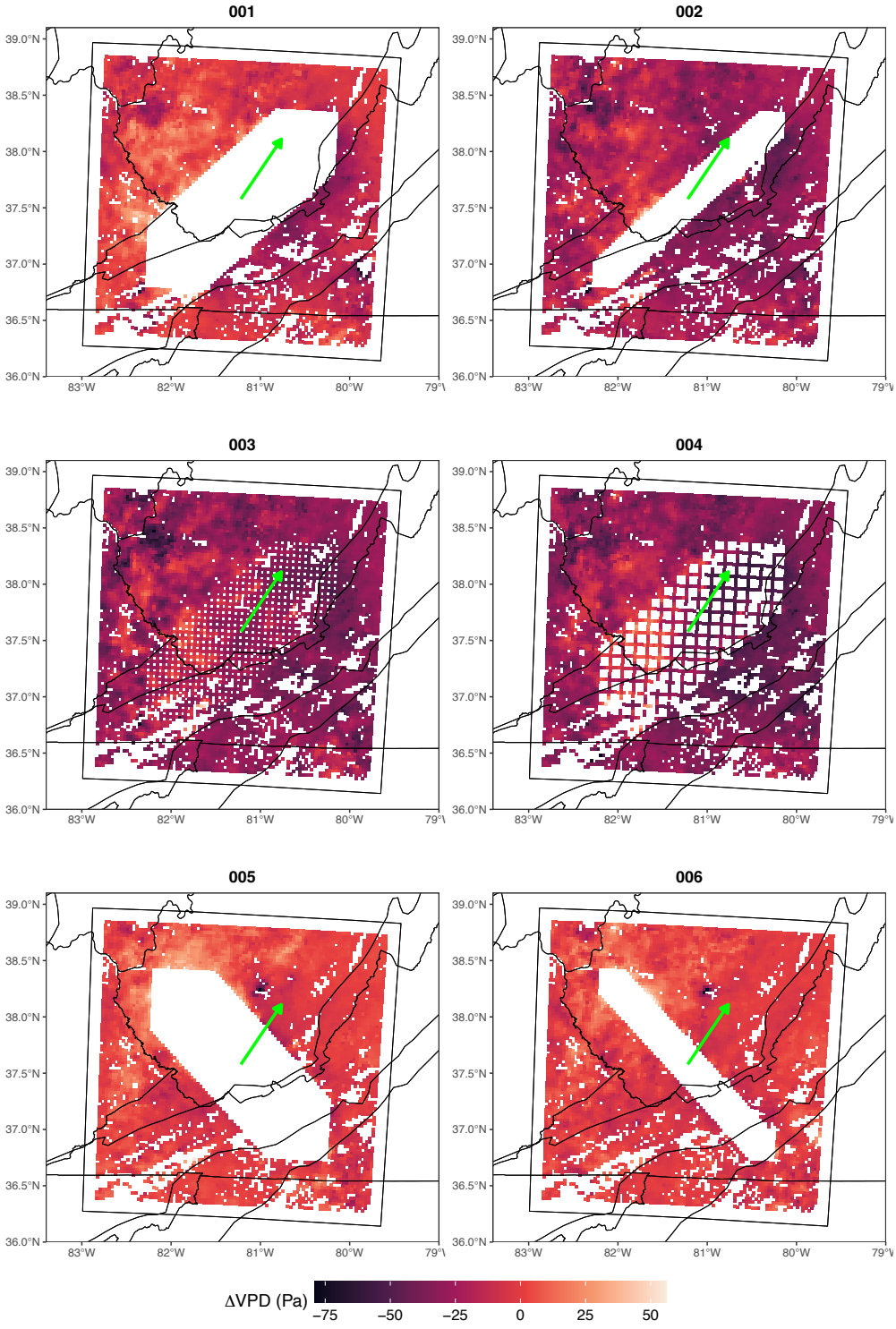

Figure 4.8: Heat maps of $\Delta\overline{\text{VPD}_{i,j,T}}$ across the remaining deciduous forest pixels of all LC Scenarios in 2018.

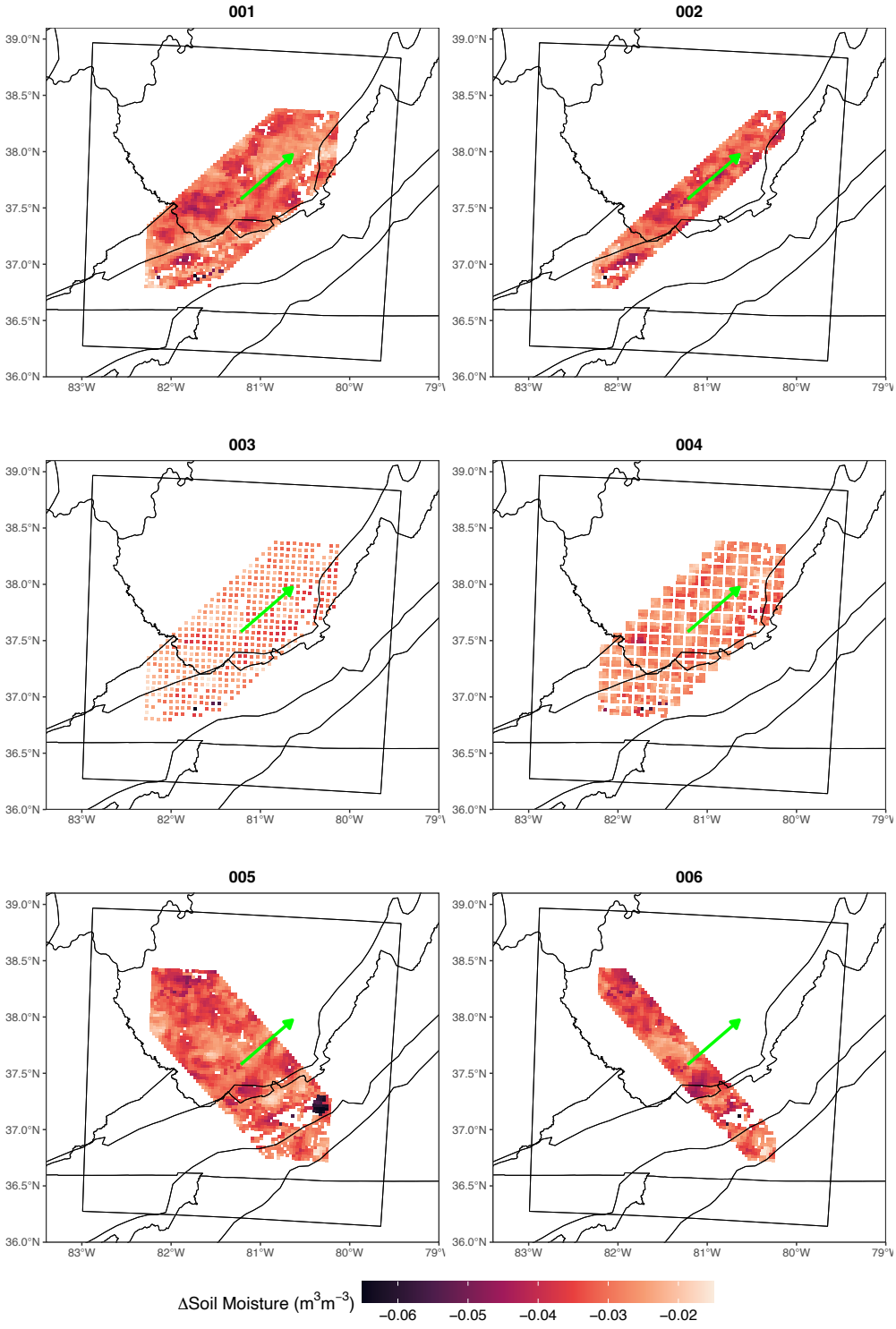

Figure 4.9: Heat maps of $\Delta\overline{\text{SoilMoist.}}_{i,j,T}$ across the deforested pixels of all LC Scenarios in 2017.

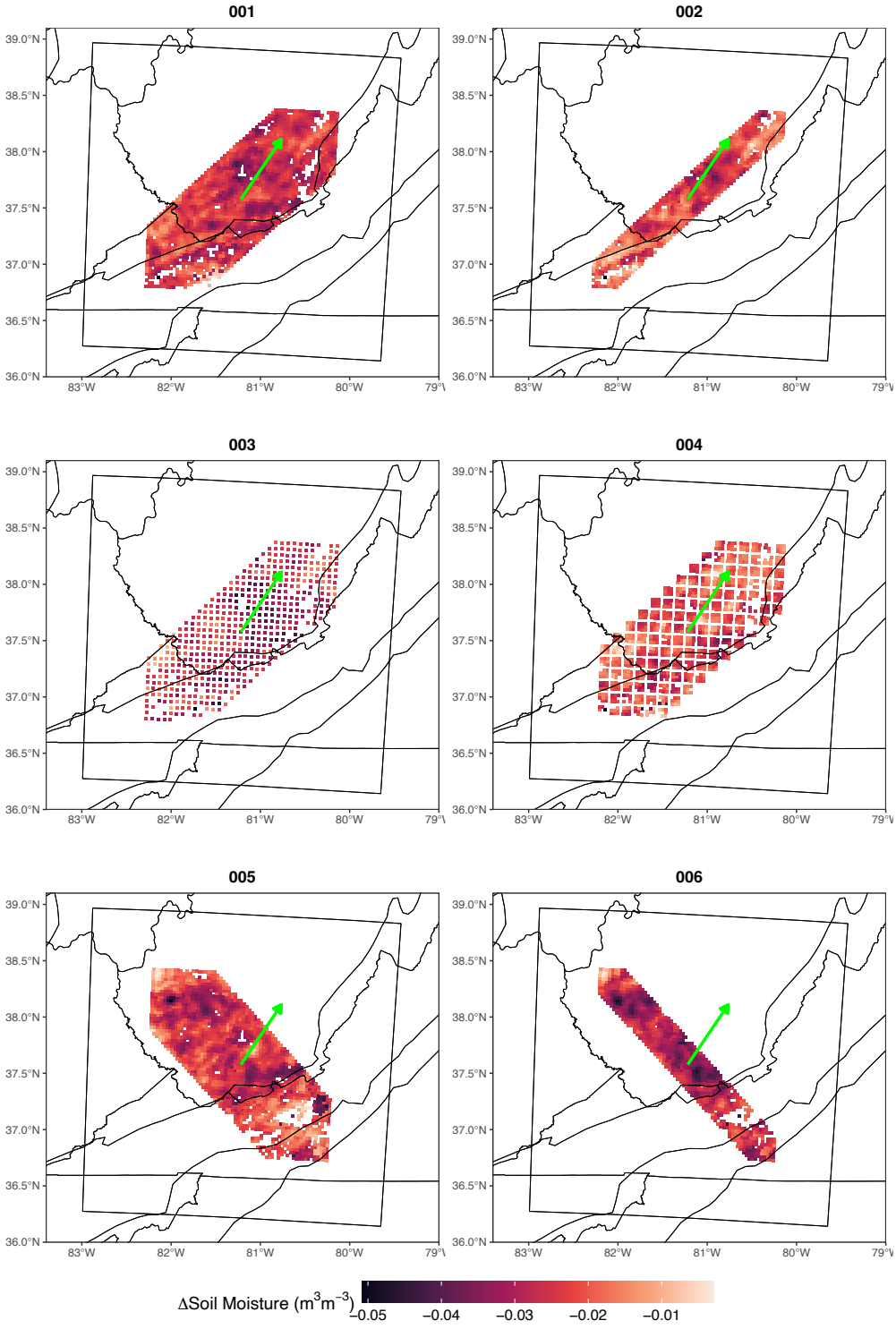

Figure 4.10: Heat maps of $\Delta\overline{\text{SoilMoist.}}_{i,j,T}$ across the deforested pixels of all LC Scenarios in 2018.

2017, $\Delta\overline{\text{Soil Moist.}}_{i,j,T}$, Remaining Deciduous Forest Pixels

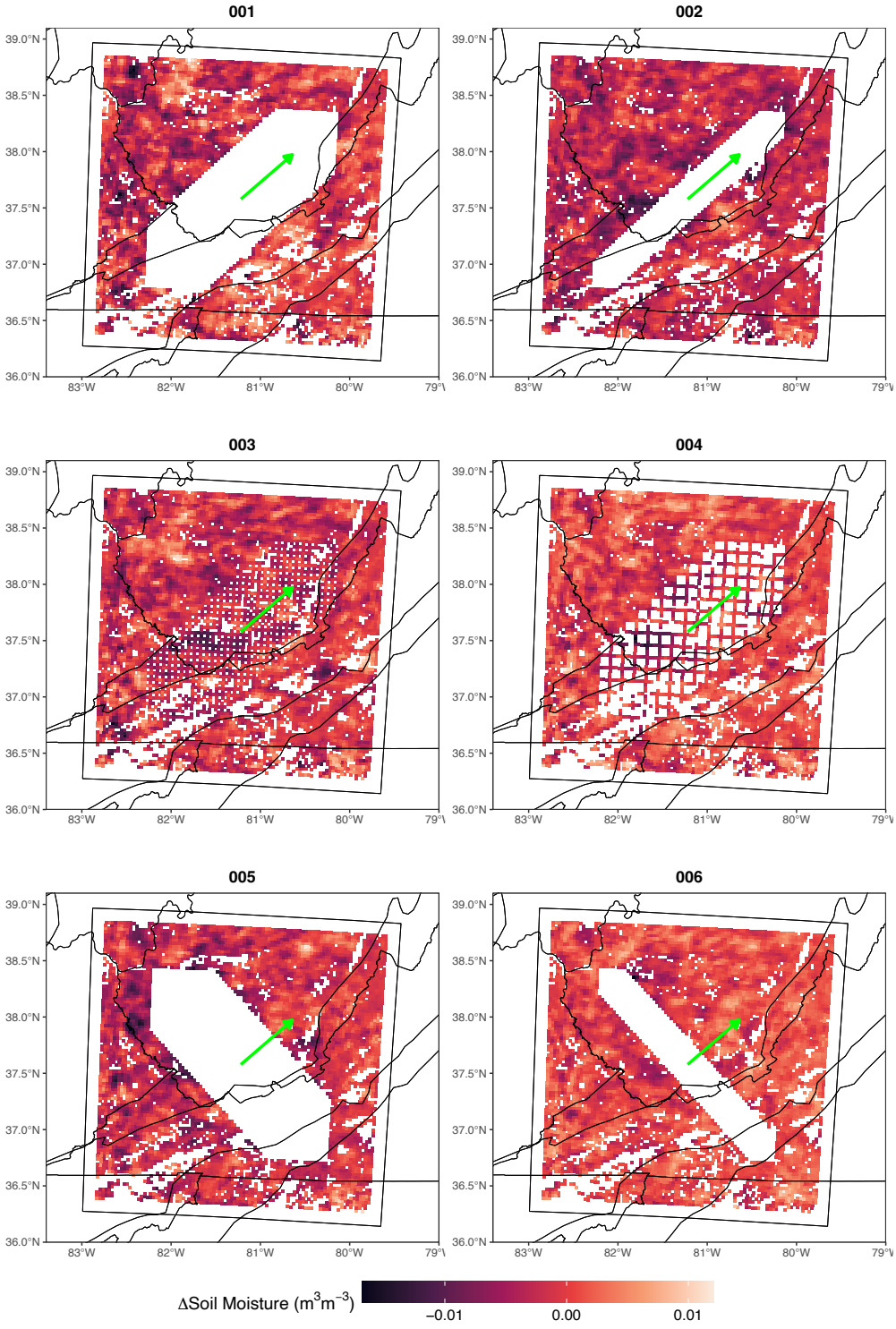

Figure 4.11: Heat maps of $\Delta\overline{\text{SoilMoist.}}_{i,j,T}$ across the remaining deciduous forest pixels of all LC Scenarios in 2017.

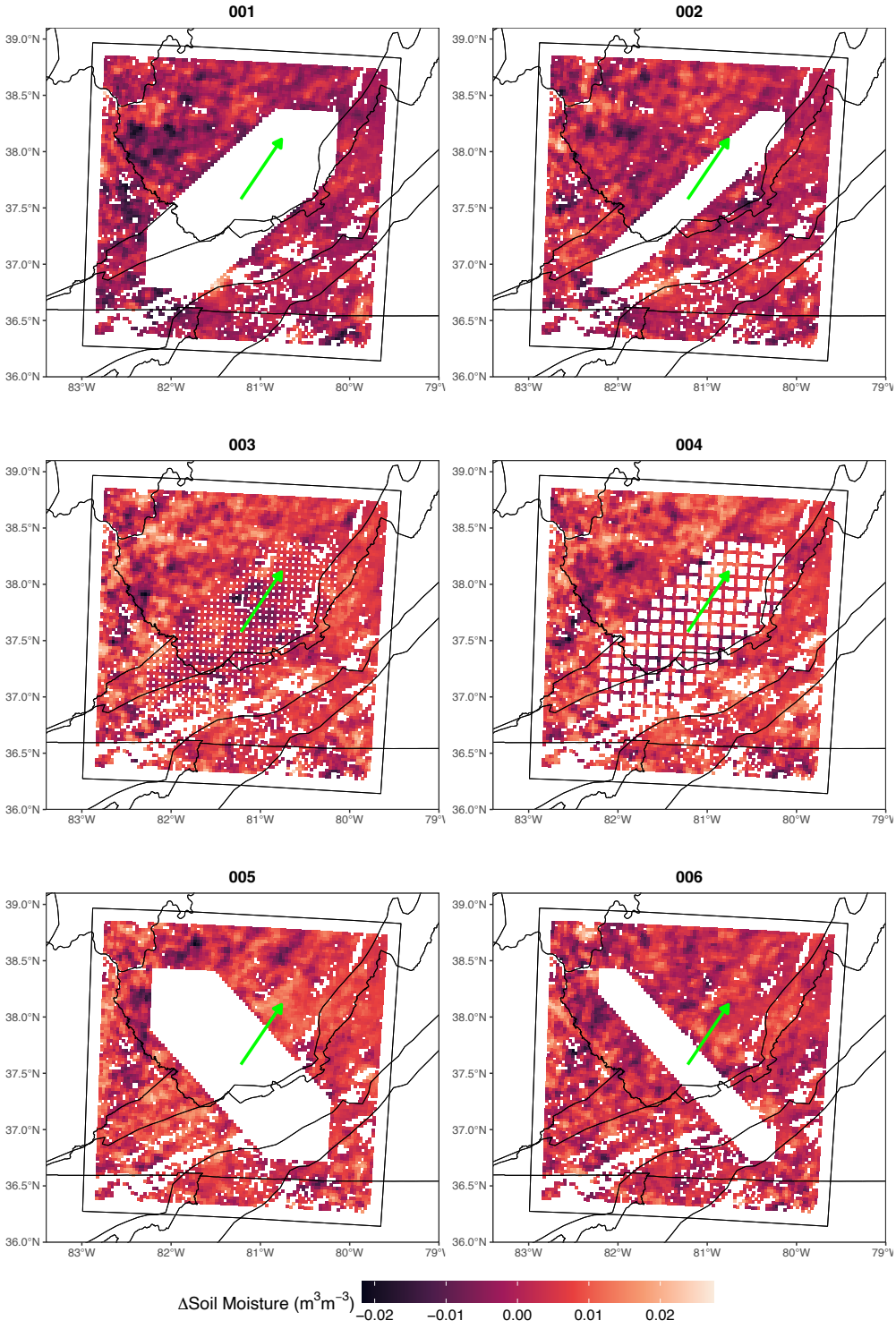

Figure 4.12: Heat maps of $\Delta\overline{\text{SoilMoist}}_{i,j,T}$ across the remaining deciduous forest pixels of all LC Scenarios in 2018.

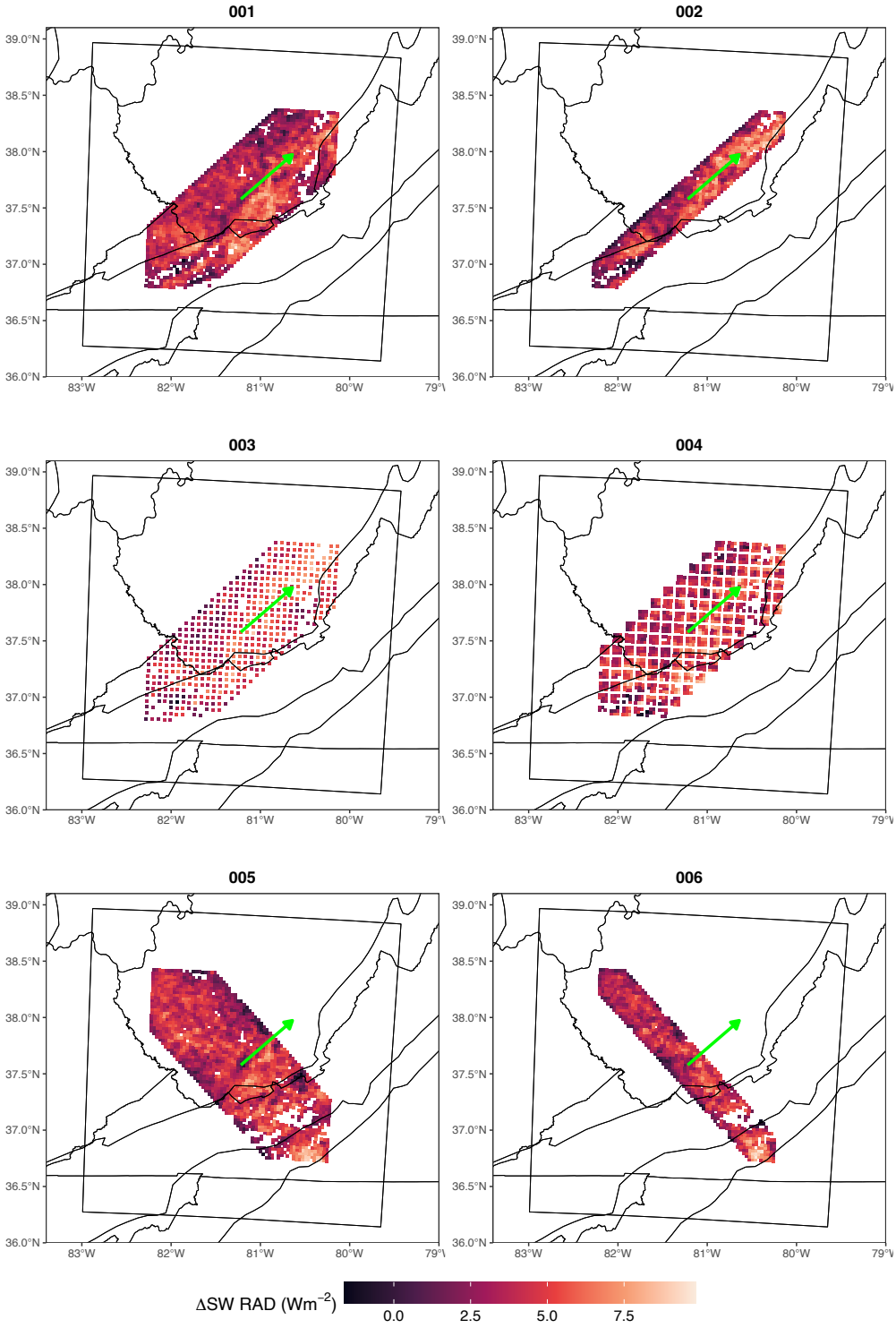

Figure 4.13: Heat maps of $\Delta\overline{\text{SW RAD.}}_{i,j,T}$ across the deforested pixels of all LC Scenarios in 2017.

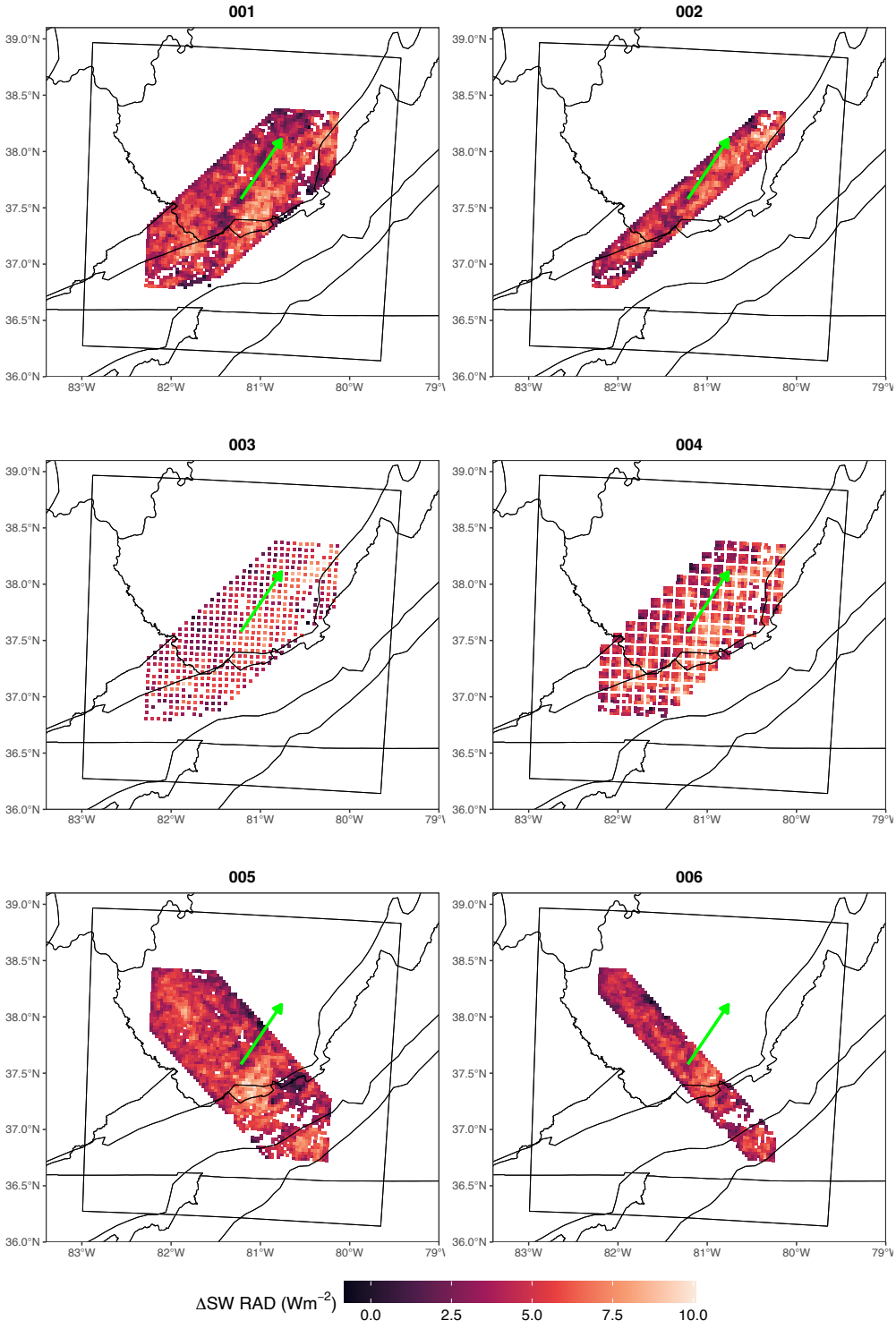

Figure 4.14: Heat maps of $\Delta\overline{\text{SW RAD.}_{i,j,T}}$ across the deforested pixels of all LC Scenarios in 2018.

2017, $\Delta\overline{\text{SW RAD.}}_{i,j,T}$, Remaining Deciduous Forest Pixels

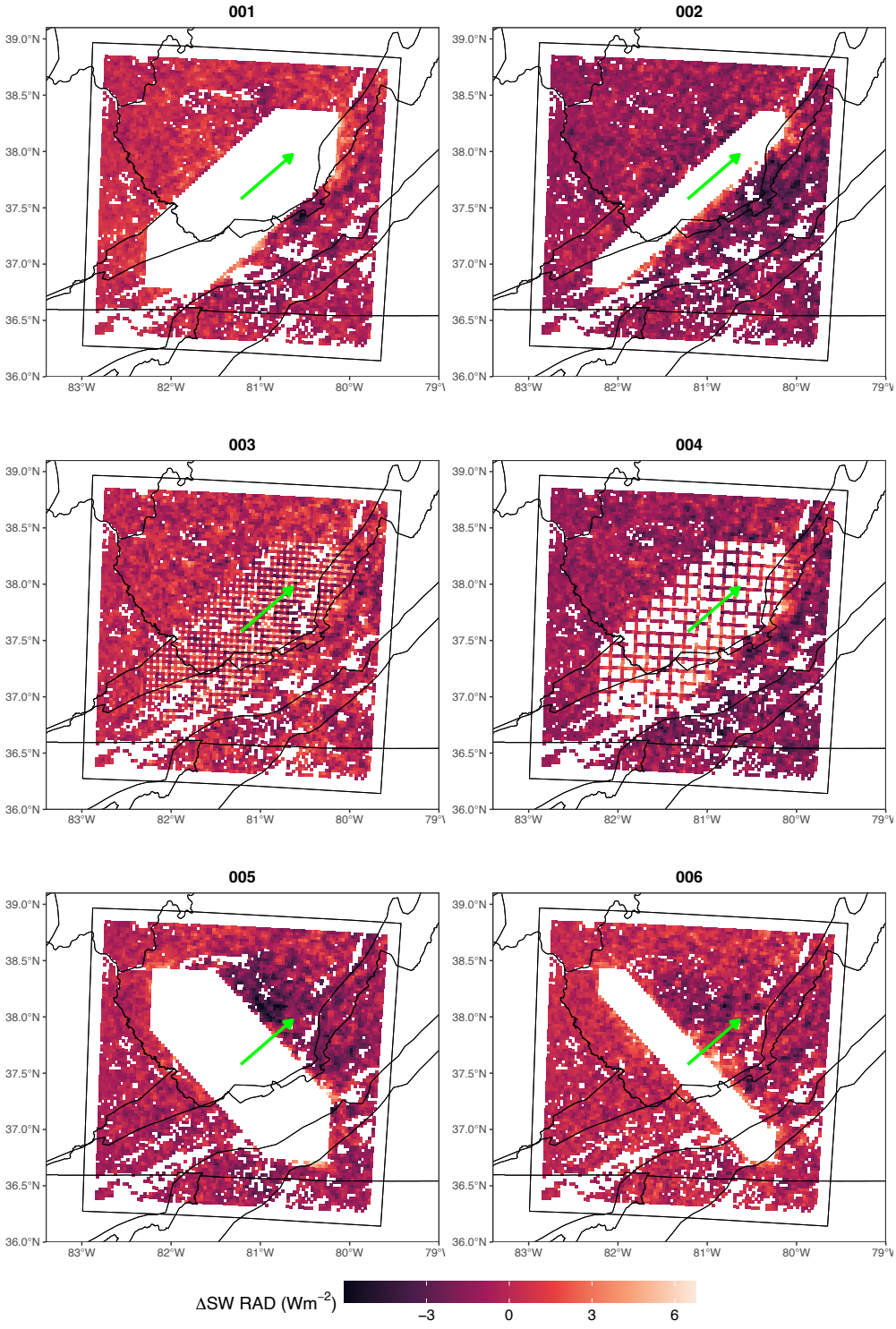

Figure 4.15: Heat maps of $\Delta\overline{\text{SW RAD.}}_{i,j,T}$ across the remaining deciduous forest pixels of all LC Scenarios in 2017.

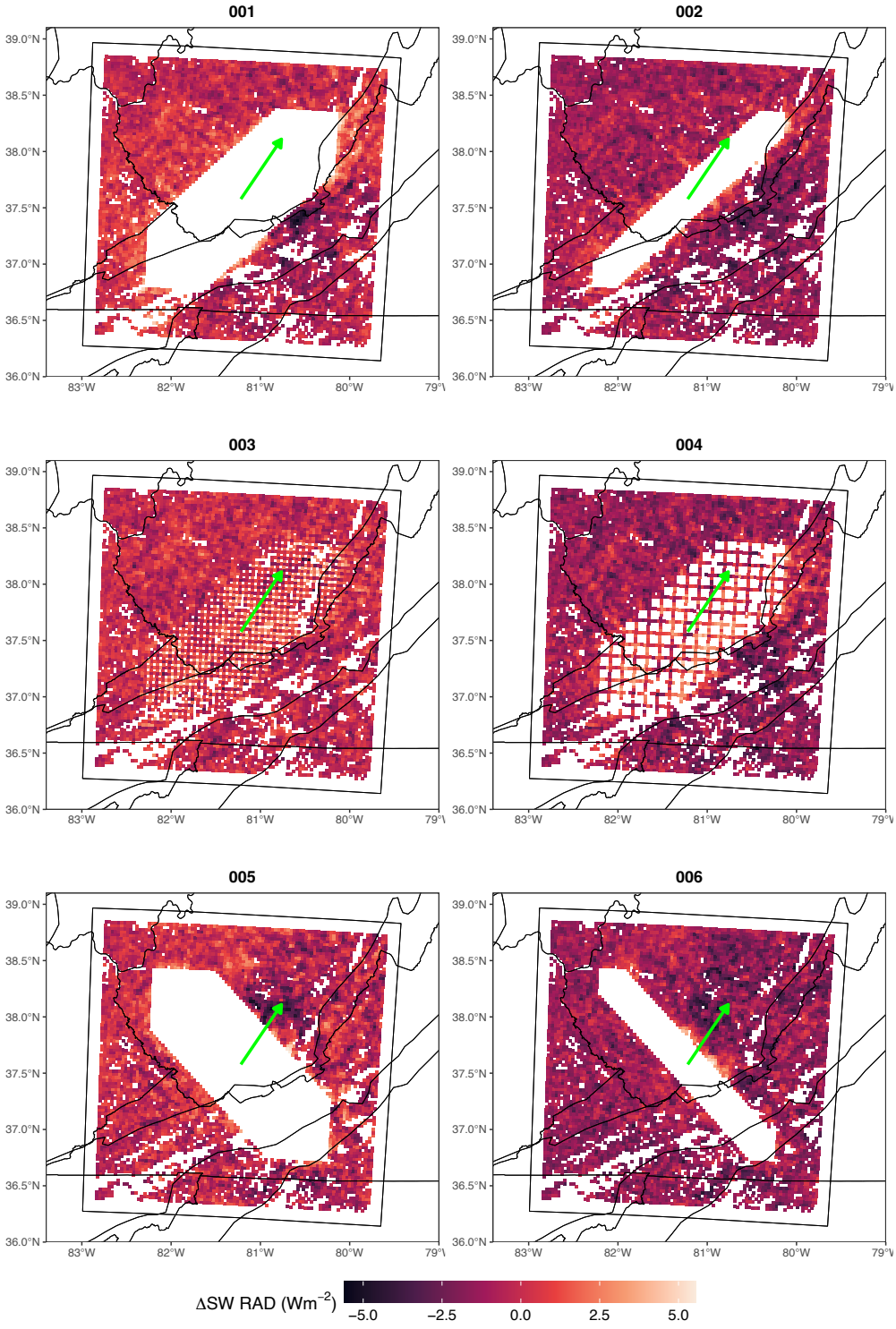

Figure 4.16: Heat maps of $\Delta\overline{\text{SW RAD.}_{i,j,T}}$ across the remaining deciduous forest pixels of all LC Scenarios in 2018.

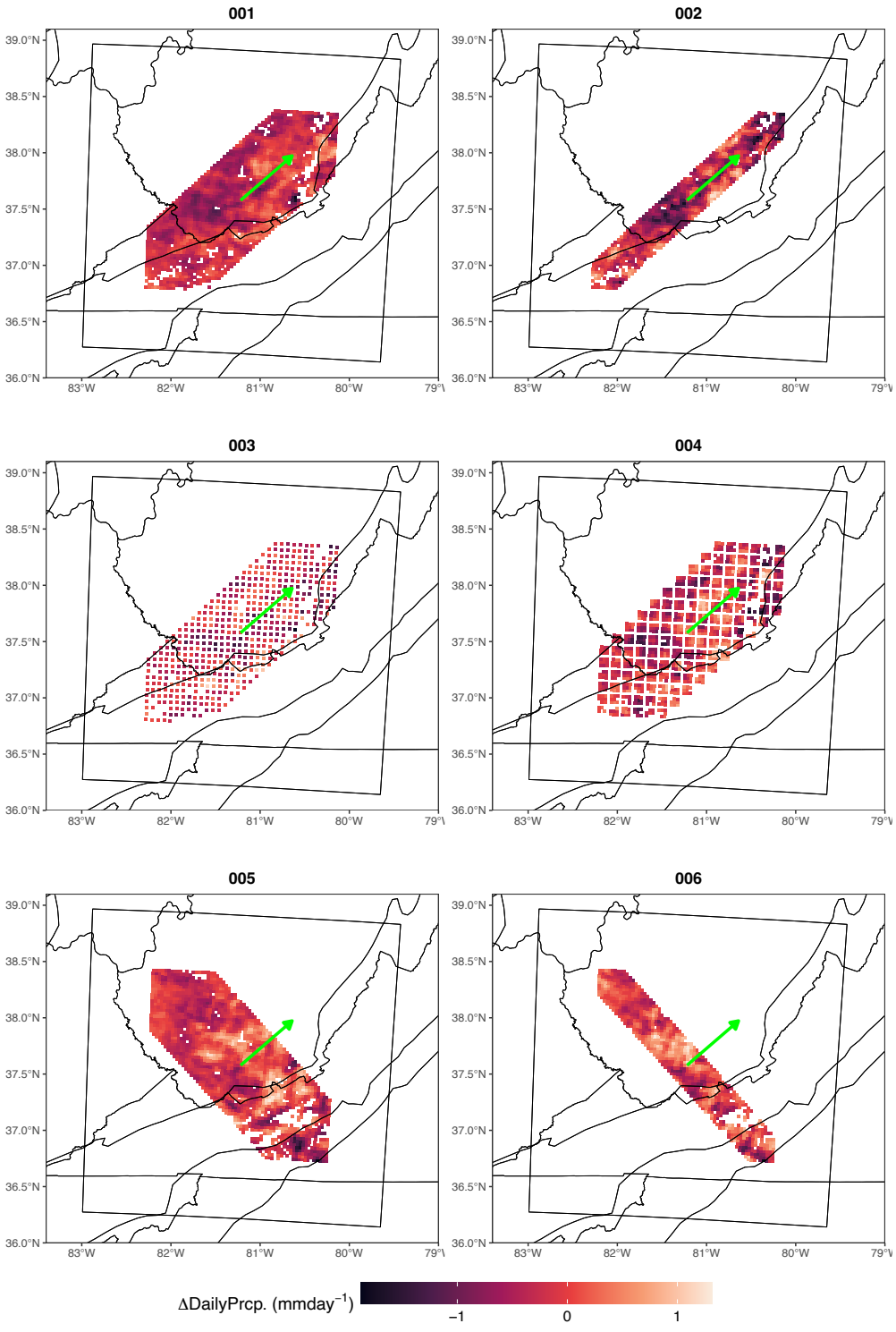

Figure 4.17: Heat maps of $\Delta\overline{\text{Daily Prcp.}}_{i,j,T}$ across the deforested pixels of all LC Scenarios in 2017.

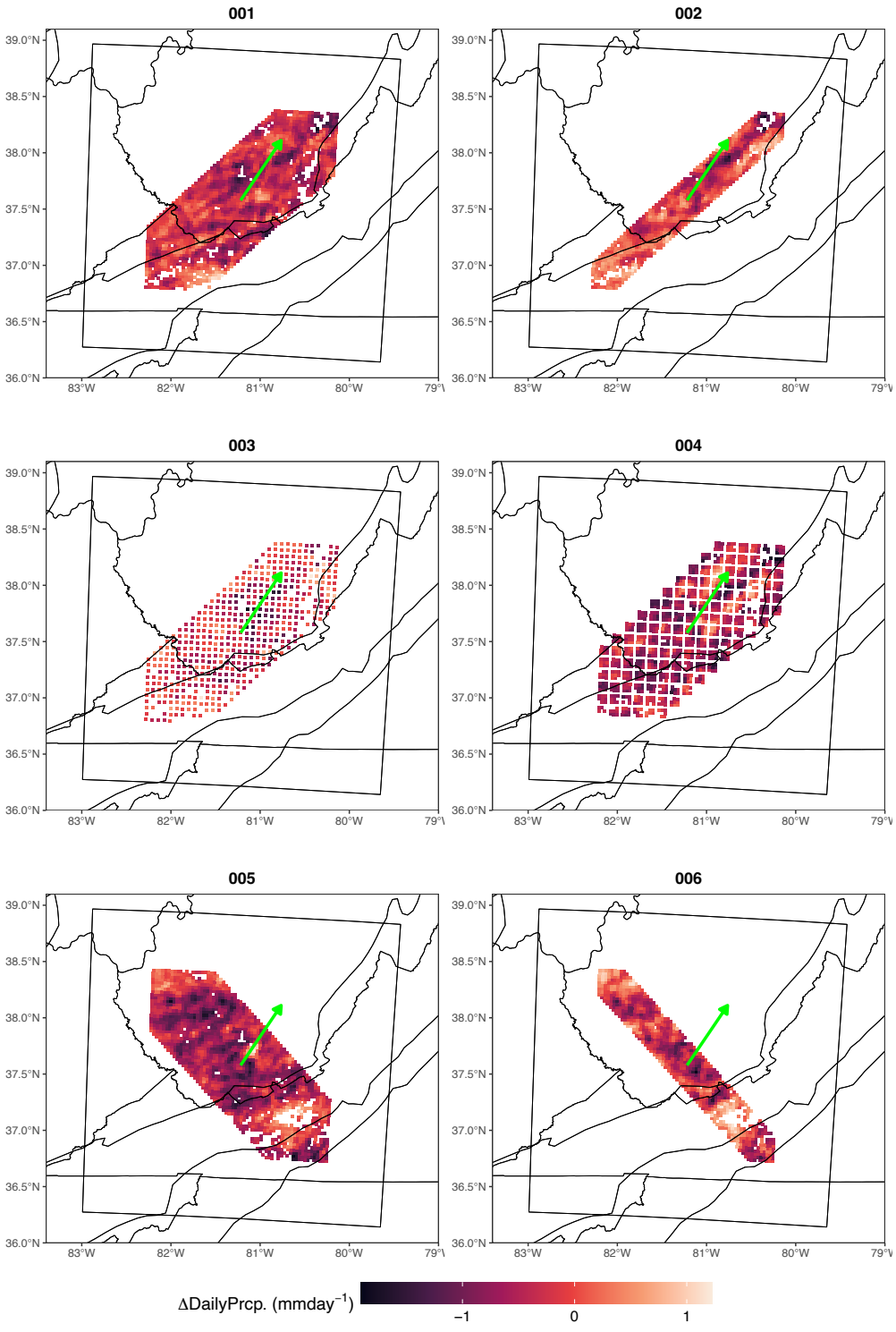

Figure 4.18: Heat maps of $\Delta\overline{\text{Daily Prcp.}}_{i,j,T}$ across the deforested pixels of all LC Scenarios in 2018.

2017, $\Delta\overline{\text{Daily Prcp.}}_{i,j,T}$, Remaining Deciduous Forest Pixels

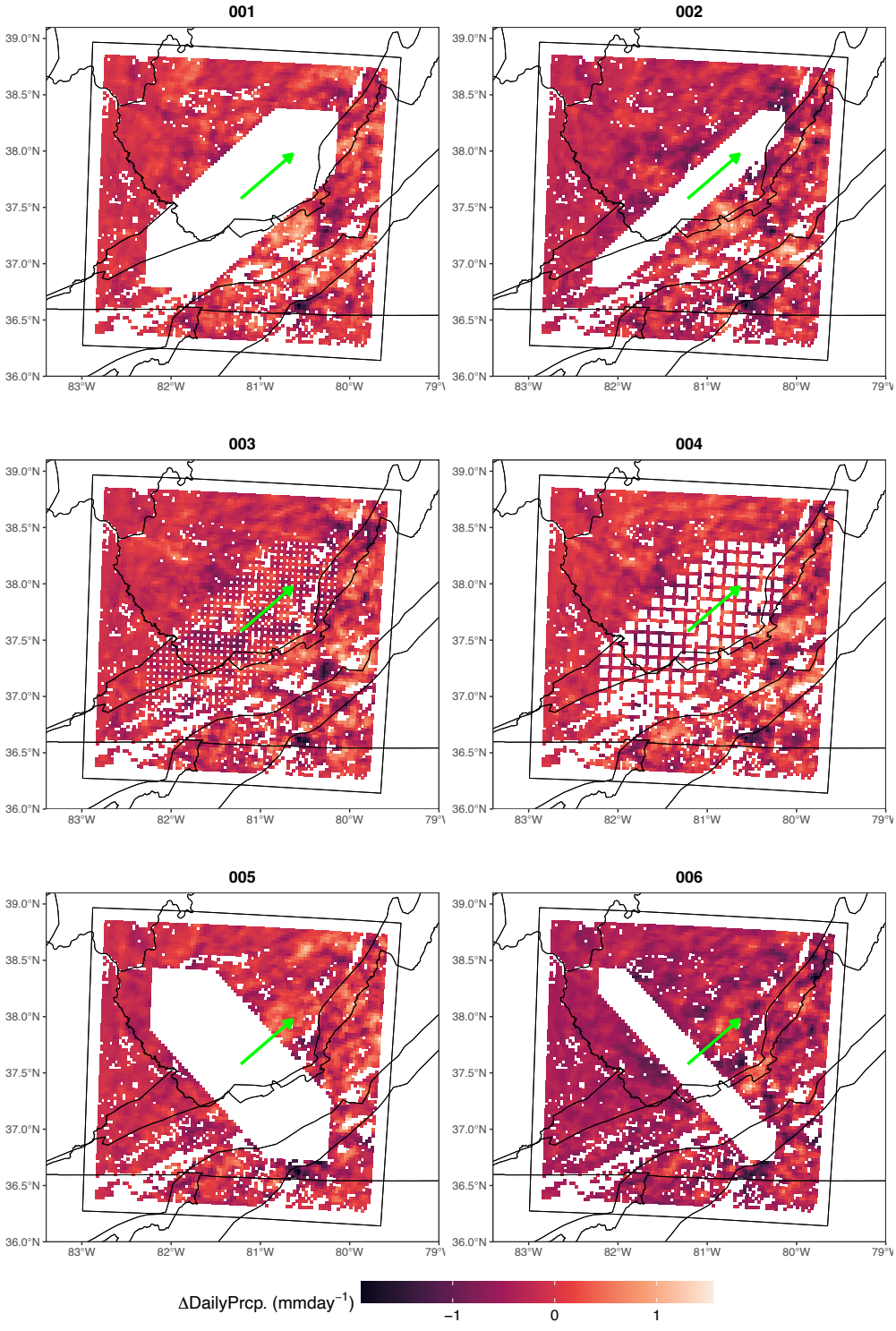

Figure 4.19: Heat maps of $\Delta\overline{\text{Daily Prcp.}}_{i,j,T}$ across the remaining deciduous forest pixels of all LC Scenarios in 2017.

2018, $\Delta\overline{\text{Daily Prcp.}}_{i,j,T}$, Remaining Deciduous Forest Pixels

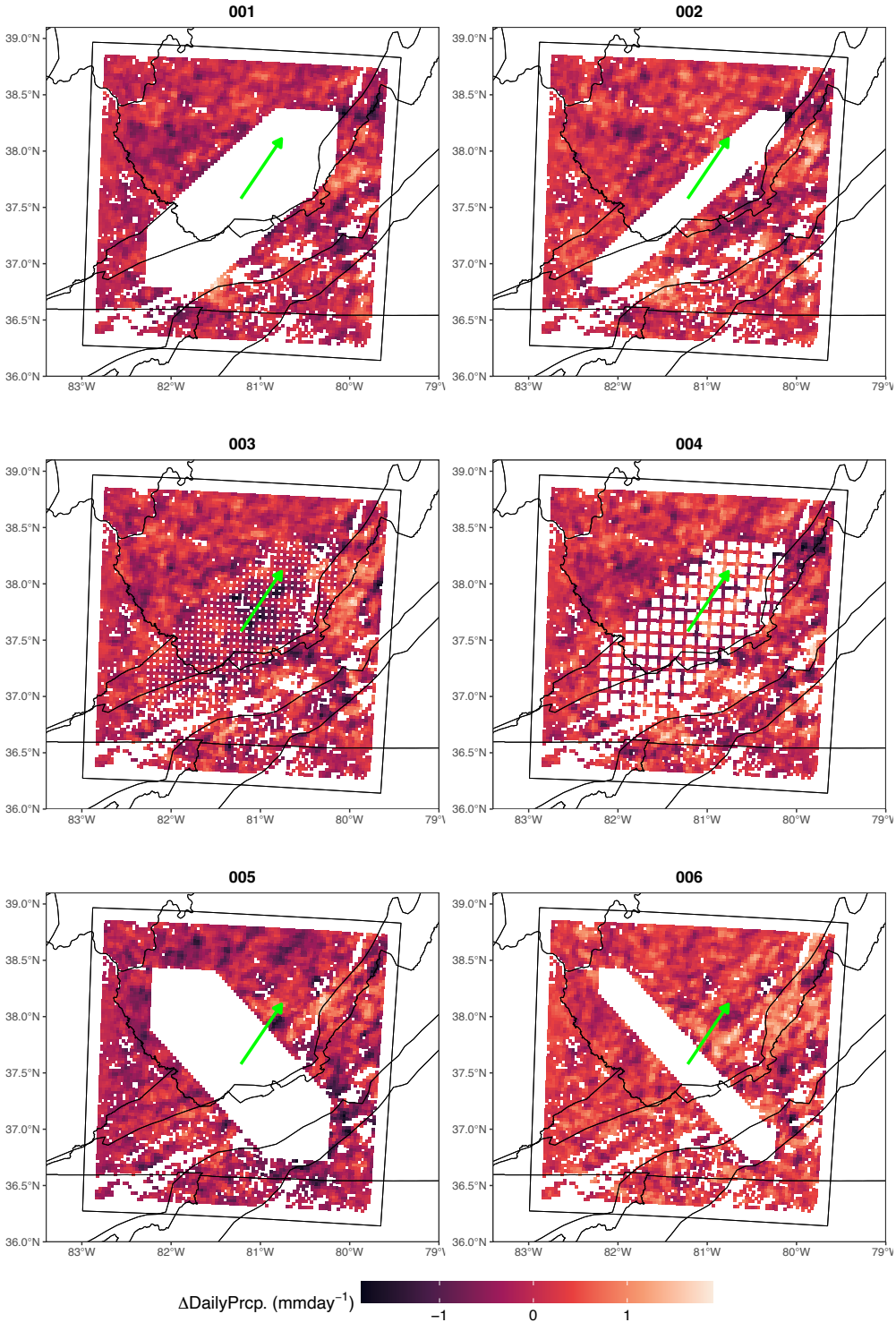

Figure 4.20: Heat maps of $\Delta\overline{\text{Daily Prcp.}}_{i,j,T}$ across the remaining deciduous forest pixels of all LC Scenarios in 2018.

2017, $\Delta\overline{\text{GPP}_{i,j,T}}$, Remaining Deciduous Forest Pixels

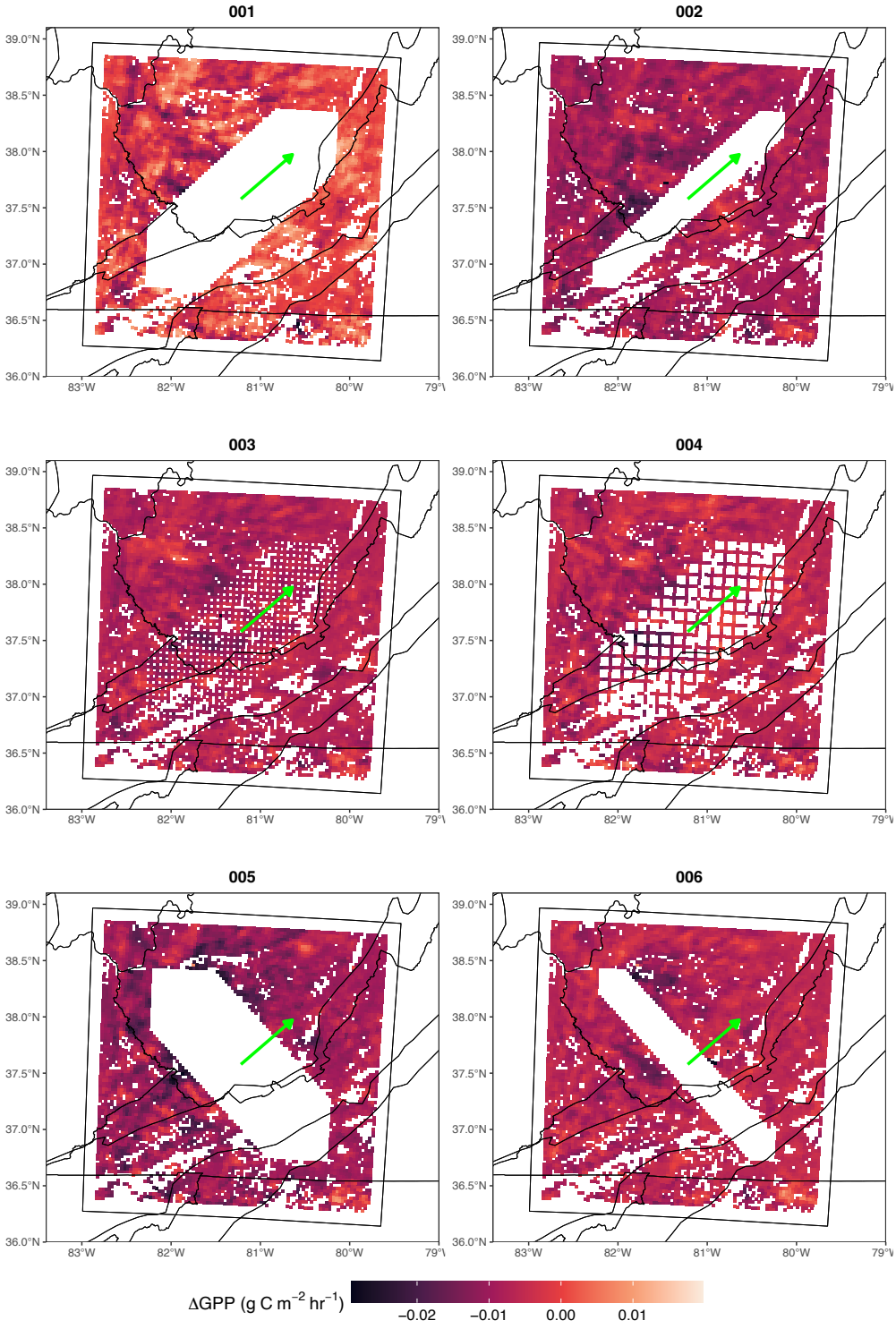

Figure 4.21: Heat maps of $\Delta\overline{\text{GPP}_{i,j,T}}$ across the remaining deciduous forest pixels of all LC Scenarios in 2017.

2018, $\Delta\overline{\text{GPP}_{i,j,T}}$, Remaining Deciduous Forest Pixels

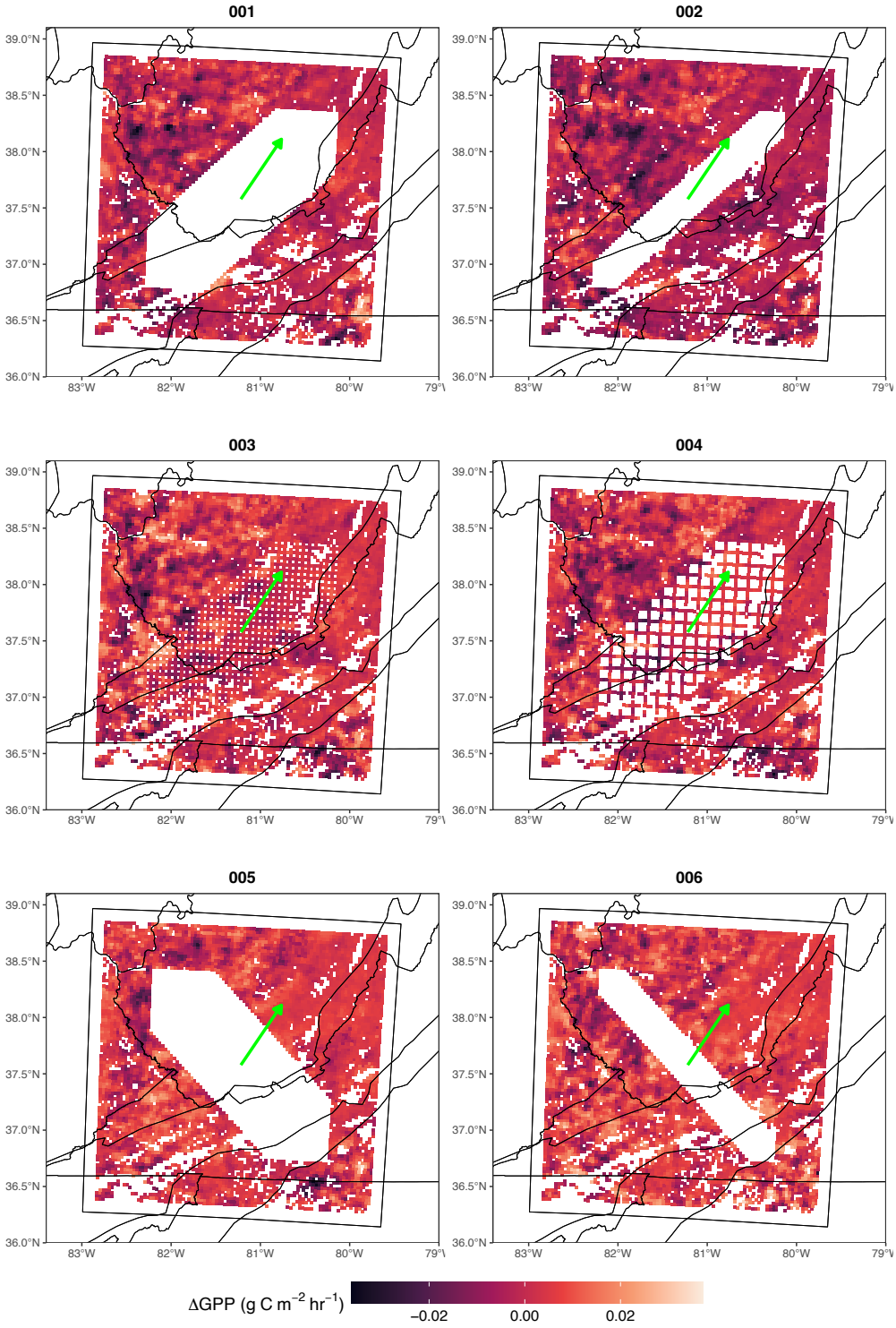

Figure 4.22: Heat maps of $\Delta\overline{\text{GPP}_{i,j,T}}$ across the remaining deciduous forest pixels of all LC Scenarios in 2018.

2017, $\Delta\overline{\mathrm{LH}_{i,j,T}}$, Remaining Deciduous Forest Pixels

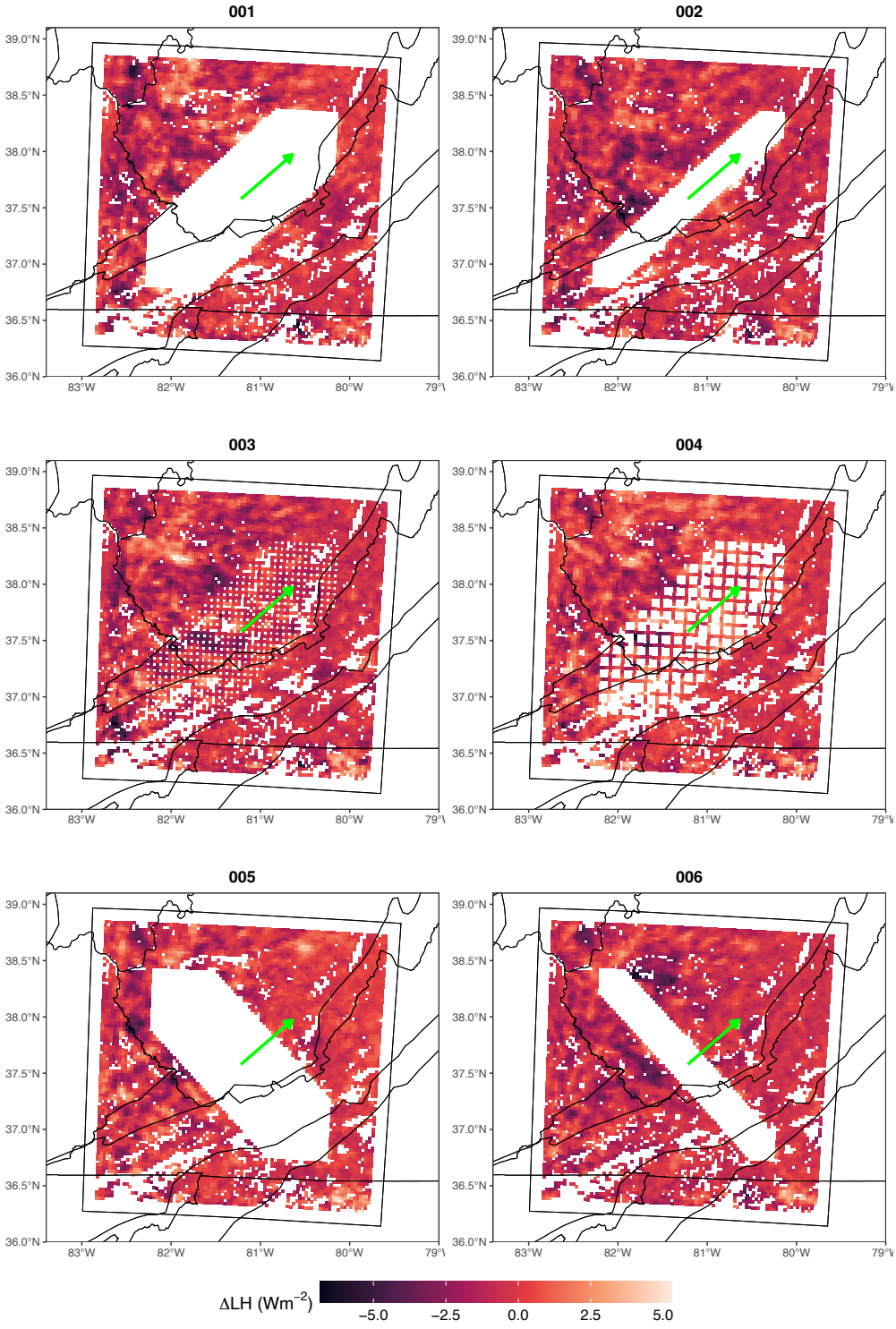

Figure 4.23: Heat maps of $\Delta\overline{\mathrm{LH}_{i,j,T}}$ across the remaining deciduous forest pixels of all LC Scenarios in 2017.

2018, $\Delta\overline{\mathrm{LH}_{i,j,T}}$, Remaining Deciduous Forest Pixels

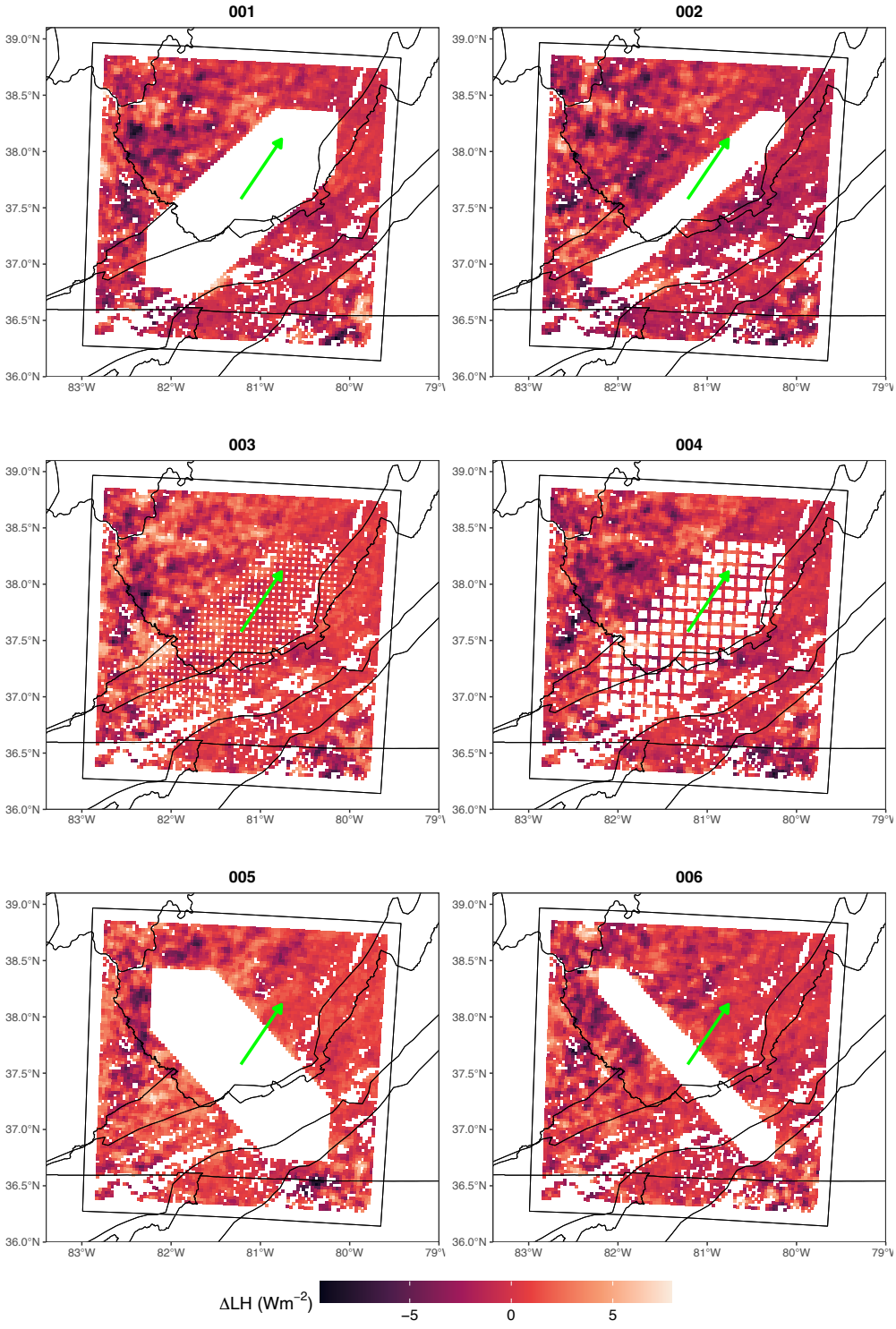

Figure 4.24: Heat maps of $\Delta\overline{\mathrm{LH}_{i,j,T}}$ across the remaining deciduous forest pixels of all LC Scenarios in 2018.